A Fully Customizable Anatomically Based Model of the Crystalline Lens

Cynthia Nicole Wilson

Thesis submitted to the
Faculty of Graduate and Postdoctoral Studies
In partial fulfillment of the requirements
For the PhD degree in Physics

Department of Physics
Faculty of Science
University of Ottawa

ABSTRACT

The human eye is a complex optical system comprised of many components. The crystalline lens, an optical component with a gradient index (GRIN), is perhaps the least understood as it is situated inside the eye and as a result is difficult to characterize. Its complex nonlinear structure is not easily measured and consequently not easily modeled. Presently several models of the GRIN structure exist describing the average performance of crystalline lenses. These models, however, do not accurately describe the performance of crystalline lenses on an individual basis and a more accurate individual eye model based on anatomical parameters is needed. This thesis proposes an anatomically correct, individually customizable crystalline lens model. This is an important tool and is needed both for research on the optical properties of human eyes and to diagnose and plan the treatment of optically based visual problems, such as refractive surgery planning. The lens model consisted of an interior GRIN with a constant refractive index core. The anterior and posterior surface was described by conic sections. To realize this eye model, the optical and biometric properties of mammalian lenses were measured and the correlation relationships between these measurements were used to simplify the model down to one fitting parameter which controls the shape of the GRIN. Using this data, an anatomically correct individualizable model of the lens was successfully realized with varying parameters unique to each lens. Using this customizable lens model, customizable human eye models based on measurements of the entire human eye can be realized.

Table of Contents

List of Tables

Table 4.11: Summary of the effect of the measurement error of each variable on the calculated spherical aberration and focal length using the lens model. The calculated range is ± 2 standard deviations. Those variables with calculated spherical aberration falling outside of the measurement error range are highlighted.

4.3 Table 4.12: Optical and biometric relationships calculated for pig lens measurements. Significant relationships were calculated for $r > 0.423$ ($p < 0.050$) given $N = 22$ samples. m_1 refers to the slope of the line of best fit, and m_2 refers to the x-axis intercept.

Table 4.13: Optical and biometric relationships calculated for rabbit lens measurements. Significant relationships were calculated for $r > 0.754$ ($p < 0.050$) given $N = 7$ samples.

Table 4.14: Optical and biometric relationships calculated for cow lens measurements. Significant relationships were calculated for $r > 0.811$ ($p < 0.050$) given $N = 6$ samples.

List of Figures

3.2.2.1 Figure 3.5: Schematic diagram of the rays in the equatorial plane and the measured variables used in the GRIN profile calculation. The actual measurements are performed in the equatorial plane.

Figure 3.6: (a) Angle formed by the emerging ray $\psi(y)$ vs. displacement of the incident ray from the optic axis y in mm measured in the equatorial plane of one pig lens. (b) Refractive index distribution n(r) vs. normalized lens radius r in the equatorial plane calculated from the points measured in (a).

3.2.3 Figure 3.7: Profile Measurement system. This measurement system consisted simply of a diffuse backlight and CCD camera with an imaging lens to capture the profile of the lens under test. Image (1) was taken to measure the lens thickness and diameter, and (2) was taken to measure the radius of curvature and asphericity; images for the lens anterior and posterior were required.

3.2.4 Figure 3.8: Wavefront system calibration. Shown are sample raw images of the beam pattern after passing through a catalogue glass lens, images of four different ray generator locations have been overlapped to show the beam density. Two images were taken at different locations on the optical axis for measurement of the lens focal length and optical aberrations.

3.3 Figure 3.9: Removal of the crystalline lens from pig eyes. The cornea is first cut and pulled back (a) to expose the iris and lens (b). The iris is removed and the zonules are cut from the lens (c). Immediately after the lens is removed it is placed in a saline solution in a petri dish equipped with a very thin glass bottom (d).

Figure 3.10: Sample images of the spot pattern after passing through three different excised pig lenses farther from (left column) and closer to (right column) the lens' focal plane along the lens' optic axis. Some lenses' images showed strong suture lines (bottom) while others did not (top).

4.1.2 Figure 4.1: Measured equatorial refractive index distribution coefficients C0 (top), C1 (middle), and C2 (bottom), for rabbit, cow, and pig lenses. The bottom error bar indicates the 5th percentile, the bottom of the box indicates the 25th percentile, the middle of the box indicates the mean, the top of the box indicates the 75th percentile, and the top error bar indicates the 95th percentile of all measurements.

Figure 4.2: Demonstration of the variability and individuality of the lens variables for the anterior radius (top), diameter (middle), and focal length (bottom) measured 5 times for 6 different pig lenses.

4.2.2 Figure 4.3: Spherical aberration (a) and focal length (b) vs. GRIN index parameter W for two different rabbit lenses. The spherical aberration and focal length were calculated using the lens model in Zemax while varying W. The

measured spherical aberration and focal length are indicated on the plots by red dots. The error bars above and below the red dots indicate one standard deviation for each measurement. The error in focal length measurement is larger than the plot range.

4.2.3 Figure 4.4: Spherical aberration calculated using the lens model vs. varying values of the measured posterior radius of curvature for one pig lens. Ra was varied over two standard deviations; the mean value of -5.05 is in the centre of this plot. The dotted line represents the mean value of spherical aberration measured for this particular pig lens. The shaded area represents two standard deviations of measurement error. This plot shows that two standard deviations of the measurement error of Ra is slightly outside the measurement error of the spherical aberration.

4.3 Figure 4.5: Linear biometric and optical relationships calculated from orthogonal regressions for pig crystalline lenses. Shown here are the linear relationships between the anterior radius of curvature of the lens and (a) focal length, (b) posterior radius of curvature, (c) lens thickness, and (d) anterior surface asphericity. The slope and intercept for the orthogonal lines of best fit are indicated by m1 and m2, respectively.

Figure 4.6: Demonstration of the lack of correlation between the anterior radius of curvature vs. spherical aberration (left) and W (right). No significant correlation of any kind was found between the spherical aberration or W and any other parameter measured.

4.4 Figure 4.7: Calculated spherical aberration vs. GRIN index parameter W for two different pig lenses. The dark blue curve was calculated using the original measured biometrical data. The light blue curve was calculated using only the measured lens focal length and thickness, and the rest of the required variables were calculated using the biometric linear relationships. The measured spherical aberration is indicated on the plot by red dots on each curve. The corresponding W for each curve was slightly different. W corresponding to the modeled data was used to find the lens focal length calculated from the model.

Figure 4.8: Measured focal length of all pig lenses and calculated focal length using the lens model. The largest percentage error between the measured and calculated focal length is 9.1% for pig 9. The average percentage error for the entire group is 3.6%.

Figure 4.9: Orthogonal regression between Focal length calculated from the customizable crystalline lens model and the measured focal length for 22 pig lenses.

Figure 4.10: Measured focal length of all cow lenses and calculated focal length using the lens model. The largest percentage error between the measured and

calculated focal length is 6.3% for cow 5. The average percentage error for the entire group is 2.7%.

5.1 Figure 5.1: Comparison of the isoindicial contours in the sagittal plane developed in this thesis (a) and in the GRIN model developed by Pierscionek et al. (b). Pierscionek's model assumed elliptical contours where this thesis made no assumption other than a spherical core.

Figure 5.2: GRIN distribution for a pig lens model developed in this thesis along the x, y, and z axes, showing a different function for the z axis.

Figure 5.3: GRIN distribution for a human lens model developed by Pierscionek along the x, y, and z axes, indicating the same function describes the GRIN along all axes.

Figure 5.4: Comparison of GRIN measurement distribution in the equatorial plane from Pierscionek(2005)[3] (dotted line) and this thesis (solid line) for pig lenses (a), and from Chan(1989)[4] (dotted line) and this thesis (solid line) for cow lenses (b). The equatorial plane GRIN calculations were all measured using the same technique.

List of Variables

n	refractive index
n_c	core refractive index
n_s	surface refractive index
c	curvature
R	radius of curvature
R_a	anterior radius of curvature
R_p	posterior radius of curvature
q	asphericity
q_a	anterior asphericity
q_p	posterior asphericity
C_0 C_1 C_2	equatorial GRIN index parameters
W	GRIN index distribution fitting parameter
a	lens dimension along the z-axis or optical axis
b	lens dimension along the lens radius or equatorial plane

Acknowledgements

Many people are due thanks for helping make this work possible. First and foremost, I would like to express my sincere gratitude to my supervisor, Dr. Rejean Munger, for his support and patience in seeing me through to the end of this project. Also I would like to thank David Priest for the technical help and support provided with the calculations and modeling and for many fruitful discussions.

I also thank the past and present members of the Visual Optics Lab at the University of Ottawa Eye Institute for all of their support when my thesis seemed like it was going nowhere. And of course my parents for their support throughout this whole process, both in their encouragement and belief in me when I thought all hope was lost.

I would also like to thank my internal and external thesis exam committee members for their valuable input during my formal defense, especially Dr. Adrian Glasser for travelling to the University of Ottawa to take part.

Last but not least, I thank my husband Kevin, for all of his love and support, and for putting up with my exponentially increasing level of insanity as I prepared this manuscript.

1. Introduction

1.1 Goal of the Project

The goal of this thesis is to construct an anatomically correct, computerized model of the human crystalline lens which can be customized to reproduce the unique optical properties of individual human crystalline lenses. This new lens model is a critical step towards a more long term goal of creating a complete computerized, individualizable model of the human eye which can be used in a clinical setting for the diagnosis and treatment planning of optical problems of individual patients. As a basic science tool the model will be useful in studying the optical properties of the crystalline lens to better understand its contribution to vision in an individual.

1.2 The Need for a New Crystalline Lens Model

The human eye is a complex optical system comprised of several optical components, most of which are well characterized. The exception is the crystalline lens which is the most difficult component of the eye to characterize experimentally in-vivo as it has a gradient index (GRIN) and different anterior and posterior surface shapes. Its location inside the eye renders it nearly impossible to isolate and measure all of its biometric and optical properties non-invasively. Numerous researchers have measured some aspects of the crystalline lens both in-vivo and in vitro using various techniques ranging from laser beam ray tracing to magnetic resonance imaging. Measurements such as the focal length, spherical aberration, surface curvature, and asphericity are relatively easily obtained, especially ex-vivo. The property of the lens that is most challenging to characterize is the GRIN structure inside of the lens.

There is a large variety of published GRIN and / or crystalline lens models. Some are purely mathematical constructs with a narrow range of applicability while others are based on biometric and GRIN measurements of real lenses. Currently, there is no real consensus on the structure of the GRIN within the crystalline lens. Furthermore, none of these models were designed to be customizable so they cannot reproduce the variance

observed in the optical properties of the crystalline lens across the population. In order to address this need, a new customizable GRIN model is required.

1.3 Working hypothesis and research approach

The aim of this thesis is to produce a crystalline lens model with the adaptability to be able to reproduce the optical properties of an individual's lens, while maintaining as many realistic anatomical features for that particular crystalline lens as possible. What is required then is a model with as many anatomical features of a real lens, both biometrically and structurally, with a real diameter, anterior and posterior thicknesses, surface curvatures, asphericites, and an inner GRIN structure.

The principal working hypothesis of this thesis is: An anatomically based customizable crystalline lens model can be constructed which can reproduce the optical properties of an individual crystalline lens. There are two corollaries to this hypothesis - there are consistent relationships between the biometric parameters and optical parameters of the lens which can be used to reduce the model's complexity, and the three-dimensional distribution of the GRIN of this crystalline lens model can be approximated from the experimentally measured GRIN in one lens plane (the equatorial plane).

The steps required in realizing and validating this crystalline lens model were:

A) Form a general anatomically based, flexible model of the lens structure using as many adjustment parameters as required to allow for individual customization.
B) Measure the anatomical and optical properties of real excised crystalline lenses from different mammalian species similar optically and biometrically to human crystalline lenses.
C) Apply these measurements to the lens model to reproduce the optical properties of individual crystalline lenses and understand the impact of the lens model parameters on the optical performance of the lens.
D) Evaluate the correlations between and importance of each of the lens model parameters to reduce the model to its simplest form.
E) Validate the simplified lens model as a predictor to the optical properties of the individual crystalline lenses.

F) Assess the limitations of this model and evaluate its possible inclusion into a full eye model.

As healthy human tissue is almost impossible to obtain for research purposes, the experimental testing of the model was performed primarily on animal lenses with several similarities to human lenses. To demonstrate the flexibility of the model, three different mammalian species, previously used for this type of investigation (porcine, bovine and rabbit) were investigated.

1.4 Outcome of the project

As will be shown in the rest of the thesis the outcome of the project was a customizable computerized model of the crystalline lens that can be used either as a stand-alone lens model or as a part of a complete model of the eye types used in this thesis with the possibility of extending the model to the human eye. It will also be demonstrated that there are significant similarities in the shape of the GRIN across different mammalian species suggesting similarities in the GRIN formation in these species. Finally, it will be verified that the number of customization parameters of the final model is compatible with use in an eye model depending solely on clinically available data.

1.5 Thesis Structure

The remainder of Chapter 1 will present the necessary basic information about the human eye and crystalline lens including its anatomical and optical properties as well as the variation of these properties among the human population and refractive errors in human vision. Chapter 2 will present the justification for the experiments performed as well as outline current eye models and their limitations within the scope of the goal of this project. The structure and basis for the new lens model developed in this thesis as well as a description and validation of the equipment and methodology used to measure the properties of the crystalline lenses will be presented in Chapter 3. Chapter 4 will present the measurement results of different mammalian crystalline lenses, apply relationships found to the new model to provide important simplifications, and finally,

show results validating the simplified model. Results will be discussed, conclusions given and possible future work discussed in Chapter 5.

1.6 Statement of contribution

In this thesis, a hypothetical customizable crystalline lens model, defined by R. Munger in previous work[1], was used as a starting point in forming a customized computer model of the crystalline lens. The optical and biometric properties of real crystalline lenses were measured on a new type of ray tracing measurement system created by the author for use specifically for this thesis. The author showed through these measurements that the equatorial GRIN of lenses from different mammalian species was the same. The author, working with Dr. Munger, developed the necessary biometric relationships that allowed the simplification of the customizable lens model to the level that it could be used in an eye model using only clinically obtainable data.

1.7 Background

In order to understand what is required for a custom lens model, it is first necessary to understand several concepts surrounding human vision. The remainder of this chapter is divided into three main sections. The first section covers the anatomy and physiology of the human eye and more specifically the crystalline lens. In the second section the optical properties of the human eye are discussed, as well as optical dysfunctions of the human eye and current treatments for these dysfunctions. In the third section the wide variation of the biometric and optical parameters of the human eye and lens amongst the population will be presented. The need for an anatomically correct customizable model of the eye and lens will be made apparent in discussing the limitations of current treatments and the variability of the human eye and lens.

1.8 The Human Eye and Crystalline Lens

1.8.1 Anatomy and Physiology of the Human Eye

The eye and the brain together form an amazing visual system unlike any man-made optical system[2]. The visual system is capable of adapting to and detecting light

levels ranging from near darkness to very bright sunlight, corresponding to a dynamic contrast ratio of approximately 1,000,000:1. The human eye can detect wavelengths in the electromagnetic spectrum ranging from 380 to 780nm, with a peak in sensitivity occurring at approximately 555nm. A dynamic range of focus is also possible in the human eye, ranging from approximately 8cm (for young eyes) in front of the eyes to infinity. The human vision system is also capable of stereo vision, allowing objects to be perceived three-dimensionally.

The entire visual system is a two part process; the first is the internal optics, involving the refractive components of the eye forming an image of the real world on the retina (back of the eye). The second is the neural processing; transforming the image pattern on the retina into electrical signals which are sent on to the brain to be interpreted as a visual percept. The rest of this section is concerned with the eye's internal optics which is more relevant to the topic of this thesis.

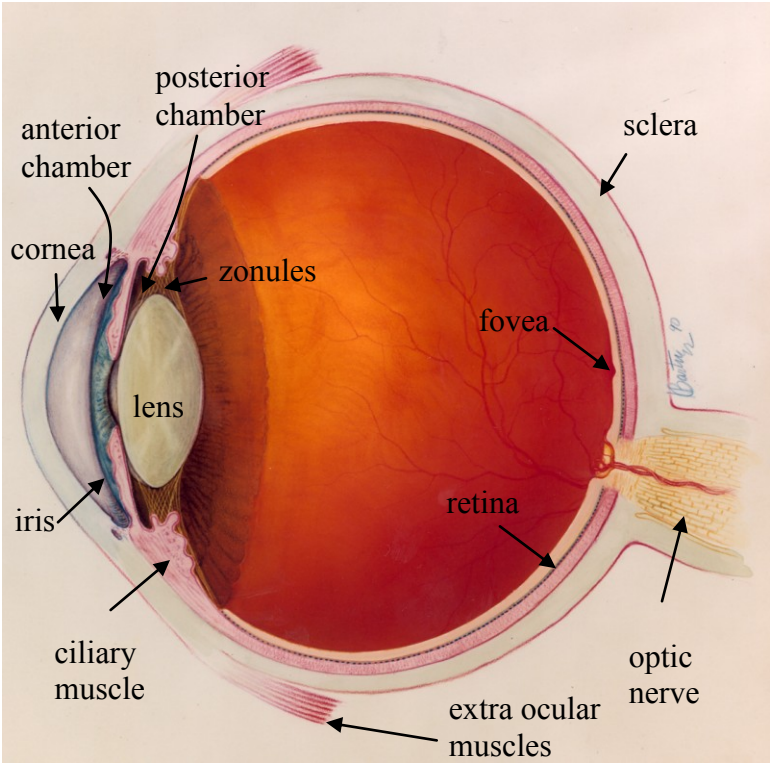

Figure 1.1: Schematic of the anatomy of the human eye. Courtesy: National Eye Institute, National Institutes of Health, USA. (www.nei.neh.gov)

The anatomy of the human eye is shown in Figure 1.1. Light is refracted as it first enters the eye through the cornea, a multi-layered collagenous structure optically

transparent over the eye's wavelength sensitivity range. Beyond the cornea lies the anterior chamber which is filled with aqueous humour, consisting mostly of water with few other substances such as ions and proteins. Beyond the anterior chamber lies the iris, which is the aperture of the eye's optical system. It is an annular shaped muscle controlled by the parasympathetic and sympathetic nervous system for contraction and dilation, respectively. The pupil size automatically adjusts to control to the amount of light entering the eye. Directly behind the pupil is the posterior chamber, also filled with aqueous humour, where the crystalline lens is located. The crystalline lens of the young human eye is a flexible cellular structure consisting mostly of water and proteins, to be described in greater detail below. The lens is attached at its equator to an annular shaped structure called the ciliary body by small elastic fibers called the Zonules of Zinn, or simply zonules. The ciliary body is responsible for the production of aqueous, which provides nutrients to the crystalline lens and the cornea. The ciliary muscle, part of the ciliary body, is responsible for a process called accommodation, which allows for the on-demand change in focusing power required for the viewing of near and far objects. Accommodation will be discussed in further details below.

The cavity beyond the lens, called the vitreous cavity, is filled with a viscous jelly-like substance called the vitreous humour which is composed mostly of water and collagen. At the very back of the eye lies the retina, an extremely complex layered structure of nerve cells extending around the inner surface of the sclera from the optic nerve to the ciliary body. The retina contains photoreceptor cells, rods and cones, which transform light energy into neural signals. The rod cells are more sensitive to low light levels, whereas the cone cells are used more in viewing objects under higher lighting conditions. The central area of the visual field falls upon a specialized area of the retina called the macula, at the centre of which lies a shallow depression called the fovea. The central field of view occurs at the fovea and vision is at its highest resolution since it is the region containing the highest density of cones. The entire eye, with the exception of the front surface where the cornea lies, is coated in a layer of hard, dense, connective tissue called the sclera. The extra ocular muscles control movement to the eye and are attached to the sclera. The optic nerve leaves the eye through the sclera, carrying signals

to the brain through the axon fibers originating in the retina. The optic nerve head forms a blind spot on the retina since it is void of photoreceptors.

1.8.2 Anatomy and Physiology of the Human Crystalline Lens

The young healthy human lens is a complex, optically clear, flexible structure responsible for refraction of light between the cornea and the retina (Figure 1.2). It is avascular to allow the maximum amount of light through to the retina and is not innervated. Structurally, it is surrounded by an acellular collagen elastic envelope called the lens capsule, a semi-permeable membrane allowing fluid and nutrient flow from the aqueous to the cells of the lens. The zonules are attached to the lens capsule at the equator and are essential to the process of accommodation. Just inside of the lens capsule along the anterior surface is the lens epithelium, which is responsible for producing new lens cells and controlling the lens' metabolic processes. A germinative region exists at the lens equator where the epithelial cells bow towards the central anterior region and continuously form new lens cells. The individual cells making up the bulk of the lens (lens fibre cells) are actually long crescent-shaped fibers, arranged end-to-end, extending around the lens in a complex pattern from their equatorial origin, towards the anterior and posterior vertices, and finally towards the lens centre. Lens fibers cells are closely connected at their cell membranes and are also interlocked closely together with small interdigitations, allowing for the passage of metabolites, nutrients, and other necessary material within the lens as well as interconnecting all of the fibers together forming the lens as one continuous element. The human lens is a biconvex oblate spheroid, with the anterior and posterior sections having different curvatures and asphericities.

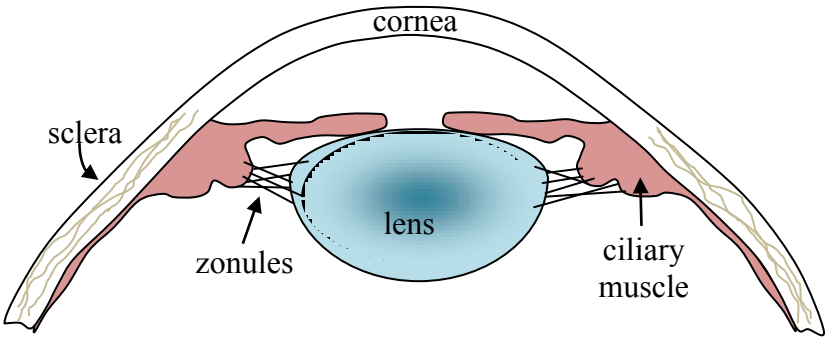

Figure 1.2: Basic configuration of the crystalline lens inside the eye. It is attached to the ciliary muscle by the zonules at its equator, has different anterior and posterior shapes and sits approximately 3mm behind the cornea measured from the anterior surface.

The lens is the only organ in the human body where the same cells exist throughout an individual's lifetime. The lens epithelial cells continuously grow and produce lens fibers, with new lens fibers growing over old lens fibers. As a result, the old cells are continuously pushed towards the inner regions of the lens and compressed[3]. As the cells move towards the centre of the lens they eventually lose their organelles and finally their nucleus, while at the same time increasing in fibrous material. As they are created lens fibers join both at the anterior and the posterior apex of the lens and structures, called sutures, appear beginning in the lens centre and radiating outwards. Optically these sutures are visible when inspecting the lens; however they are not important to vision and have been ignored in optical models of the lens. Because of this inward growth process, the lens takes on an onion like structure with a compressed core. The centre of the lens becomes so compressed with age that it takes on a more uniform composition and spherical shape. The outer region, still having recognizable fibers and a concentric ring-like structure is known as the cortex. As the lens grows and ages, it hardens and increases in volume (i.e. increasing in diameter by approximately 0.1mm to 0.5mm per decade[4]) causing its optical properties to vary continuously with age.

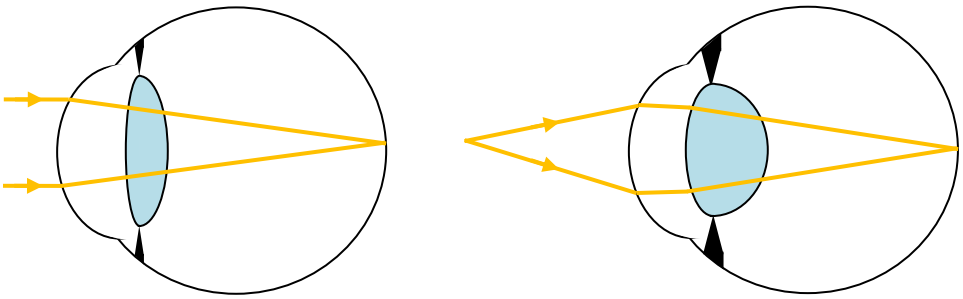

Figure 1.3: Schematic of the process of accommodation by the crystalline lens. The eye is shown in the unaccommodated state on the left, and in the accommodated state on the right.

One of the important functions of the lens is accommodation, which is the process of changing the eye's refractive power on demand for viewing of objects anywhere between a few centimeters in front of the eye and infinity. It is a complex process involving rapid neuromuscular and biophysical adaptation, shown in Figure 1.3. The zonules are attached to both the lens equator and the ciliary body. The tension on the zonules can be controlled by the contraction of the ciliary muscle (located inside the ciliary body) and the tension on the muscle controls the tension on the lens capsule. In

the relaxed state of the muscle, the zonules are under tension, the lens flattens and the eye is in an unaccommodated state for distant vision. When the muscles contract the tension on the zonules and lens is released, the lens thickness and surface curvatures increase, and the eye is in the accommodated state for focus closer than infinity.

The crystalline lens is comprised of 66% water and 33% proteins[5] of three main types; α, β, and γ crystallins. The lens refractive index is determined by the water to protein ratio, with the ratio of the γ crystallins having the greatest effect on the refractive index. Different types of crystallins are present in different concentrations across the lens and the concentrations of these crystallins change with age. The changes in the concentration of these proteins as a function of aging are thought to be due to the change in the structure and/or breakdown of the proteins after synthesis. The concentration of γ crystallin is highest in the nucleus and decreases rapidly from the cortical region towards the outside of the lens. The increase in refractive index towards the centre of the lens has been shown to follow the increase in concentration of γ crystallins[6,7].

Two very common dysfunctions of the lens that affect a large proportion of the population are presbyopia and cataracts. As mentioned previously, as the lens ages it becomes more optically dense and stiffer. In most eyes, the lens will eventually grow is size and stiffen which will contribute significantly to the loss of accommodative function and the eye is more or less fixed in its unaccommodated state. This part of the aging process is known as presbyopia and will affect almost everyone over the age of 50. The stiffening of the lens is thought to occur due to changes in the crystallin proteins causing them to crosslink, as well as the crystallins adhering to the lens fiber cell walls[8].

Cataracts are the progressive opacification of the lens causing an increase in refraction, scattering, absorption, and or reflection of light as it passes through the lens. This results in a progressive loss in vision, and if left untreated will lead to blindness. There are many different causes of cataracts, including exposure to UV light, diabetes and high blood pressure. Detailed discussion on this topic is beyond the scope of this thesis as the interest lies in modeling the working, healthy lens.

1.8.3 Vertebrate Crystalline Lenses

In this thesis it was necessary to perform various measurements on crystalline lenses of various species similar optically and biometrically in structure to human lenses since the end goal was a model of the human crystalline lens. It is common and scientifically accepted practice to use animal models as a starting point in biological studies since human tissues are not readily available for research.

Cow, pig, and rabbit lenses were chosen for the investigations for this thesis because they are readily available and are known to have well documented biometric and optical properties similar to human lenses. Cow, pig and rabbit lenses have asymmetric anterior and posterior sections, and have similar aberrations to human lenses. Pig and rabbit lenses in particular are similar in size and have similar focal lengths to human lenses. The lenses of other species, such as fish, reptiles, and rodents are also readily available to study, however they diverge significantly from human crystalline lens properties as they are more spherically shaped and exhibit different optical properties. Cow, pig, and rabbit lenses have been studied extensively by other authors and therefore the results obtained in this thesis may be compared with others.

Several differences do exist between the three species studied in this thesis and human lenses. Cow, pig, and rabbit lenses only exhibit a few diopters of accommodation, whereas young human lenses are capable of up to 10 diopters of accommodation. Furthermore, the changes in human crystalline lenses due to accommodation and ageing may not be present in cow, pig, and rabbit crystalline lenses and therefore further study is required regarding these matters before assuming the model developed here can be directly applied to human lenses. Nonetheless, the three species were chosen for this thesis to prove the model's validity both within and across several different species.

1.9 Optical Properties of the Eye and Lens

1.9.1 Optical Performance of the Eye and Lens

This section gives an overview of the optical performance of the visual system of a young normal eye using parameters found in two widely accepted reference books on the topic of visual optics[2,9]. The optics of the eye vary widely across the population; the

parameters give in this section have very broad ranges. The variation in the eye's dimensions and optics will be discussed in the next section.

The population average for the total refractive power of the unaccommodated eye is 60D corresponding to a focal length of about 17mm. The main refracting components of the eye are the cornea and the lens. The cornea provides about 65% of the eye's refractive power; the remainder is provided by the lens. Refraction takes place at the anterior (48D) and posterior curvatures (-6D) of the cornea. Refraction also takes place at both surfaces of the lens as well, with the amount of refractive power of the lens surfaces dependant on the accommodative state. Continuous refraction also takes place within the lens due to its GRIN structure. The aperture stop of the eye is the flexible iris. On average the length of the eye is 18mm at birth and increases to 24mm by adulthood.

The total thickness of the cornea at its vertex is approximately 600μm, and its uniformly distributed refractive index is 1.376. The anterior surface of the cornea is ellipsoidal in shape with its major axis perpendicular to the optic axis and an asphericity (conic constant), q, of approximately -0.27. The posterior surface shape is difficult to measure due to the effect of the anterior surface on these measurements; nonetheless it has radius of curvature of approximately 6.2 mm and an asphericity of approximately -0.6.

In the relaxed state the total thickness of the young lens is approximately 3.6mm and the refractive power is approximately 19D. A normal adult human lens has an equatorial diameter between 8.5 and 10mm. The curvatures of the anterior and posterior lens surfaces are about 12.4mm and 8.1mm, respectively. The anterior and posterior surface curvatures are also ellipsoidal in shape, with asphericities of about -0.94 (major axis perpendicular to the optic axis) and 0.96 (major axis parallel to the optic axis), respectively. Upon accommodation, the lens on average increases in thickness by 0.3mm, the anterior surface moves towards the cornea by 0.2mm, and the radii of curvatures of the anterior and posterior surfaces decrease by about 4.9mm and 1.3mm, respectively[10]. These changes due to accommodation increase the refractive power of the lens to approximately 30D.

The refractive index of the lens increases towards the centre; the index of the human lens at the surface is about 1.386 increasing to about 1.406 at the nucleus where it

remains constant. An equivalent uniform index lens would consist of a lens with a refractive index of approximately 1.42, an index well above the index anywhere in the lens, to have the same paraxial power. It is known that if γ crystallins (the highest measured refractive index lens proteins) were used to produce a uniform refractive index lens, the concentration of lens crystallin required to produce an index of 1.42 would result in an opaque lens. Therefore the GRIN of the lens serves to increase the effective refractive power of the lens given these properties of the crystallin proteins.

As for most optical components, aberrations are inherent to the individual optical components of the eye, and also the eye as a whole. The main sources of these aberrations are the two main refractive components of the eye; the cornea and the lens. Aberrations referred to thus far are monochromatic; as most of the studies measuring the aberrations of the eye do so using one wavelength of light. Chromatic aberrations also exist in the eye, occurring due to the dispersive quality of the eye since it is mostly made up of water, and also due to the variation of the eye's power with wavelength. The interest of this thesis is monochromatic aberrations and chromatic aberrations will not be discussed further.

Several types of aberrations exist in the eye; those most commonly affecting vision are spherical and cylindrical defocus. Spherical defocus in human eyes can range from -10D (eye power too large) to +10D (eye power too weak) or more. While cylindrical error is usually no larger than about 3.5D. These errors are easily corrected optically with ophthalmic or contact lenses.

The eye lacks a common axis among each of the optical components; therefore the optic axis of the eye is referred to as the line of best fit (Figure 1.4). A cylindrical refractive error occurs when one or more of the cornea or lens' surfaces are toroidal in shape, tilted, or displaced with respect to the eyes main axis. Furthermore, the fovea is displaced with respect to this optic axis creating a new reference axis, the visual axis, forming an angle of approximately 5º horizontally and 2º vertically with the optic axis, as depicted in Figure 1.4. Two nodal points are associated with this visual axis such that a ray following the visual axis directed towards the first nodal point, N, will have a conjugate refracted ray emerging from the second nodal point N′ and directed at the fovea.

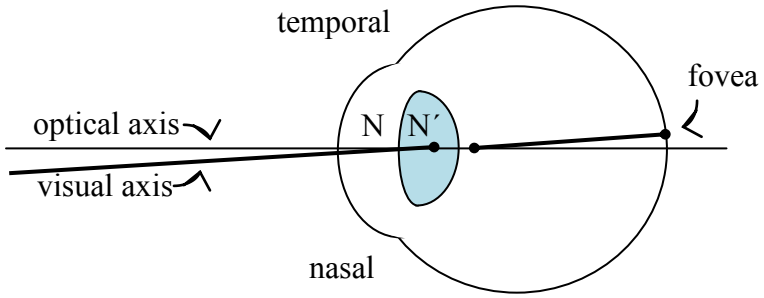

Figure 1.4: Optical and visual axis of the eye. The fovea is displaced slightly from the optical axis, forming a visual axis.

The human eye is also affected by higher order monochromatic aberrations; the most important being spherical aberration and to a lesser extent, coma[11,12]. Positive spherical aberration of the eye occurs when non-paraxial rays intersect the optic axis beyond the paraxial rays, and conversely, negative spherical aberration occurs when paraxial rays intersect in front of the paraxial rays, and may cause a blurred retinal image. Both the cornea and the lens exhibit spherical aberration. For the majority of the population, the cornea exhibits positive spherical aberration even though the anterior surface is aspherically shaped; the conic constant is not large enough to compensate for its spherical shape. The lens exhibits negative spherical aberration, and interestingly enough, the amount of negative spherical aberration of the lens effectively acts against the positive spherical aberration of the cornea to give a lower total spherical aberration of the eye as a whole[13,14]. Coma is another aberration occurring in the human eye resulting from the lack of a common optical axis among the components, also possibly resulting in reduced retinal image quality.

There are also a number of anatomical mechanisms causing these higher order aberrations, varying from individual to individual including pupil size, accommodation, age, retinal eccentricity, and refractive state. A larger pupil size could result in higher aberrations than a smaller pupil size since both paraxial and non-paraxial rays are used to form the retinal image. Spherical aberration changes with accommodation[15,16] and aging[17]. The young eye has positive spherical aberration[17] when relaxed and shifts to negative spherical aberration upon accommodation due to the change in surface curvatures of the lens. Similarly, as the lens ages, it changes in size, surface curvatures, and refractive index[17-24]. This causes a decrease in spherical aberration, resulting in an

overall increase in positive spherical aberration of the eye since the lens can no longer compensate for the positive spherical aberration of the cornea. The aberrations of the eye also increase with increasing pupil radius[25]. As the size of the pupil increases, so does the surface area of the optics of the eye used in the visual system resulting in more error and variability.

1.9.2 Refractive Error Treatments

There are many different options available to correct the refractive errors of the eye, including reading glasses, contact lenses, intraocular lenses (IOLs), and corneal refractive surgery. There are technologies emerging, however, to improve these methods of error correction incorporating customized correction including wavefront corneal refractive surgery, and custom contact and spectacle lenses, to name a few. The appearance of these emerging custom technologies highlights the need for a customized human eye model.

Corneal refractive surgery involves re-shaping the cornea to correct for the common refractive errors and lately some higher order aberrations, in particular spherical aberration. Over the past decade several advances have been made in the customization of refractive surgery. Improvements in corneal topography and thickness measurement techniques have allowed for precise measurements of corneal thickness and curvature prior to treatment to help design the optimal ablation pattern for that particular patient. A technique called wavefront guided or customized ablation[26] has been recently incorporated to offer more corrections than simple defocus and astigmatism. The attempt has been made to correct for higher order aberrations such as spherical aberration, coma, and trefoil[27]. In order to do this, a correction based on calculations including the pre-operatively measured wavefront emerging from the reflection of a spot focused on the patient's fovea is calculated and directly translated to a pattern which is then ablated on the cornea. This measurement technique has also been used very recently in the design of customized contact lens and spectacle design[28, 29]. There exists a problem in this aberration measurement technique in that the pre-operative wavefront measurement system measures the wavefront as it exits the eye, which has been shown to not be necessarily the same wavefront as going into the eye and onto the retina.

The possible need to differentiate between measured data exiting the eye and light entering the eye, as seen by patient, further exhibits the need for an accurate pre-treatment screening using a model of the patient's eye. No system currently exists that tests and models the visual performance of an individual eye as a whole before a refraction correction is made. Current systems apply a correction without modeling the eye as a whole both before and after the correction is made to determine if the correction is proper and accurate. The need for an eye model for both understanding and treatment of an individual's eye is clearly needed.

1.9.3 Biometric and Optic Variation of the Human Eye and Lens

As with many other physiological parameters of the human body, the anatomical and optical characteristics of the eye's components vary widely across the population as do the optical properties of the eye as a whole. The literature describing the various parameters of the whole eye is extensive and will not be discussed in great detail here; a few important parameters are shown. A more detailed description of the biometric parameters of the lens found in the literature is presented since the lens is the focus of this work.

Recent advancement in technology and accuracy in measurements have resulted in greater quality of reported results of measurements of the human eye and lens, therefore only more recent work is shown here. These studies have been done for various purposes, including studies of the effects of aging on the eye, understanding the causes of refractive errors, relationship to genetics, and general population studies. The results of some of these studies measuring parameters of the eye[30-42] are summarized in Table 1.1. Results of studies focusing specifically on measurements of the parameters of the crystalline lens[43-59] are summarized in Table 1.2. Numbers of eyes and/or lenses investigated in these studies range from a few to over a hundred. Since the model proposed in this thesis is at this time restricted to the young lens in the accommodated state since the lenses are measured in-vitro, only results of studies of the lens in the accommodated state are summarized and compared here as lens parameters change drastically after accommodation. Furthermore, as the purpose of showing this data was

to highlight the significant variances in ocular and lenticular parameters in the normal young population, this is well demonstrated from the accommodated lens data alone.

Table 1.1: Recent Measurements of a few of the Biometric and Optical Parameters of the Human Eye

Component	***Range***
Axial Length	23.3mm – 24.9mm
Cornea centre thickness	0.51mm – 0.58mm
Lens Thickness	4.2mm – 4.3mm
Cornea Anterior Curvature	7.60mm – 7.98mm
Cornea Posterior Curvature	6.36mm – 6.70mm
Anterior Chamber Depth	2.91mm – 3.86mm

Table 1.2: Recent Measurements of the Biometric and Optical Parameters of the Human Lens

Component	***Range***
Thickness	3.14 – 7.00mm
Anterior Thickness	0.4 – 1.8mm
Posterior Thickness	0.30 – 2.29mm
Diameter	6.20 – 9.85mm
Anterior Radius of Curvature	4 – 25mm
Posterior Radius of Curvature	-3 – -12mm
Anterior Asphericity	-6.06 – 3.27
Posterior Asphericity	-1.19 – 1.09
Equivalent Index	1.40 – 1.43
Central Index	1.39 – 1.41
Surface Index	1.36 – 1.41
Power	15 – 44D
Focal Length	16 – 75mm
Spherical Aberration	-0.3 – 0.6um
Astigmatism	-1.25 – 0.3um

Several studies have measured the ocular aberrations of the human eye across a large sample group; the most notable being Porter (2001)[60], Castejon-Mochon (2002)[61], Thibos (2002)[62], Cheng (2004)[63], and Sheehan (2007)[64]. These studies measured the wave aberrations on eyes corrected for defocus and astigmatism using a standard pupil size of 6mm. Aberrations of the unaccommodated state were compared here. It was found in all of these studies that the most significant aberration is spherical, with all other aberrations measured having a mean of zero. The spherical aberration of the eyes

reported in these studies ranged from -0.3 to 0.6μm. This indicates that most eyes in the accommodated state suffer from a slight amount of positive spherical aberration, and are free, for the most part, from higher order aberrations.

As can be seen in Tables 1.1 and 1.2, the biometric and optical parameters of the eye and lens vary widely over the human population. Since the mean value of all higher order aberrations is zero, this also illustrates the degree of variability in biometry among the population since any individual is likely to have either slightly positive or slightly negative higher order aberrations. Porter found an uncorrelated, random distribution of aberrations from subject to subject, and also stated that "...We see that the aberrations inherent in the eye's optics across subjects are analogous to the variation displayed when we look at different sets of fingerprints." This illustrates why there is a need for the model of the human eye to be both fully customizable and anatomically correct; the first step of which is a customizable lens model based on these anatomical parameters.

References

[1] R. Munger, M. C. W. Campbell, I. Belanic, "Refractive index distribution in mammalian lenses: test for elliptical symmetry," OSA Technical Digest Series, VSIA, **2**, 76 - 79 (1990).

[2] A. G. Bennett, R. B. Rabbetts, *Clinical Visual Optics,* 2nd ed., (Bath: Butterworth-Heinemann, 1996).

[3] R. W. Young, H. W. Fulhorst, "Regional differences in protein synthesis within the lens of the rat," Invest. Ophth. Vis. Sci. **5,** 288-297 (1966).

[4] U. Muller-Breitenkamp, O. Hockwin, H. Siekmann H., et. al.**, "**Ultraviolet radiation as cataract risk factor: a case report," Dev. Ophthalmol. **27,** 76-80 (1997).

[5] J. J. Harding, K. J. Dilley, "Structural Proteins of the Mammalian Lens: A Review with Emphasis on Changes in Development, Aging and Cataract," Exp. Eye Res. **22**, l-73 (1976).

[6] B. Philipson, "Distribution of Protein within the normal rat lens," Invest. Opthal. Vis. Sci., **8**, 258-270 (1969).

[7] M. C. W. Campbell, "Measurement of refractive index in an intact crystalline lens," Vis. Res., **24**, 5, 409-415 (1984).

[8] B. K. Pierscionek, "Presbyopia: the whens, whys and wherefores. . ." Ophthal. Physiol. Opt. 2000; 20, 2: S17-S19.

[9] Atchison, D. A., Smith, G. *Optics of the Human Eye*. Edinburgh: Butterworth-Heinemann, 2002.

[10] L. F. Garner, M. K. H. Yap, "Changes in ocular dimensions and refraction with accommodation," Opthal. Physiol. Opt. **17**, 1, 12-17 (1997).

[11] J. Liang, D. R. Williams, "Aberrations and retinal image quality of the normal human eye," J. Opt. Soc. Am. A **14**, 11, 2873-2883 (1997).

[12] L. N. Thibos, A. Bradley, X. Hong, "A statistical model of the aberration structure of normal, well-corrected eyes," Ophthal. Physiol. Opt. **22**, 427–433 (2002).

[13] P. Artal, A. Guirao, E. Berrio, D. R. Williams, "Compensation of corneal aberrations by the internal optics in the human eye," J. Vis. **1**, 1-8 (2001).

[14] W. Wang. Z. Wanga, Y. Wang, T. Zuo, "Effects of the Cornea and the Crystalline Lens on the Aberrations of the Complete Eye," Proc. of SPIE 6018: 60180D1-6 (2005).

[15] D. A. Atchison, M. J. Collins, C. F. Wildsoet, J. Christensen, M. D. Waterworth, M. D., "Measurement of monochromatic ocular aberrations of human eyes as a function of accommodation by the Howland aberroscope technique," Vision Res. **35**, 3, 313-323 (1995).

[16] C. Lu, R. Munger, M. C. W. Campbell, "Monochromatic aberrations in accommodated eyes," Ophthal. Vis. Opt. **3**, 160-163 (1993).

[17] A. Glasser, M. C. W. Campbell, "Presbyopia and the optical changes in the human crystalline lens with age," Vision Res. **38**, 209–229 (1998).

[18] S. T. Fontana, et al. "Volume and Depth of the Anterior Chamber in the Normal Aging Human Eye," Arch. Ophth. **98,** 1803-1808 (1980).

[19]J. F. Koretz, C. A. Cook, J. R. Kuzak, "The Zones of Discontinuity in the Human Lens: Development and Distribution with Age," Vision Res. **34**, 22, 2955-2962 (1994).

[20] A. Glasser, M. C. W. Campbell, "Presbyopia and the Optical Changes in the Human Crystalline Lens with Age," Vision Res. **38**, 2, 209-229 (1998).

[21] A. Glasser, M. C. W. Campbell, "Biometric, optical and physical changes in the isolated human crystalline lens with age in relation to presbyopia," Vision Res. **39,** 1991–2015 (1999).

[22] J. F. Koretz, C. A. Cook, P. L. Kaufman, "Aging of the human lens: changes in lens shape at zero-diopter accommodation," J. Opt. Soc. Am. A, **18**, 2, 265-272 (2001).

[23] M. Dubbelman, G. L. van der Heijde, "The shape of the aging human lens: curvature, equivalent refractive index and the lens paradox," Vision Res. **41,** 1867–1877 (2001).

[24] B. A. Moffat, D. A. Atchison J. M. Pope, "Age-related changes in refractive index distribution and power of the human lens as measured by magnetic resonance micro-imaging in vitro," Vision Res. **42,** 1683–1693 (2002).

[25] G. Walsh, W. N. Charman, "The effect of pupil centraton and diameter on ocular performance," Vision Res. **28**, 5, 659-665 (1988).

[26] M. A. Lawless, C. Hodge, "Wavefront's role in corneal refractive surgery," Clin. Exp. Ophthalmol. **33**, 199–209 (2005).

[27] J. Liang, B. Grimm, S. Goelz, J. F. Bille, "Objective measurement of wave aberrations of the human eye with the use of a Hartmann-Shack wave-front sensor," J. Opt. Soc. Am. A **11**, 7, 1949-1957 (1994).

[28] R. Sabesan, T. M. Jeong, L. Carvalho, I. G. Cox, D. R. Williams, G. Yoon, "Vision improvement by correcting higher-order aberrations with customized soft contact lenses in keratoconic eye," Opt. Lett. **32**, 8, 1000-1002 (2007).

[29]J. D. Marsack, K. E. Parker, Y. Niu, K. Pesudovs, R. A. Applegate, "On-eye performance of custom wavefront-guided soft contact lenses in a habitual soft lens-wearing keratoconic patient," J. Refract. Surg. **23**, 9, 960-964 (2007).

[30] P. H. Alsbirk, "Variation and Heretability of Ocular Dimensions," Acta Ophth. **55**, 443-456 (1977).

[31] C. K. Hitzenberger, "Optical Measurement of the Axial Eye Length by Laser Doppler Interferometry," Invest. Optom. & Vis. Sci. **32**, 616-624 (1991).

[32] R. Goyal, et al. "Comparison of laser interferometry and ultrasound A-scan in the measurement of axial length," Acta Ophth. Scan. **81,** 331-335 (2003).

[33] J. Francois, et al. "Ultrasonic Study of 100 Emmetropic Eyes," Ophthalmologica. **175**, 321-327 (1977).

[34] D. A. Goss, et al. "Ocular Components Measured by Keratometry, Phakometry, and Ultrasonongraphy in Emmetropic and Myopic Optometry Students," Optom. & Vis. Sci. **74,** 489-495 (1997).

[35] M. Dubbelman, "The Thickness of the Aging Human Lens Obtained from Corrected Scheimpflug Images," Optom. & Vis. Sci. **78**, 411-416 (2001).

[36] T. Eysteinsson, et. al. "Central Corneal Thickness, Radius of the Corneal Curvature and Intraocular Pressure in Normal Subjects Using Non-Contact Techniques: Reykjavik Eye Study," Acta Ophth. Scand. **80**, 11-15 (2002).

[37] B. K. Pierscionek, "Refractive Index Contours in the Human Lens," Exp. Eye. Res. **64**, 887-893 (1997).

[38] M. C. M. Dunne, et. al. "Normal Variations of the Posterior Corneal Surface," Acta Ophth. **70**, 255-261 (1992).

[39] Manns, et. al. "Radius of Curvature and Asphericity of the Anterior and Posterior Surface of Human Cadaver Crystalline Lenses," Exp. Eye Res. **78**, 39-51 (2004).

[40] B. Gilmartin, "Myopia: precedents for research in the twenty-first century," Clin. Exp. Ophth. **32**, 305-324 (2004).

[41] M. Bechmann, et. al. "Central corneal thickness determined with optical coherence tomography in various types of glaucoma," Br. J Ophthalmol. **84**, 1233–1237 (2000).

[42] B. A. Moffat, D. A. Atchison J. M. Pope, "Age-related changes in refractive index distribution and power of the human lens as measured by magnetic resonance micro-imaging in vitro," Vision Res. **42,** 1683–1693 (2002).

[43] M. J. Howcroft, J. A. Parker, "Aspheric Curvatures for the Human Lens," Vision. Res. **17**, 1217-1223 (1977).

[44] J. F. Koretz, C. A. Cook, J. R. Kuzak, "The Zones of Discontinuity in the Human Lens: Development and Distribution with Age," Vision Res. **34**, 22, 2955-2962 (1994).

[45] A. Glasser, M. C. W. Campbell, "Presbyopia and the Optical Changes in the Human Crystalline Lens with Age," Vision Res. **38**, 2, 209-229 (1998).

[46] A. Glasser, M. C. W. Campbell, "Biometric, optical and physical changes in the isolated human crystalline lens with age in relation to presbyopia," Vision Res. **39,** 1991–2015 (1999).

[47] J. F. Koretz, C. A. Cook, P. L. Kaufman, "Aging of the human lens: changes in lens shape at zero-diopter accommodation," J. Opt. Soc. Am. A, **18**, 2, 265-272 (2001).

[48] M. Dubbelman, G. L. van der Heijde, "The shape of the aging human lens: curvature, equivalent refractive index and the lens paradox," Vision Res. **41,** 1867–1877 (2001).

[49] G. Smith, M. J. Cox, R. Calver, L. F. Garner, "The spherical aberration of the crystalline lens of the human eye," Vision Res. **41**, 235–243 (2001).

[50] P. Rosales, M. Dubbelman, S. Marcos, R. van der Heijde, "Crystalline lens radii of curvature from Purkinje and Scheimpflug imaging," J. Vis. **6**, 1057–1067 (2006).

[51] W. Wang, Z. Q. Wang, Y. Wang, T. Zuo, "Optical aberrations of the cornea and the crystalline lens," Optik **117,** 399–404 (2006).

[52] R. Urs, F. Manns, A. Ho, D. Borja, A. Amelinckx, J. Smith, R. Jain, R. Augusteyn, J. M. Parel, "Shape of the isolated ex-vivo human crystalline lens," Vision Res. **49,** 74–83 (2009).

[53] S. R. Uhlhorn, D. Borja, F. Manns, J. M. Parel, "Refractive index measurement of the isolated crystalline lens using optical coherence tomography," Vis. Res. **48,** 2732–2738 (2008).

[54] S. Kasthurirangan, E. L. Markwell, D. A. Atchison, J. M. Pope, "In Vivo Study of Changes in Refractive Index Distribution in the Human Crystalline Lens with Age and Accommodation," Invest. Ophth. Vis. Sci., **49**, 6, 2531-2540 (2008).

[55] D. Borja, F. Manns, A. Ho, N. Ziebarth, A. M. Rosen, R. Jain, A. Amelinckx, E. Arrieta, C. Augusteyn, J. M. Parel1, "Optical Power of the Isolated Human Crystalline Lens," Invest. Ophth. Vis. Sci. **49**, 6, 2541-2548 (2008).

[56] L. F. Garner, G. Smith, "Changes in equivalent and gradient refractive index of the crystalline lens with accommodation," Optom. Vis. Sci. **74**, 2, 114-119 (1997).

[57] J. F. Koretz, G. H. Handelman, N. P. Brown, "Analysis of human crystalline lens curvature as a function of accommodative state and age," Vis. Res. **24**, 10, 1141-l 151 (1984).

[59] N. Brown, "The Shape of the Lens Equator," Exp. Eye Res. **19,** 571-576 (1974).

[59] N. Brown, "The Change in Shape and Internal Form of the Lens of the Eye on Accommodation," Exp. Eye Res. **15**, 441-459 (1973).

[60] J. Porter, A. Guirao, I. G. Cox, D. R. Williams, "Monochromatic aberrations of the human eye in a large population," Opt. Soc. Am. A **18**, 8, 1793-1803 (2001).

[61] J. F. Castejon-Mochon, N. Lopez-Gil, A. Benito, P. Artal, "Ocular wave-front aberration statistics in a normal young population," Vis. Res. **42,** 1611–1617 (2002).

[62] L. N. Thibos, X. Hong, A. Bradley, X. Cheng, "Statistical variation of aberration structure and image quality in a normal population of healthy eyes," J. Opt. Soc. Am. A. **19**, 12, 2329-2348 (2002).

[63] H. Cheng, J. K. Barnett, A. S. Vilupuru, J. D. Marsack, S. Kasthurirangan, R. A. Applegate, "A population study on changes in wave aberrations with accommodation," J. Vis., **4,** 272-280 (2004).

[64] M. T. Sheehan, A. V. Goncharov, V. M. O'Dwyer, V. Toal, C. Dainty, "Population study of the variation in monochromatic aberrations of the normal human eye over the central visual field," Opt. Express **15**, 12, 7367-7380 (2007).

2. Previous Work

As discussed in Chapter 1, the new lens model will confine its parameters to anatomical features of the lens and will use some accepted properties of the lens GRIN as a starting point. The model testing and simplification will require that the anatomical and optical properties of the lens be measured experimentally.

This chapter summarizes the most important published work with impact on this thesis with respect to experimental measurements of the lens GRIN. Different approaches used to measure the lens GRIN will be covered. Current crystalline lens models will also be discussed, focusing on those models incorporating a GRIN. Finally, published data on the biometry of the crystalline lens will be covered with a focus on the correlations between different anatomical features; a key concept necessary for the simplification of the lens model developed in this thesis. These concepts will lay the foundation which supports the approach taken for the development of the new lens model.

2.1 Crystalline Lens Measurements

The properties of the crystalline lens are difficult to measure in-vivo due to its location inside the eye behind the cornea. The cornea will affect all in-vivo optical measurements of the lens since it is a refracting surface. There has been some success correcting for the effects of the cornea on measurements of the anterior surface shape of the lens. This success has not been repeated for the posterior of the lens which is even more difficult to measure since the optics of the anterior surface and section of the lens must be taken into account. In-vivo ultrasound measurements can provide lens position and thickness measurements; however it is not possible to gather any information on the GRIN of the lens using this technique. No in-vivo measurements have attempted to measure the lens GRIN.

In vitro measurements have their own set of issues. Firstly, in the case of human lenses, once the lens is removed from the eye its shape changes since it is no longer held taught by the zonules. Secondly, the lens must be handled with extreme care once it is removed from the eye since the lens capsule is extremely sensitive to manipulation and

exposure to air. As soon as the lens is removed from its natural environment, its optical properties may change dramatically or it may even opacify, interfering with measurements. If the capsule is removed to explore the different layers destructively the lens becomes even more fragile since it is jelly-like and falls apart extremely easily. Therefore the lens must be handled extremely carefully in preparing it for measurements and held in a special solution during measurements.

Despite these limitations, many in-vitro methods have been used in measuring different properties of the crystalline lens. Most are limited to measuring a few simple properties such as the lens thickness and/or the anterior and posterior surface curvatures. More important to this thesis are the in-vitro experimental methods to investigate the lens GRIN and the summary of the most relevant methods along with results are discussed in the following sections. These include analysis of frozen sections, fibre optic reflectometry, Scheimpflug photography, laser ray tracing, tomography, and magnetic resonance imaging (MRI).

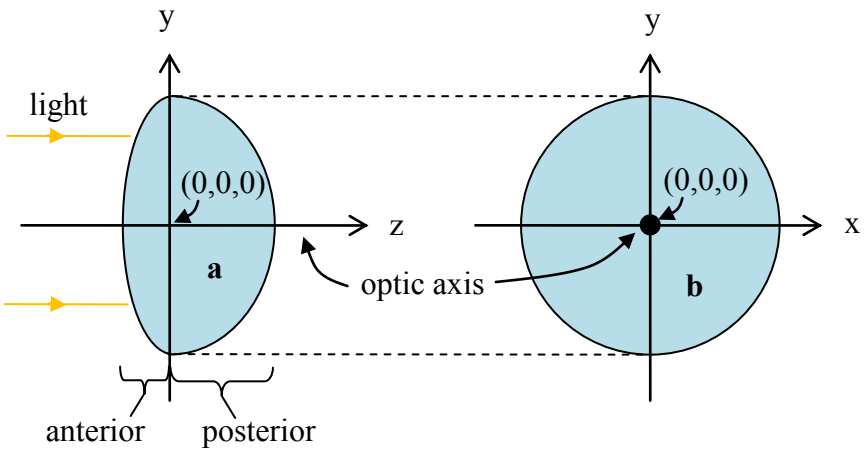

Figure 2.1: Orientation geometry of the crystalline lens. a) Depicts a cross section across the y-z or sagittal plane of the lens. b) Depicts a cross section of the x-y plane or the equatorial plane of the lens. The optic axis lies along the z axis, and the meridional plane is in the x-z plane (not shown)

Before a detailed discussion of lens measurements begins, it is important to cover the nomenclature of orientation of the lens as it is studied, shown in Figure 2.1. The optical axis of the lens as used in the eye is along the z axis. The plane which divides the anterior and posterior surfaces of the lens is called the equatorial plane, represented by the x-y plane at z = 0. In human and most mammalian lenses, this plane is not in the

geometric center of the lens because of the different front and back surface shapes. The sagittal plane of the lens lies in the y-z plane at x = 0 and the meridional plane lies in the x-z plane at y = 0.

2.1.1 Less Precise GRIN Measurement Methods

The different methods of investigating the GRIN can be divided into two groups based on the perceived accuracy of the results. The first group discussed in this section, although perceived as less reliable, has nevertheless contributed significantly to our understanding of the GRIN. The following sections discuss in more detail the methods whose results are widely considered to be more reliable.

Analysis of frozen sections, fiber optic reflectometry, and Scheimpflug photography are techniques that have been used to investigate the GRIN with what is generally considered to be limited accuracy and reliability. A few notable studies using these techniques will be discussed briefly in this section.

After removal from the eye, the lens can be frozen, and sectioned into thin slices. During freezing and sectioning of the lens, the cell structure may not be preserved, however experiments of this type are generally concerned with protein concentration and structure throughout the lens in a larger scale than the cellular level. Different analysis techniques have been applied to study lens sections to provide spatially resolved information on the lens structure. This technique has been used by many authors to either measure the concentrations of the α, β, and γ crystalline proteins within the section or directly measure the refractive index of the section. Studies of the profile of the protein distribution across the lens have been instrumental in further understanding the lens GRIN since the protein concentration is linearly proportional to the refractive index[1]. Nakao (1968)[2] measured the GRIN of sections of rabbit and later monkey and human lenses (1969)[3] in the equatorial and sagittal plane using an optical diffraction technique, and suggested that the refractive index in these lenses can be approximated by concentric iso-indicial curves of circular shape in the equatorial plane and elliptical shape in the sagittal plane with different ellipticities in the anterior half than the posterior half. Philipson (1969)[4] analysed the protein density of thin lens sections in the sagittal and equatorial planes using microradiograpy, and verified his predicted refractive index using

an Abbe refractometer. Philipson proposed that the refractive index profile of the lens can be approximated by considering the lens as a layered structure, with each layer having a mean protein concentration and consequently a mean refractive index associated with it, and also found that these layers are conic at the outer limits of the lens and become more circular towards the lens centre. Bando (1976)[5] and later Fagerholm (1981)[6] used microspectrophotometry to determine the protein distribution of slices of human lenses and found similar results to Philipson. Fagerholm also showed that there is a central nuclear region of constant concentration. In all of these studies mentioned based on sectioning of the lens, the index of refraction (or protein concentration) increases towards the lens centre, following some type of conic profile roughly parabolic in shape in both the sagittal and equatorial planes. Although these techniques provide a general idea of the lens gradient, the process of freezing may alter the actual structure of the GRIN as can the process of sectioning.

Fibre optic reflectometry is another invasive GRIN measurement technique using optical time domain reflectometry. The lens is pierced with a 100μm fibre probe and pulses of light are sent down the fibre into the lens under test. The pulse is reflected in the sample and the intensity of the return pulse is a function of the refractive index. Pierscionek (1994)[7,8] used this method to map the surface refractive index of decapsulated bovine and human crystalline lenses, and later the GRIN inside of bovine[9] and human[10,11] lenses. The GRIN in both lens types was reported to be uniform over most of the inner nuclear region and to decrease in the periphery, in agreement with the frozen sectioning techniques discussed above. Also, the shape of the GRIN in the sagittal plane was not uniformly distributed; the transition in index values increased more sharply anteriorly than posteriorly; also in agreement with refractive index profiles calculated as discussed above. In contrast with the sectioning data, the refractive index values measured at the lens edges near the lens equator were 0.2 higher than reported above, and the refractive indices measured at the anterior and posterior edges of the lenses at the vertex varied from those measured at the equatorial edges in some lenses, indicating that if the crystalline lens is made up of isoindicial contours (surfaces of constant refractive index), these do not necessarily follow the outer lens shape. The issue with this technique is that as the probe moves through the lens, the lens matter is damaged causing

some material displacement which creates inaccuracy in the actual location of the material within an undisturbed lens. Furthermore, the probe can only move along a single bore hole into the lens while displacing it; therefore it is not possible to obtain a full three dimensional map of the lens gradient.

Scheimpflug slit lamp photography[12] is a non-invasive technique which has been used extensively for general measurements of the anterior section of the eye such as the thickness and shape of the cornea and lens. Attempts have been made to study various internal lens structures which are visible using this technique little success. Scheimpflug photography of the eye is based on the Scheimpflug principle, where a photograph of the cross section of lens is obtainable by illuminating the eye using a thin slit (slit lamp) and by tilting the image plane of the camera such that the image plane is conjugate with the path of the illuminating slit through the anterior segment of the eye. An example of the anterior section of the eye obtained using this technique is shown in Figure 2.2. Brown (1973)[13], (1974)[14], (1979)[15], was the first study the lens using Scheimpflug photography showing that it was possible to image the structure of the lens capsule and the edges of cortical and nuclear regions, called zones of discontinuity as seen in Figure 2.2. Different lens regions were correlated to changes in the optical density in the images, these regions were visible due to different light scattering properties of each region, and even though the exact mechanisms of this scattering are largely unknown it was suggested that these regions follow the lens GRIN isoindicial structure. Brown made no attempt to correct the images for the optical effects of the cornea through which the light must return. Koretz (1994)[16] re-analyzed Brown's Scheimpflug images to correct for the effect of the cornea by passing the images through a model of an equivalent eye. Koretz identified the effect of the refraction of the image by the lens itself as a second correction to be made to Brown's images, however this was not done since the relationship between the refractive power of the lens, its GRIN and its location within the eye was unknown. The shapes of the zones of discontinuity did not coincide with any other reports of the isoindicial crystalline lens shapes using other techniques and therefore have not provided any useful information about the lens GRIN. This technique has been proven more effective in studies of accommodation, investigating the changes in surface shape and lens displacement.

In summary, the methods discussed in this section are generally not well suited for GRIN measurements. When the lens is sectioned or probed, its structure is altered by the destructive process. When using Scheimpflug photography, there is no direct evidence that the image intensity profile is linked to the GRIN. If there was evidence, the calculation of the GRIN from the image would still not be possible due to the effects of the rest of the eye's internal optics. These methods (with the exception of Scheimpflug photography) are very useful, however in determining other properties of the lens such as water content, protein concentration, and a few biometric parameters.

Figure 2.2: Scheimpflug photography of human crystalline lens obtained with a Pentacam system. In this image a cataract is visible in the lens centre.

2.1.2 Laser Ray Tracing

The GRIN of crystalline lenses has also been explored in vivo non-destructively using ray tracing by scanning beams. This method was first used by Campbell (1981)[17], (1984)[18] in two different studies to explore rat crystalline lenses as per Figure 2.3. In the first study, the information from Philipson's protein concentration distribution in the sagittal and equatorial planes discussed above was converted into a refractive index distribution in these planes. A parabolic line of best fit of the points was then assumed to define the index values of isoindicial circles in these planes and a spherically symmetric distribution was created, indicated in Figure 2.3 (a). Ray tracing was then performed both experimentally on real rat lenses in the configuration shown and theoretically on the model lens, measuring both spherical aberration and coma, and both ray trace results were within the same order of magnitude but not in exact agreement.

In Campbell's second study, the GRIN was calculated completely from the laser beam ray tracing data using a method developed by Chu(1977)[19] to find the GRIN of spherically symmetric fibre optic preforms and later modified by Barrell and Pask (1978)[20] for elliptical preforms. This method is used extensively in this thesis and its mathematical basis is discussed in greater detail in Chapter 3. A full mathematical derivation of this method is presented in Appendix A for reference. In these measurements, the lens was surrounded by a fluid matching the refractive index of the lens surface. The assumption was made that the lens is rotationally symmetric about the optic axis, which for rat lenses is completely reasonable since these lenses have symmetric anterior and posterior sections. Experimental laser ray tracing was then performed on real rat lenses by shining a reference beam through the lens optical axis and scanning a second beam at varying distances from the equatorial axis, z, also indicated in Figure 2.3 (b), to obtain the exit angle ψ as a function of z. These data were then transformed to a refractive index distribution $n(r)$ which is the refractive index as a function of radial distance from the lens centre. Campbell assumed an ellipsoidal shape for the isoindicials (surfaces or contours of constant refractive index) in this study compared to the previous study above where they were concentric with the lens surfaces, as indicated in Figure 2.3 (b). The actual desired ellipsoidal distribution, n, was then derived from this spherical distribution by applying the following equations:

$$n = n_o^2\sqrt{1 - 2\Delta N(R)} \tag{3.1}$$

$$R^2 = \left(\frac{z}{\rho_z}\right)^2 + \left(\frac{y}{\rho_e}\right)^2 \tag{3.2}$$

$$\Delta = \Delta_{eq}(\rho_z/\rho_e) \tag{3.3}$$

where the refractive index is in a plane (z, y), Δ_{eq} is the difference in index between the lens edge and centre, n_o is the refractive index at the lens centre, $N(R)$ is a general function to be determined and ρ_z and ρ_e are the half lengths of the lens along the optic (z) and equatorial (y) axis, respectively. The refractive index distribution along the optic axis was then determined using the above equations and compared to Philipson's data along the same axis. Fairly good agreement was found with both data sets following approximately parabolic shapes. These data however were not verified optically in any

way with real rat lenses and therefore the accuracy of the results of this study are questionable.

Chan et al. (1988)[21] and Pierscionek et al. (1988)[22], (1989)[23,24] also used laser beam ray tracing to investigate bovine and human lenses. These groups also based their research on the work of Chu but added a correction term to eliminate the need for the immersion medium and lens surface to be index matched. The GRIN calculation involved for these lenses is more complex since bovine and human lenses lack the anterior / posterior symmetry about the equatorial axis. Instead they measured the equatorial (x-y) plane GRIN, which in these lenses is rotationally symmetric and

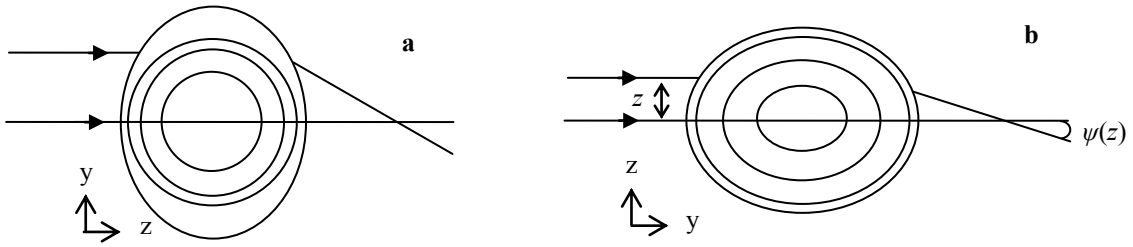

Figure 2.3: Schematic showing Campbell's laser ray tracing set-up through the sagittal (a) and meridional (b) planes of crystalline lenses using beams of approximately 0.5mm in diameter. Also indicated are the different modeled index distributions with isoindicial contours not concentric (a) and concentric (b) with the surface of the lens.

thus can be calculated using Chu's method. In the first study, the 3D GRIN profile of bovine lenses was estimated in a similar fashion used by Campbell as described above by projecting the GRIN measured in the equatorial plane on to the sagittal plane by rotating a family of concentric elliptical isoindicial contours in the x-y plane about the z axis. This was accomplished by using an elliptical function to describe $N(R)$ in equation 3.1. Ray tracing was then performed in the sagittal plane both theoretically using the modeled lens and experimentally with real bovine lenses and results compared were on the same order of magnitude but not in very good agreement. In their later studies, human lenses were modeled with elliptical isoindicial contours in the sagittal plane following the shape of the outer lens surfaces with different anterior and posterior sections to more closely match the lens anatomically. The refractive index in the equatorial plane of a human lens was compared to that measured by Nakao and it was found that while both GRINs followed a more or less parabolic shape, the profile used by Pierscionek was flatter in the

central regions and steeper at the edges. Experimental results were also compared to a GRIN proposed by Pomerantzeff (1972)[41] (discussed later), and the shape was in agreement in the central regions but not at the edges. The refractive index profile of the model of a human lens in the sagittal plane was then compared to Nakao and Pomerantzeff's results and differences were again present at the periphery of the lens; this time greater discrepancies were apparent as Pierscionek's model was steeper at the edges. Further comparisons with data from Fagerholm (discussed above) were made by converting the modeled refractive index profile in the sagittal plane to a protein concentration profile, and even though better agreement was found, they still were not exactly the same shape. Theoretical and experimental ray tracing was then performed on the model and real lenses, respectively, and it was found that the model could not predict the real ray paths as the results were not in agreement.

The elliptical symmetry function of the isoindicial contours assumed by Pierscionek was tested by Munger et al. (1990)[26]. Six different mammalian species (human, rabbit, rat, squirrel, cow, and pig) were tested by ray tracing through the lens along the x, y, and z axes and calculating the function N(R) in equation 3.1 for both planes. It was found that the functions N(R) for the x and y axes were similar, however the function N(R) along the z axis was not the same, and therefore these lenses fail the elliptical symmetry test. This indicates that the isoindicial contours follow some other function which still remains unknown.

2.1.3 Tomography

Tomography is a more recent non-invasive measurement method used in studying the crystalline lens GRIN both in vivo and in vitro. Tomography, very simply, is a method of obtaining a cross-sectional image of a sample non-destructively by calculating ray paths through a sample. These two dimensional images may then be used to create three dimensional constructs.

Acosta (2005)[27] used tomography in studying the crystalline lens of the fish. The tomographical information in this instance was obtained using a laser ray tracing system. The slopes of the refracted rays leaving the lens were recorded and the lens parameters were calculated from these slopes. The ray trajectories through the lens were then

calculated as a function of the distribution of the lens refractive index in 2D planes across the lens. A discussion of the theory is not necessary for completeness; basically the outcome was a three dimensional composition of the refractive index distribution calculated by applying a tomographic inversion algorithm to the two dimensional sections. In the case of the fish lens, it was found to be spherical and therefore rotationally symmetric in every plane.

Human lenses, as already discussed, are only rotationally symmetric in the plane perpendicular to the optical axis which makes the inversion algorithm used in tomography more difficult. A new method was developed by Vazquez et. al., (2006)[28] to account for this asymmetry. This new method was used on porcine lenses which exhibit asymmetry in the anterior and posterior halves. For the rotationally symmetric fish lens, only one projection of rays was necessary to reconstruct a three dimensional refractive index profile. With the porcine lens, however, rays in two planes were required to reconstruct the GRIN in three dimensions. The resulting model was a lens with isoindicial contours following an elliptical profile in the sagittal plane; as was done by Chan et. al (1988)[21] discussed above. The outer lens surface, however, was not restricted to follow the same contours as the lens GRIN. These results were inconclusive, however since two different GRIN profiles were found that matched the experimental results; one having a steeper profile and one having a more flat profile and therefore the GRIN still remained to be unknown. Vazquez could not find a physiological reason why one model would represent the lenses better than the other and a single solution could not be justified.

Another tomographic method that has been used to study the crystalline lens is optical coherence tomography (OCT)[29]. OCT is an interferometric non-invasive tomographic technique. The basic OCT set up is an interferometer, with one arm scanned over the sample to give its reflectivity profile. A cross sectional image is achieved by laterally combining a series of scans while varying the depth scanned into the sample. OCT is a good choice for the optical and biometric study of ophthalmic tissues since it has a high resolution, is non-destructive, and can penetrate tissues up to a few millimeters. A few authors have used OCT to study the anterior chamber of the eye including the lens.

OCT was used by Verma et al. (2007)[30] to study the GRIN profile of the fish lens in vivo. Their study focused on the fact that OCT directly measures the optical path of light traveling through a medium. The backscattered or reflected light from the sample is detected only when the path lengths of the sample and reference arms are equal; since the path length of the reference arm is known the position of the reflecting surface can be found. The actual path of the rays inside the lens was computed using ray tracing with an assumed polynomial form for the refractive index profile. Depth scans were performed at different locations along the lens in the meridional plane. In these scans, the optical path length was measured and then fit with the optical path calculated for the estimated refractive index profile. The gradient index profile was assumed to be a 4^{th} order polynomial, with only even terms considered since the index of the fish lens is spherically symmetric in all directions. Beams were scanned along two orthogonal planes and the index profile along both planes was found to be the same, as expected for a spherical fish lens. A lens was modeled optically using the calculated GRIN and its performance was in agreement with other author's results[32] of the optical performance of real fish lenses.

OCT has recently been used by de Castro et al. (2010)[31] to reconstruct the GRIN of pig crystalline lenses. The GRIN in this method was retrieved by the measurement of the posterior surface of the lens distorted by the anterior surface and GRIN within the lens by OCT. The posterior surface is distorted since the light must travel from this surface through the GRIN and out the posterior surface. A 4-variable model of the GRIN was first assumed where the GRIN was described as a monotonically increasing function from the lens edge. The centre position of the lens was assumed to be a function of the total lens thickness, the anterior and posterior surfaces were modeled as conic sections and the GRIN was assumed to follow these surfaces. The variables of the model were fit based on the OCT data retrieved. The resulting GRIN of the lenses was then modeled optically and negative spherical aberration was calculated, in agreement with others' measurements on real lenses. None of the lenses tested were measured optically for comparison with the modeled results. A real drawback to this method is that the GRIN distribution is dependent on the form of the model used and one model could not be chosen as unique.

2.1.4 Magnetic Resonance Imaging

Since 2005, the evolution of high resolution magnetic resonance imaging (MRI), with resolutions of less than 5μm/pixel has made it possible to study the GRIN of crystalline lenses, and several authors have studied the crystalline lens structure and GRIN in vitro using this technique.

Moffat (2002)[33] used MRI to non-invasively calculate the refractive index distribution across the sagittal plane of human crystalline lenses. Lens protein solutions were first made by pulverizing different regions of lenses to establish the relationship between the refractive index of lens protein solutions from different lens areas and the relaxation rate of these solutions measured by MRI. These relations were then used to determine the GRIN isoindicial contours in the sagittal plane of whole intact lenses from MRI images in that plane. The resolution of the MRI process in this case was 20μm/pixel. The shape of the contours indicated that the outer isoindicial contours of the lens did not follow the shape of the lens surface. The refractive index profiles in the equatorial and sagittal planes were found to have the same parabolic shape suggested by the studies discussed above; however these results were not compared with other's results. These results were not verified optically.

Jones (2004)[34] also used MRI to map the GRIN of porcine crystalline lenses in the sagittal plane. The same measurement procedure was applied as above, however this time the technique was verified optically by comparing ray tracing on the model obtained from the MRI measurements to experimental ray tracing measurements with the same lenses. There was a high degree of error in estimating the refractive index in the central lens region by MRI, and therefore the focal lengths of the model could only be calculated using non-paraxial rays since the refractive index of the central region was too noisy. The focal lengths of the experimental and modeled ray tracing results were in good agreement using only the peripheral rays; however the spherical aberration results were not in good agreement which Jones attributed to the noisy central lens measurements.

Jones et al. (2005)[35] then continued this research to measure the GRIN of human lenses using MRI. The GRIN obtained from the MRI measurements was optically modeled by ray tracing for 20 human lenses and these modeling results were compared

with experimental ray tracing measurements using the same lenses. The focal length and longitudinal spherical aberration results for both the theoretical and experimental results were in very good agreement. Attempts were made to fit this distribution to the form used by Castro (2010)[31]; however it was found that it was impossible to model the lens using this form due to the lack of symmetry between the anterior and posterior lens sections in human lenses, as described in section 2.1.2.

2.1.5 Summary of Crystalline Lens GRIN Measurements

Directly measuring the GRIN of the human lens with any degree of precision is an extremely difficult task. The laser ray tracing method is able to produce a GRIN measurement non-invasively, however has major drawbacks. The GRIN is not directly measured in the sagittal plane; it is inferred from the equatorial plane with the assumption of elliptical symmetry in the sagittal plane. In contrast to laser ray tracing, tomographic methods directly measure the optical path through the sagittal plane. This method is also non-invasive; however the method does not lead to a unique solution and thus is inconclusive. A major drawback of OCT, similar to laser ray tracing, is that the GRIN measurement is dependent on a predetermined form which is later fit to measured data. MRI has been shown to be a useful tool for measuring the GRIN of individual crystalline lenses however it has its limitations as well in that the technique assumes a direct relationship between the water content and refractive index of the lens homogenates.

Regardless of all of these differences in measurement techniques, there has been some general agreement on the structure of the GRIN of the crystalline lens. The distribution in the equatorial plane has been measured to be rotationally symmetric. The GRIN is distributed by some kind of conic form, mostly parabolic in shape from the lens edges to the nuclear region where it is uniform. Also, the isoindicial contours within the lens follow some type of conic form, mostly elliptical in shape that does not necessarily follow the shape of the lens capsule.

2.2 Crystalline Lens Models

2.2.1 Basic Crystalline Lens Models

Most models of the crystalline lens are incorporated into a schematic model of the eye and as such are designed to make the full eye model compliant with measured properties of the eye. The simplest lens models use a single homogeneous index crystalline lens using either spherical or aspheric surfaces. The most commonly used models of this type include the Gullstrand (1909)[37], Gullstrand-Emsley[38], Le Grand[39], and Indiana[40] eye models. More complex models have also been developed which describe the lens as a 2 layer model, with a different index of refraction for each layer and different surface shape at the lens surface and the interface between the layers. These homogeneous models will not be looked at in detail since it is known that they are not anatomically correct and are not applicable to this work, however it should be known that they exist. The weakness of these models is the absence of a lens GRIN and as such they cannot predict the optical properties of the lens including its higher order aberrations. For this reason the rest of this section will focus on the description of GRIN models of the lens.

2.2.2 GRIN Crystalline Lens Models

As discussed in the previous section, it is known from physical measurements that an index gradient exists inside the lens. Several authors have used results of these GRIN measurements with many different approaches. Since there have been a large number of GRIN crystalline lens models proposed over the years, only those which have been validated by comparison to measured properties of real crystalline lenses will be discussed here as these are relevant to the goal of this thesis.

A crystalline lens model incorporating a non-uniform GRIN was computed by Nakao for the rabbit (1968)[2] and later for the monkey and human (1969)[3]. These models were derived from refractive index measurements discussed in the previous section. The crystalline lenses in these models were described by discrete isoindicial shells to approximate the measured continuous refractive index distribution. The calculated isoindicial curves in the sagittal plane were families of concentric ellipses, with different

eccentricities in the anterior and posterior halves; the isoindicial curves calculated for the equatorial plane were concentric circles. Several models were constructed varying both the refractive index at the lens centre and the rate of increase of the index from the edge to the centre of the lens. These models were then used for theoretical ray tracing experiments. While these models were a good first attempt at a crystalline lens model with a gradient refractive index distribution, Nakao did not compare the theoretical results to actual physical measurements of optical properties. Hughes (1979)[41] later compared Nakao's rabbit models with actual measurements of rabbit crystalline lenses and found that the model was not a good predictor of the experimental results.

Pomerantzeff (1972)[42]produced a model of the GRIN of the human crystalline lens based on the "onion-like" structure of the lens, from what was known at the time about crystalline lens formation and the addition of layers of lens fibre cells as the lens grows. This model assumed a shell structure with 100 layers; the outermost layer matched the surface shape and the core had spherical symmetry. The refractive index increased smoothly towards the central core, which had a constant index. The shell interfaces were described by a 3rd order polynomial with different curvatures for the anterior and posterior of the lens, joined abruptly at the lens equator. The surface curvatures and thickness of this lens model were based on physical measurements of human lenses. Unfortunately, sufficient physical data of human crystalline lenses was not available at the time the model was made to base this lens model on actual refractive index measurements, however Pierscionek later compared experimental data with ray tracing measurements (already discussed) and did not find any agreement. This model was later refined by Pomerantzeff et al. (1984)[43] and tested against lens spherical aberration measurements which were derived from aberration measurements of whole eyes in vivo. The refined model contained 200 layers and the lens thickness and curvature measurements were updated using more accurate experimental measurements from human crystalline lenses. This model had a varying GRIN parameter, and unfortunately several different GRIN models were within good agreement of the experimentally measured spherical aberration and the actual GRIN was still unknown.

Jagger (1990)[44] constructed individual models of crystalline lenses of the cat. These models were based on refractive index measurements of frozen sections in the

sagittal plane using an Abbe refractometer on sectioned lenses of five cats' left eyes. Isoindicial contours of the cat lenses were generated from these measurements and individual eye models were constructed for each lens. The isoindicial curves followed an elliptical shape different from the lens curvature; each isoindicial curve consisted of an anterior and posterior section smoothly joined at the centre, with the anterior curvature less than the posterior curvature. The model lenses had rotational symmetry in the equatorial plane. The GRIN of the lens in the equatorial plane followed a parabolic profile. Lenses from the same cat but from the right eye, were measured optically by laser ray tracing to test the model. These results were compared to theoretical ray tracing performed on the model lenses and good agreement was found in terms of the paraxial focal length and longitudinal spherical aberration. This technique did suffer the weakness however that the lens core could not be measured because there was not sufficient optical contact between the core of the lens and the refractometer.

Smith (1991)[45] was the first to study the optical modeling of the crystalline lens of the human describing the lens with both a GRIN and aspherical surfaces. Elliptical isoindicial curves were used, based on the work by Nakao (1968)[2] and Jagger (1990)[43]. The GRIN shape in the equatorial plane was modeled after that measured by Pierscionek (1989)[24] and fit to a power function where the GRIN was described as increasing radially from the lens edge. Four different lens models were studied. The first model consisted of a GRIN with isoindicial contours concentric with the outer lens surface with equal anterior and posterior surface curvatures. The second model was the same as the first except the isoindicial contours were asymmetrically elliptical, with the anterior surface curvature less than the posterior surface curvature. The third model also had asymmetrically elliptical isoindicial contours; however these contours did not follow the shape of the anterior and posterior lens surfaces; they were modeled by ellipses with different eccentricities than the lens surface. Model four has isoindicial surfaces with a variable concoid surface shape, not necessarily elliptical with a non-smooth joint at the equator, in contrast to the first three models which had smooth equatorial joints. The lens surfaces of this last model were described by conic aspheres, the aspheric shapes were taken from physical measurements of the surface radii of curvature measurements of

human lenses. From this study it was found that the fourth model most closely matched physical measurements of real lenses equivalent power and spherical aberration.

Another shell model of the lens was produced by Al-Ahdali (1995)[46]. A specific laminated structure of the crystalline lens was created to determine the effect of such a structure on the optical characteristics of the entire human eye. The structure used for this study had 600 concentric shells 5.6μm thick with the refractive index increasing exponentially from the periphery towards the lens centre which was proposed to mimic the laminated structure of the lens fibres. The shells of this model had different front and back curvatures abruptly joined at the equator. This model was loosely based on the model of Pomerantzeff (1972)[33], and as such also had a central core region of constant refractive index. A numerical ray tracing procedure was then used in a model of the whole eye to study its optical performance with such a lens. The parameters of the lens were varied such that the outcomes of the numerical ray tracing matched physical measurements of human eyes for focal length and spherical aberration. It was found that a constant refractive index core gave good agreement with accepted experimentally measured values for the focal length of the eye. Also, the laminar structure of the lens was compared with a continuous structure with the same index gradient and the laminar structure showed no appreciable reduction of spherical aberration of the eye as a system. If the lens was modeled properly, it would exhibit positive spherical aberration to "cancel out" the negative spherical aberration of the cornea and reduce the spherical aberration of the eye as a whole as discussed in Chapter 1.

Liou (1997)[47] developed a model of the eye with a gradient index crystalline lens using empirical values to produce a model as close in structure anatomically to the human eye as possible. This model is also known as the Liou Brennan eye model and is used extensively in eye modeling research. The lens surfaces were aspheric in shape, adapted from measurements by Brown (1973)[13] and the GRIN followed a parabolic shape based on measurements by Pierscionek (1989)[24]. The core was assumed to be spherical with a uniform refractive index. Equivalent optical power and spherical aberration of the entire eye were modeled using ray tracing and results were compared to other schematic model eyes having lenses with constant refractive index. It was found that incorporating a GRIN into the model eye served to reduce the spherical aberration of the model eye as a

whole, as the spherical aberration of this model was lower than that of other schematic model eyes. The calculated spherical aberration for this model eye was also in better agreement with experimental results of measured spherical aberration of real human eyes. The experimental results used, however, were average results on human eyes and differences existed when compared with results of individual human eyes.

Navarro et al. (2007)[48] developed a flexible GRIN model of the human lens with isoindicial surfaces concentric with the outer lens surfaces. The lens was modeled as a power function, following the GRIN derived by Smith from Pierscionek's data. The equatorial plane of this model was modified to follow a concoid surface such that the intersection of both hemispheres did not follow a flat plane and is instead determined by the geometry of the external surfaces. The human lens data by Jones et al. (2005)[36] obtained using MRI discussed previously was used to produce two GRIN models, one for each lens individually and another using a general model using the variable describing the increase in index along the optical axis as a function of age. Good agreement was found with the modeled GRIN and the GRIN of the individual lenses, however there were differences in the GRIN when the general model was compared to each of the individual's lenses modeled as a function of age. The focal length of the general model lens (with GRIN varied for age) was compared to the individual experimental results for the lenses and it was found that the model was off by about 6D.

2.2.3 Summary of Crystalline Lens GRIN Models

Most authors agree upon using isoindicial contours having some form of conic shape to describe the refractive index distribution. Models that have the best performance when compared to experimental crystalline lens measurements have used different eccentricities for the anterior and posterior halves of the lens. The refractive index profile that is in best agreement with experimental measurements for both paraxial and wide angle models follows some kind of parabolic shape that is constant in the centre, for both the equatorial and sagittal planes. Consequently these isoindicial contours and parabolic-like GRIN distributions are closer to what has been measured experimentally.

For the outer lens surfaces, better optical performance was achieved using models having aspheric surfaces. In more recent crystalline lens measurements, aspheric surfaces have been measured and when these real surfaces were incorporated into lens models having a GRIN, the optical performance of these models more closely matched experimental spherical aberration data. Furthermore, if the isoindicial contours did not follow the outer aspheric surfaces, better results were achieved. Consequently, this more closely matches anatomical measurements as the lens fibres do not necessarily follow the surface capsule of the lens, as discussed in Chapter 1.

2.3 Crystalline Lens Biometry and Optical Relationships

Several authors have studied and reported striking relationships between the biometric and optical parameters of the crystalline lens which are of great interest to this thesis since the number of parameters of the crystalline lens model could potentially be reduced using these relationships, especially if they can be based on clinically available information. It is also quite remarkable that these relationships exist due to the highly non-linear interaction between the parameters of the crystalline lens and the high degree of variation (shown in Chapter 1) among these parameters across the population.

2.3.1 Bovine, Porcine, and Human lens relationships

Good indications of several biometric relationships were found by Pierscionek (1992)[49] in a study of the growth related changes of bovine crystalline lenses. In this study, the dimensions, focal lengths and lens weights were determined for 23 crystalline lenses from cows ranging in age from 2 months to 19 years. The lens thickness, and diameter were determined from digitized images. To calculate the radii of curvature, the relation curvature = (equatorial radius)^2/(sagittal thickness) was used; therefore a spherical lens surface was assumed. The lens focal length was determined using a laser ray tracing technique previously discussed. Non- linear relationships were established between the total lens volume and lens weight, and lens dimensions (diameter, anterior thickness, posterior thickness, total thickness) and lens weight. Although the author did not specifically calculate a relationship between the various lens dimensions and the anterior and posterior lens radii of curvature, it is was clear that a non-linear relationship

exists since the plot of anterior and posterior lens surface curvatures increased non-linearly with lens weight, and also the plot of the various lens dimensions also increased linearly with lens weight. Also, the statement was made that the relationship between the anterior and posterior radii of curvature remained constant at a ratio of 1.19. Non-linear relationships were also apparent between the measured lens focal length and lens weight indicating possible linear correlations between the focal length and lens dimensions.

Vilupuru (2001)[50] measured optical and biometric interrelationships of the porcine crystalline lens. Lens weight, focal length, spherical aberration, surface curvatures, thickness, and diameter were measured for 20 isolated pig lenses. The power and spherical aberration of each lens was measured by laser ray tracing, and the curvature and thickness of each lens was determined from measurements from digital profile images. The radii of curvature were calculated from fitting 40 points manually marked along the entire lens surface to spherical curves. Therefore no asphericity data was collected from these lenses as it was found that the spherical curves fit very well to the lens curvatures. Significant linear relationships were found between the anterior and posterior radii of curvature, and between the lens thickness and anterior radius of curvature, for example: anterior radius of curvature = -1.240 x posterior radius of curvature – 0.826 ($r = -0.922$). A significant linear relationship was also found between the lens focal length and anterior radius of curvature ($r = 0.503$). As above, no significant correlation was found between the spherical aberration and any other measured parameter of the crystalline lenses.

Glasser (1999)[51] studied the optical and biometric changes in human crystalline lenses as a function of aging. 38 human crystalline lenses ranging in age from 5 to 96 years were studied in vitro. These properties were measured using the same technique as Vilipuru described above. It was found in this study that the lens focal length was significantly linearly correlated with both the anterior and posterior surface curvatures ($r^2 = 0.656$ and 0.570, respectively). It was also found that the anterior radius of curvature was very highly inversely linearly correlated with the posterior radius of curvature since each of these was well correlated with the focal length. Also found in this study was very good linear correlation between the lens equatorial diameter and the anterior and posterior radii of curvature. Another finding was the inverse proportionality between the

radii of curvature and the constant of the x^2 term in the parabolic equation describing the surface shape for both the anterior and posterior radii of curvature. All of these findings were independent of age. The authors concluded that the average focal length of the lens can be predicted with a high level of confidence from the surface curvatures, (focal length = 3.955 x anterior radius of curvature + 13.853, $r^2 = 0.656$) and either the anterior or posterior surface curvature can be predicted from knowledge of the other. The spherical aberration was found to be significantly linearly proportional to age, with spherical aberration increasing with age from negative to positive. Spherical aberration was not found to correlate with any other measured parameter.

Manns (2004)[52] studied the relationships between the radius of curvature and asphericity of the anterior and posterior surface of the human crystalline lens. Thirteen pairs of human lenses ranging in age from 46 to 93 years were measured using a topographic measurement technique. This measurement system projected a grid on the lens surface and measured the height of the surface at each grid point with respect to a reference height. From these measurements the asphericity and radius of curvature of each lens was calculated. A significant linear biometric relationship was found in this study between the anterior asphericity and the anterior curvature (anterior asphericity = 1.22 x anterior curvature - 8.10, r = 0.84). A less significant (r = 0.39) linear biometric relationship was found between the anterior and posterior radii of curvature. No relationship was found between the posterior asphericity and posterior radius of curvature. The posterior radius of curvature in this study proved difficult to measure due to attachment of the vitreous to the posterior of the lens surface. This resulted in a lower number of lenses with the posterior successfully measured (16 lenses) relative to the larger number of successful anterior lens' measurements (24 lenses). Manns suggested that this was the reason why the posterior shape factor is not as strongly correlated to the posterior radius of curvature, as well as why there was no correlation measured between the anterior and posterior radii of curvature as was measured in other studies. This study also demonstrated the importance of measuring the surface shape of the lens all the way out to the periphery as opposed to only in the central zone, showing as an example very different results when comparing fits to a 3mm zone and a 6mm zone. If only the central lens region is used to measure the surface shape, the asphericity could be incorrectly

measured since the lens edges are important in this calculation. If the central lens region is used to calculate an elliptical aspheric surface, the central flatter region will produce incorrect results for the total lens surface shape. Also discussed in this paper is the importance of a conic section fit as opposed to a polynomial fit to the lens surface as had been used previously by other authors. Other authors had fit the lens to a 2^{nd} order polynomial with very good results indicating that the outer surface of the lens is parabolic in shape. The importance of using a conic section to fit the lens surface shape was illustrated explicitly by fitting both a conic section and three different polynomials (2^{nd}, 4^{th}, and 6^{th} degree) to the same lens surface. All three formulae demonstrated excellent fits with r-squared values greater than 0.9999, however four formulae had different asphericities. It was concluded that the conic section provided the most reliable measure of the shape of the lens.

2.3.2 Summary of Lens Biometric and Optical Relationships

Several strong linear relationships have been found between different biometric and optical parameters of the crystalline lens. The strongest linear relationships from all of the studies mentioned here are the relationships between the anterior and posterior radii of curvature, and between the anterior radii of curvature and the measured lens focal length. It is important to note that all authors mentioned here, with the exception of Manns and Vilupuru, used digitized profile images to calculate the radii of curvature using a fraction of the central portion of the lens. Manns pointed out the importance of using the full lens surface in the radii of curvature measurements, and also using a conic section to find the aspheric shape of the lens. Nonetheless, these optical and biometric linear relationships are crucial in the development of any lens model as they can significantly decrease the number of unknowns.

References

[1] K. Barer, S. Joseph, "Refractometry of living cells," Quart. J. Micro. Sci,. **95**, 399–423 (1954).

[2] S. Nakao, S. Fujimoto, "Model of Refractive-Index Distribution in the Rabbit Crystalline Lens," Journ. Opt. Soc. Am. **58**, 8, 1125-1130 (1968).

[3] S. Nakao, T. Ono, R. Nagata, I. Iwata, "The distribution of refractive indices in the human crystalline lens," Jap. J. Of Clin. Opthal. **23**, 41-44 (1969).

[4] B. Philipson, "Distribution of protein within the normal rat lens," Invest. Ophthal. Vis. Sci. **8**, 258-269 (1969).

[5] M. Bando, A. Nakajima, M. Nakagawa, T. Hiraoka, "Measurement of Protein Distribution in Human Lens by Microspectrophotometry," Exp. Eye Res. **22**, 389-392 (1976).

[6] P. P. Fagerholm, B. T. Philipson, B. Lindstrom, "Normal human lens, the distribution of protein," Exp. Eye Res. **33**, 615-620 (1981).

[7] B. K. Pierscionek, "Refractive Index of Decapsulated Bovine Lens Surfaces Measured with a Reflectometric Sensor," Vis. Res. **34**, 15, 927-1933 (1994).

[8] B. K. Pierscionek, "Refractive index of the human lens surface measured with an optic fibre sensor," Ophth. Res. **26**, 1, 32-35 (1994).

[9] B. K. Pierscionek, A. Belaidia, H. H. Bruun, "Optical development in the foetal bovine lens." Exp. Eye Res. 77, 639–641 (2003).

[10] B. K. Pierscionek, "Refractive Index Contours in the Human Lens." Exp. Eye Res. **64,** 887-893 (1997).

[11] B. K. Pierscionek, "Variations in Refractive Index and Absorbance of 670-nm Light with Age and Cataract Formation in Human Lenses." Exp. Eye Res. **60**, 407-414 (1995).

[12] T. Scheimpflug, "Improved Method and Apparatus for the Systematic Alteration or Distortion of Plane Pictures and Images by Means of Lenses and Mirrors for Photography and for other purposes." 1904, British Patent no. 119.

[13] N. Brown, "The Change in Shape and Internal Form of the Lens of the Eye on Accommodation," Exp. Eye Res. **15**, 441-459 (1973).

[14] N. Brown, "The Shape of the Lens Equator," Exp. Eye Res. **19**, 571-576 (1974).

[15] N. Brown, "Photographic Investigation of the Human Lens and Cataract," Survey of Ophthal. **23**, 5, 307-314 (1979).

[16] M. C. W. Campbell, A. Hughes, "An analytic, gradient index schematic lens and eye for the rat which predicts aberrations for finite pupils," Vis. Res. **21,** 1129-1148 (1981).

[17] M. C. W. Campbell, "Measurement of refractive index in an intact crystalline lens," Vis. Res. **24**, 409-415 (1984).

[18] J. F. Koretz, C. A. Cook, J. R. Kuszak, "The Zones of Discontinutity in the Human Lens: Development and Distribution with Age,"

[19] P. L. Chu "Nondestructive measurement of index profile of an optical-fibre preform." Electron. Lett. **13,** 736-738 (1977).

[20] Barrell, K. F., Pask, C., "Nondestructive Measurement of Noncircular Optical Fibre Preforms." Opt. Comm., 1978; 27, 2: 230 – 234.

[21] Chan, D. Y. C., Ennis, J. P., Pierscionek, B. K., Smith, G., "Determination and modeling of the 3-D gradient refractive indices in crystalline lenses." App. Opt., 1988; 27, 5: 926-931.

[22] B. K. Pierscionek, D. Y. C. Chan, J. P. Ennis, G. Smith, R. C. Augusteyn, "A non-destructive method of constructing three-dimensional gradient index models for crystalline lenses : I. Theory and experiment," Am. J. Optom. Phys. Optics **65**, 481 – 491 (1988).

[23] B. K. Pierscionek, "Growth and Ageing Effects on the Refractive Index in the Equatorial Plane of the Bovine Lens," Vis. Res. **29**, 12, 1159-1766 (1989).

[24] B. K. Pierscionek, D. Y. Chan, "Refractive index gradient of human lenses," Optom. Vis. Sci. **66**, 12, 822-829 (1989).

[25] O. Pomerantzeff, H. Fish, J. Govignon, C. L. Schepens "Wide-angle optical model of the eye," Opt. Acta **19**, 387–388 (1972).

[26] R. Munger, M. C. W. Campbell, I. Belanic, "Refractive index distribution in mammallian lenses: test for elliptical symmetry," OSA Technical Digest Series, VSIA, **2**, 76 - 79 (1990).

[27] E. Acosta, D. Vazquez, L. Garner, G. Smith, "Tomographic method for measurement of the gradient refractive index of the crystalline lens. I. The spherical fish lens," J. Opt. Soc. Am. A **22**, 3, 424-433 (2005).

[28] D. Vazquez, E. Acosta, G. Smith, L. Garner, "Tomographic method for measurement of thegradient refractive index of the crystalline lens. II. The rotationally symmetrical lens," J. Opt. Soc. Am. A **23**, 10, 2551-2565 (2006).

[29] Schmitt, J.M. *Optical coherence tomography (OCT): a review,* IEEE Journ. Sel. Top. in Quant. El., 1999; 5, 4: 1205-1215.

[30] Verma, Y., Rao, K. D., Suresh, M. K., Patel, H. S., Gupta, P. K., *Measurement of gradient refractive index profile of crystalline lens of fisheye in vivo using optical coherence tomography.* Appl. Phys. B., 2007; 87: 607–610.

[31] A. de Castro, S. Ortiz, E. Gambra, D. Siedlecki, S. Marcos, "Three-dimensional reconstruction of the crystalline lens gradient index distribution from OCT imaging," Opt. Express **18**, 21, 21905-21917 (2010).

[32] Jagger, W. S., "The optics of the spherical fish lens," Vis. Res. **32**, 7, 1271-1284 (1992).

[33] B. A. Moffat, D. A. Atchison, J. M. Pope, "Age-related changes in refractive index distribution and power of the human lens as measured by magnetic resonance micro-imaging in vitro," Vis. Res. **42**, 1683–1693 (2002).

[34] C. E. Jones, J. M. Pope "Measuring optical properties of an eye lens using magnetic resonance imaging," Magn. Reson. Imaging **22**, 211–220 (2004).

[35] C.E. Jones, D.A. Atchison, R. Meder, J.M. Pope, "Refractive index distribution and optical properties of the isolated human lens measured using magnetic resonance imaging (MRI)," Vision Res **45,** 2352–2366 (2005).

[36] H. von Helmholtz, *Treatise on Physiological Optics,* 3rd ed.,translated by J. P. C. Southall, Optical Society of America, New York (1924).

[37] H. H. Emsley, *Visual Optics,* 5th ed.*,* New York, Butterworths, (1952).

[38] Y. Le Grand, S. G. El Hage, S.G., *Physiological Optics*, New York, Springer-Verlag, (1980).

[39] L. N. Thibos, M. Ye, X. Zhang, A. Bradley, "Spherical Aberration of the Reduced Schematic Eye with Elliptical Refracting Surface," Opt. Vis. Sci. **74**, 7, 548-556 (1997).

[40] S. Nakao, T. Ono, R. Nagata, I. Iwata, "The distribution of refractive indices in the human crystalline lens," Jap. J. Clin. Opthal. **23**, 41-44 (1969).

[41] A. Hughes, "The artifact of retinoscopy in the rat and rabbit eye has its origin at the retina/vitreous interface rather than in longitudinal chromatic aberration," Vision Res. **19**,1293-1294 (1979).

[42] O. Pomerantzeff, H. Fish J. Govignon C. L. Schepens "Wide-angle optical model of the eye," Opt. Acta **19**, 387–388 (1972).

[43] O. Pomerantzeff, M. Pankratov, G. J. Wang, P. Dufault, "Wide-angle optical model of the eye," Am. J. Optom. Physiol. Opt. **61**, 166-176 (1984).

[44] W. S. Jagger, "The Refractive Structure and Optical Properties of the Isolated Crystalline Lens of the Cat," Vis. Res. **5**, 723-738 (1990).

[45] G. Smith, B. K. Pierscionek, D. A. Atchison, "The optical modeling of the human lens," Opthal. Phys. Opt. **11**, 359-369 (1991).

[46] I. H. Al-Ahdali, M. A. El-Messiery, "Examination of the effect of the fibrous structure of a lens on the optical characteristics of the human eye: a computer-simulated model," Appl. Opt. **34**, 25, 5738-5745 (1995).

[47] H. L. Liou, N. A. Brennan, "Anatomically accurate, finite model eye for optical modeling," J. Opt. Soc. Am. A. **14**, 1684-1695 (1997).

[48] R. Navarro, F. Palos, L. González, "Adaptive model of the gradient index of the human lens. I. formulation and model of aging ex vivo lenses," J. Opt. Soc. Am. A, 24, 8, 2175-2185 (2007).

[49] B. K. Pierscionek, R. C. Augusteyn, "Growth related changes to functional parameters in the bovine lens," Biochim. Biophys. Acta 283-290 (1992).

[50] A. S. Vilupuru, A. Glasser, "Optical and biometric relationships of the isolated pig crystalline lens," Ophthal. Physiol. Opt. **21**, 4, 296-311 (2001).

[51] A. Glasser, M. C. W. Campbell, "Biometric, optical and physical changes in the isolated human crystalline lens with age in relation to presbyopia," Vision Res. **39**, 1991–2015 (1999).

[52] F. Manns, V. Fernandeza, S. Zippera, S. Sandadia, M. Hamaouia, A. Hoc, J. M. Parela, "Radius of curvature and asphericity of the anterior and posterior surface of human cadaver crystalline lenses," Exp. Eye Res. **78**, 39–51 (2004).

3. Lens Model Construction Methodology

The last chapter outlined the need for a customizable crystalline lens model both for the scientific investigation of its properties and for its use in ophthalmic applications such as customized refractive eye surgery. This chapter will describe the formulation of the mathematical model of the lens developed in this thesis. Also discussed are the techniques used in measuring the optical and biometric properties of real crystalline lenses to be applied to the model. The verification of the measurement systems will also be discussed.

3.1 Custom Crystalline Lens Model Mathematical Description

3.1.1 Crystalline Lens Model Surface Shapes

The surfaces of the crystalline lens were described as aspheric surfaces. This was to accurately replicate the surfaces of actual crystalline lenses, as per the many studies described in the previous chapter. Mathematically, each surface of the lens was described by the sagittal depth equation for a rotationally symmetric conic section:

$$z = \frac{(x^2 + y^2)c}{1 + \sqrt{(x^2 + y^2)c^2(1 + q)}} \tag{3.1}$$

where the surface apical radius of curvature is given by $R = 1/c$. The sagittal height is in the z axis, perpendicular to the x-y plane. The coefficient q is the asphericity (q = 0 for a sphere, q = -1 for a parabola, -1 < q < 0 for a prolate ellipse, and q > 0 for an oblate ellipse). Since the human crystalline lens, like most mammalians lenses, has different apical curvatures and asphericities for the anterior and posterior surfaces, two different sets of parameters were allowed to properly describe the two surfaces of the lens. Therefore the model had four unknown parameters in the description of the surface of an individual lens; the anterior and posterior surface radii and asphericities: R_a, R_p, q_a, and q_p.

3.1.2 Crystalline Lens Model GRIN

The crystalline lens GRIN in this thesis was developed using the hypothesis already described by other authors and that an estimation of the lens GRIN across the entire lens can be calculated from the measured GRIN in the equatorial plane, as discussed in Chapter 2. It is known that the distribution in this plane is rotationally symmetric and can be calculated from laser beam scanning. This method has been used by other authors (Campbell (1984)[1] and Chan (1988)[2]) and is described in detail later in this chapter. In the equatorial plane, the GRIN as a function of the radial distance from the lens centre has the generally accepted following form:

$$n(R) = n_c \sqrt{1 - \left(\frac{n_c^2 - n_s^2}{n_c^2}\right) f(R)} \tag{3.2}$$

$$f(R) = C_0 + C_1 R^2 + C_2 R^4 \tag{3.3}$$

$$R = r/b \ , \tag{3.4}$$

where $\boldsymbol{r}$ is the distance from the lens center, b is the equatorial lens radius, n_c and n_s are the central and surface index of refraction, respectively. C_0, C_1 and C_2 are parameters found by fitting equation () to the experimental data from laser beam scanning. The GRIN at any point in the lens was then determined from the equatorial GRIN using the following set of equations:

$$n(r,z) = n_c \sqrt{1 - \left(\frac{n_c^2 - n_s^2}{n_c^2}\right) p(r,z)} \tag{3.5}$$

$$p(r,z) = C_0 + C_1 K(r,z)^2 + C_2 K(r,z)^4 \tag{3.6}$$

$$K(r,z) = \sqrt{\left(\frac{r}{b}\right)^2 + \left(\frac{z}{\left[1-\sqrt{k(r,z)}\right]^W (b-a)+a}\right)^2} \tag{3.7}$$

$$k(r,z) = \left(\frac{r}{b}\right)^2 + \left(\frac{z}{a}\right)^2 \tag{3.8}$$

where W is the GRIN fit index parameter, a and b are the lens radius along the z axis and in the equatorial plane respectively, and $r = \sqrt{x^2 + y^2}$ is the distance along the equator from the lens centre. The anterior and posterior sections of the lens were described independently; for example when the anterior of the lens GRIN was described by equations (3.7) and (3.8), a represented the anterior lens thickness. Equation 3.7 is a modification of the equation which describes an elliptically symmetric GRIN:

$$K(r,z) = \sqrt{\left(\frac{r}{b}\right)^2 + \left(\frac{z}{a}\right)^2} \tag{3.9}$$

which has been shown to be incorrect in describing the lens in the equatorial plane as it fails to model lenses since it does not predict ray tracing results in all planes, as discussed in Chapter 2. The modifier term, $\left[1-\sqrt{k}(r,z)\right]^W (b-a)$ acts as a modifier for the scaling of the z axis to accommodate for a change in symmetry from elliptical at the lens surface to spherical at the lens center. For example, along the optical axis ($r = 0$) at the anterior lens surface $z = a$ and thus $k(r,z) = 1$, the modifier term becomes equal to zero for any value of W and the GRIN is elliptical in shape. At the lens equatorial plane, $z = 0$ and thus $k(r,z) = 0$, the modifier term is equal to 1 for all values of W and the GRIN is spherical. For all values of z in between, the ellipticity changes as a function of z according to the value of W. A schematic of the lens in the sagittal plane and equatorial plane described by these equations is shown in Figure 3.1.

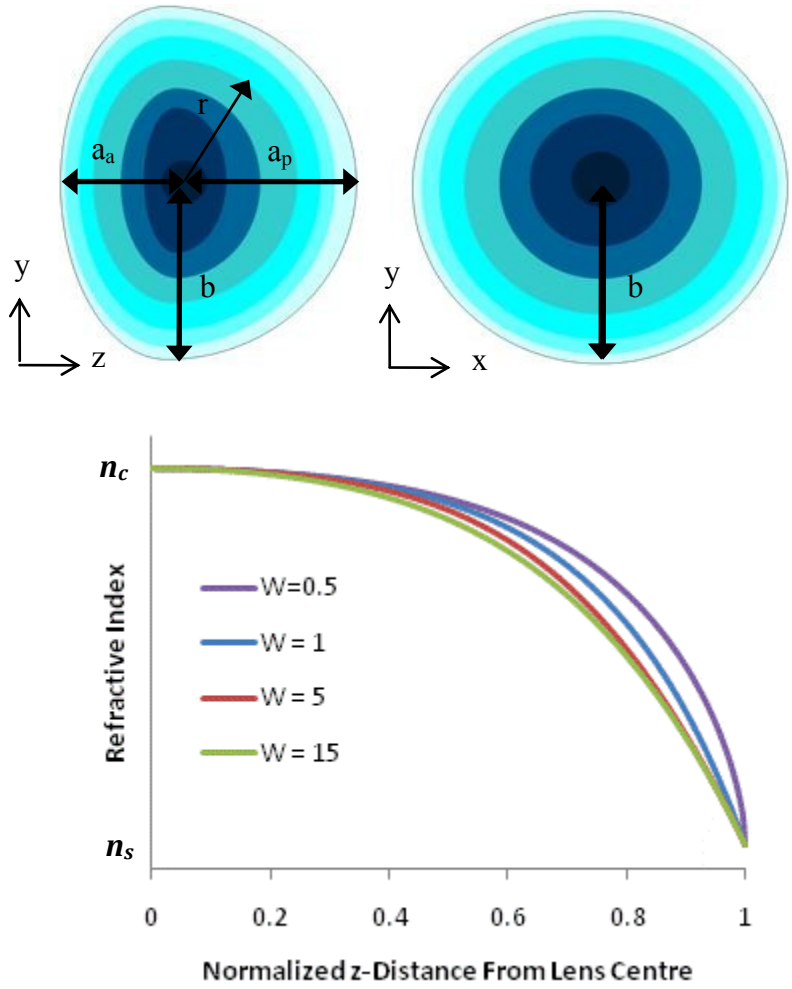

Figure 3.1: Schematic of the crystalline lens model in the sagittal plane (top left) and equatorial plane (top right). The outer lens surfaces do not necessarily follow the isoindicial contours of the refractive index GRIN profile. (bottom) Refractive index profile in the meridional plane for varying GRIN fit parameter W with normalized distance z from the lens centre.

The lens model is thus dependent upon the anterior and posterior lens thickness and asphericity, anterior and posterior surface curvatures, diameter, and GRIN equatorial parameters, C_0, C_1, and C_2. The remaining parameter, W, is designed to be left as a customization parameter to match an individual lens' model to its measured optical quality. Measurements were performed on the lenses of various species to determine if some correlations between these parameters (with the exception of W) could be used to simplify the model so it could be used in a clinical setting. This was accomplished by entering in all of the measured parameters into Zemax® (Zemax Development Corporation) optical modeling software for a specific lens and determining the value of

W that matched the measured optical performance of that lens, specifically the spherical aberration and focal length.

The model also depends on the central and surface index of refraction for the lens, which have been published for many of these species including humans. It was not the purpose of this thesis to measure the refractive index of the lenses; instead published values were used.

3.2 Crystalline Lens Measurements and Calculations

To test the model's ability to predict the optical performance of crystalline lenses, the focal length, spherical aberration, equatorial GRIN as well as the anterior and posterior thickness, diameter, and surface shapes were measured (or calculated where necessary) for several crystalline lenses across three mammalian species - pigs, rabbits and cows. The results of these measurements and model testing are presented in the next chapter. In the rest of this chapter the instrumentation used to obtain these measurements including validation of the approaches and testing of the reliability of the measurements is presented.

3.2.1 Lens Focal Length and Aberration Measurement System

A ray tracing system was constructed to measure the monochromatic focal length and aberrations of each crystalline lens. The experimental set-up, shown in Figure 3.2, consisted of a high-powered multi-line Krypton - Argon ion laser (Series 43, Melles Griot) with a filter isolating the 647nm line. A spatial filter was used to produce a clean source beam. The beam was then collimated with a 200mm focal length lens to expand the beam to a 20mm diameter. A mask was used to separate the single large beam into an array of 1mm diameter pencils of collimated light separated by 2mm center to center. A system of two lenses acted as a telescope to increase the sampling density of the mask. This also reduced the beam array size to the desired pupil size matching the effective optical zone of the crystalline lenses. A constant pupil size of 6mm for the pig and rabbit lenses, and 11mm for the cow lenses was chosen for measurements since this used the majority of the optical region of these lenses. The mask was mounted on an x-y stage to

change its position by 0.5mm in the x and/or y directions to further increase the sampling density within the lens aperture. The result was 4 data sets providing ray tracing in steps of 0.5mm in the lens principal plane.

A mirror then directed the array of beams upwards through the lens under test where the collimated pencils were refracted by the lens optics. A 0.5" CCD sensor (Hitachi KP M22AN, with no imaging optics) was then placed in the path of the refracted rays after the test lens in a position where all rays were within the area of the sensor. The CCD sensor capturing the images was mounted on a z translation stage with a digital micrometer so that images of the refracted beam pattern could be obtained at two different locations along the optical axis. The captured images (Figure 3.2) show a pattern of spots, each one corresponding to the point of intersection of the ray with the CCD sensor. The beam positions in each image were determined from the known pixel size and total number of pixels of the sensor and the position of each spot in the image.

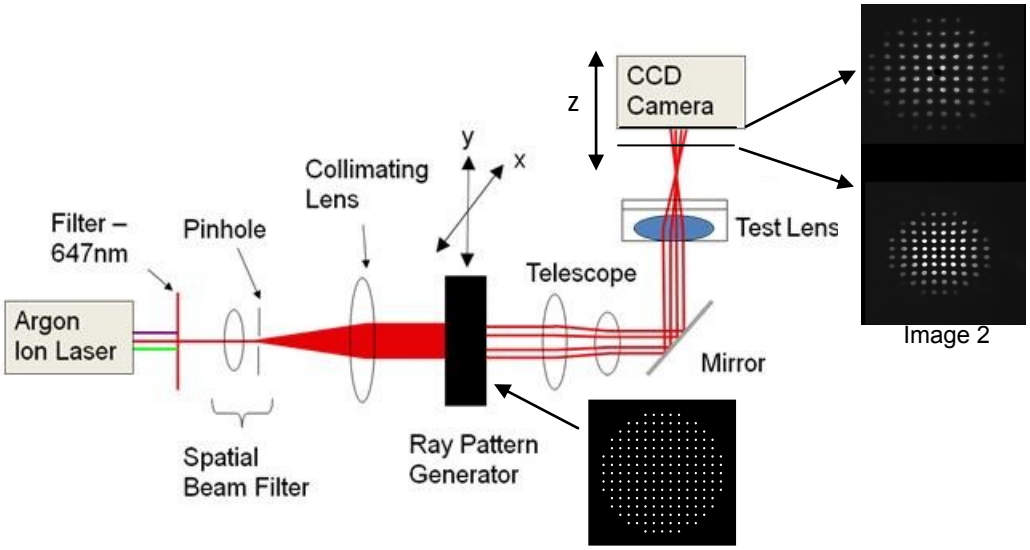

Figure 3.2: Side view schematic of the experimental set up for the ray tracing measurements. An argon ion laser is filtered, collimated, and sent through a mask to form a pattern of beams. The beam pattern is concentrated using two lenses as a telescope then sent through the lens under test. Images of the beam pattern after it has passed through the lens under test are captured using a CCD camera.

The measurement methodology for testing physiological crystalline lenses was as follows: First the crystalline lens, sitting in a balanced saline solution to approximate the aqueous (n = 1.337), was inserted into the measurement system and its optical axis was

aligned with the instruments optical axis. This was achieved by finding the position of the lens for which the central beam passed undeviated through the lens centre. Then eight images were taken at two different planes along the optical axis for four different positions of the mask. Image planes were chosen as far apart as possible along the optical axis while the entire spot pattern remained visible in both positions. Care was taken to ensure the beams did not cross paths in between the images, thus the images were taken on the same side of the (best) focal plane of the lens under test. The original beam grid positions before the beams passed through the lens as well as the images of the beams taken at two different planes after passing through the lens were used to calculate the Zernike polynomials of the wavefront after passing through the lens. These calculations are described in the following section.

3.2.1.1 Aberration and Focal Length Calculations

A custom ray tracing program was written in MathCad© (PTC, Inc.) mathematical modeling software to perform the aberration and focal length calculations. A diagram outlining the ray tracing schematic is shown in Figure 3.3. First an image of the entrance beam pattern of the collimated ray pencils (taken with no test lens in place) was used to locate the position of the beams incident on the test lens. The depth of solution the test lenses were in was carefully recorded with calipers and the effect of refraction of the rays leaving the fluid was calculated and accounted for in the program. Next the four images for each sensor position were combined to create a single set of spots for each sensor planes. A centroid finding algorithm was used to find the center of each spot and a list of point positions was created for each sensor plane. A slope was then calculated for each ray in the vertical and horizontal directions from the displacement of each spot between planes and the distance between the sampling planes. Once the ray slopes were obtained, ray tracing was used to find the plane of best focus for the lens and the principal plane of the lens. The plane of best focus was defined as the plane producing the smallest image diameter based on a root mean square calculation:

$$D = \sum_i \sqrt{(\Delta x_i)^2 + (\Delta y_i)^2} \tag{3.10}$$

where Δx_i represents the x-distance from point *i* to the optic axis, and Δy_i represents the y-distance from point *i* to the optic axis. The principal plane was roughly identified as the plane where the deviated rays when traced back to the lens intersected the incident ray pattern. It was found that an exact principle plane did not exist for the biological lenses; each of the deviated rays intersected the incident ray pattern in a different location along the z-axis. The rays which did not intersect the incident ray pattern were ignored in the calculation. The focal length was then defined as the distance between the principal plane and the best focus plane. This focal length was then used as the radius of curvature of the perfect wavefront at the principal plane and by definition provided the slopes for the rays of a perfect or ideal lens. The wavefront error of the test lens was then

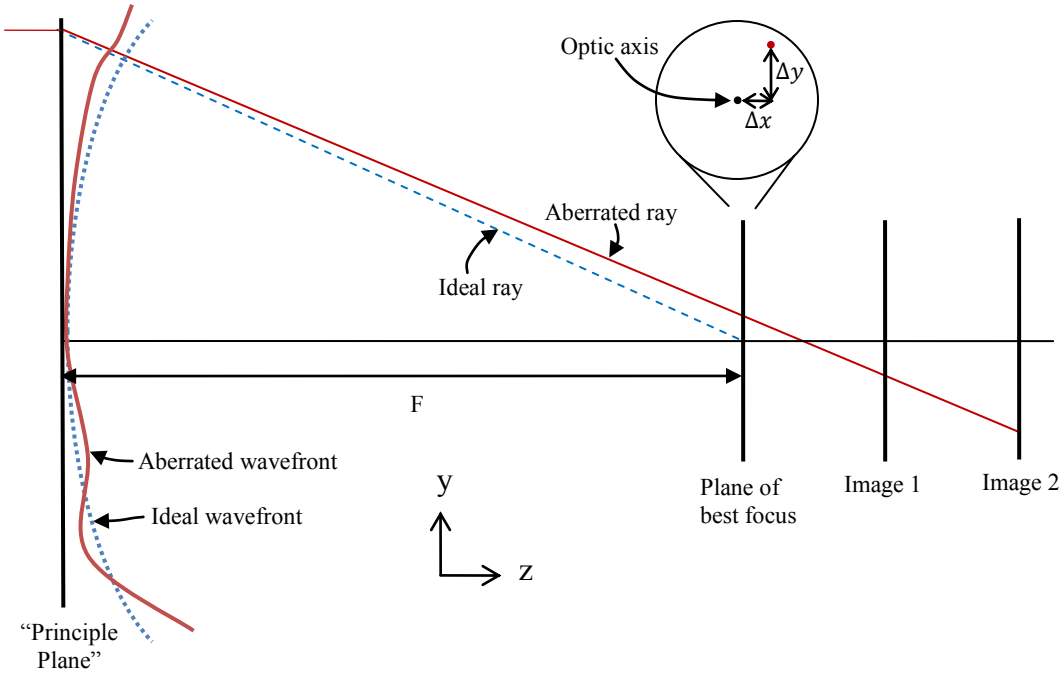

Figure 3.3: Schematic of orientation for ray tracing calculations of focal length and aberrations. One ray traced through the system is shown. Principle plane was not a straight plane as shown.

calculated as a difference in slope between the perfect and actual ray. In this experiment the local slopes of rays across the wavefront were measured at the entrance pupil of the test lens, therefore the method developed by Cubalcini (1979)[3] was used to determine the Zernike coefficients of the aberrations. In this approach the coefficients of the Zernike polynomials could be directly calculated from a least squares fit of the ray slopes with the

derivatives of the Zernike polynomials. Details of this calculation can be found in Appendix B.

3.2.2 Equatorial GRIN Distribution Measurement System

To calculate the equatorial GRIN distribution, a measurement of ray deviations in that plane was required. The same setup as above was used for this measurement with a few modifications, shown in Figure 3.4. First, the mask used for this measurement was limited to a single horizontal set of rays since the equatorial section of the lens lies along the x-y plane at z = 0. Second, the lens was positioned in the same plane as the original beam so the set of rays was incident on the equatorial plane instead of the sagittal plane of the lens. Ray directions were obtained using the methodology described above for the aberration measurement. To ensure the beams were passing through the equatorial plane, it was ensured there was no deviation by the beams out of the x-y plane, if there was any deviation it was caused by the GRIN directly above or below the plane.

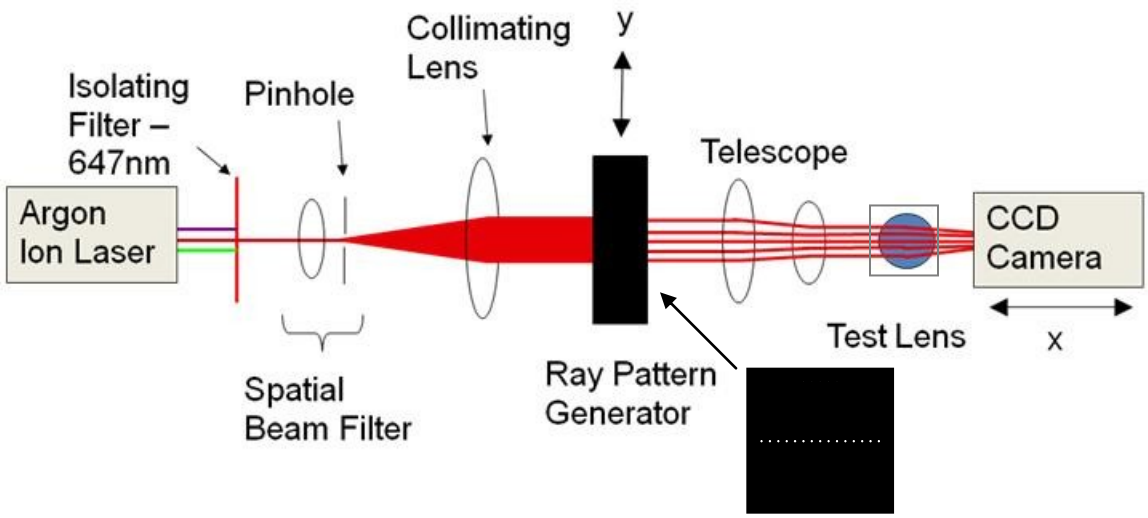

Figure 3.4: Top view of schematic of equatorial GRIN distribution measurement set up. Similar to the wavefront measurement set up; only one line of rays in the y direction is used and directed through the equatorial lens plane.

3.2.2.1 Equatorial GRIN Calculations

The GRIN in the equatorial plane of the lens was calculated using the methods developed by Campbell (1984)[1] and Chan (1988)[2] who both used a modified version of

Chu (1977)[4], who produced a method to non-destructively determine the GRIN of optical fibre performs that have rotational symmetry. This method is well documented and described in further detail in Appendix A. In summary in this methodology the amount of deviation of each beam as it exits the lens is used to calculate the refractive index profile in the equatorial plane. The basic geometry is shown in Figure 3.5. The beam position upon entering the lens is y, and $\psi(y)$ is the exit angle of the beam relative to the optic axis upon leaving the lens as a function of the beam height upon entering the lens. The refraction of rays leaving the medium was accounted for in the calculations as in the previous section.

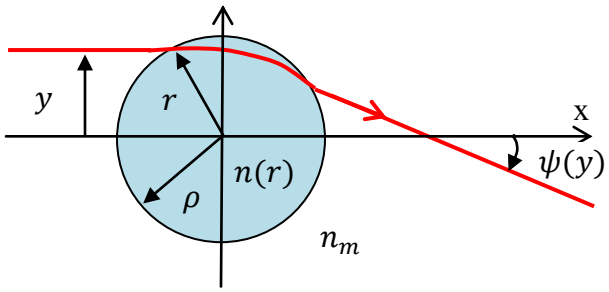

Figure 3.5: Schematic diagram of the rays in the equatorial plane and the measured variables used in the GRIN profile calculation. The actual measurements are performed in the equatorial plane.

In order to find the refractive index distribution as a function of the ray paths passing through the lens, the function $\psi(y)$ is transformed into a new function:

$$g(\xi) = \frac{1}{\pi}\int_{\xi}^{\rho} \frac{dy\,\psi(y)}{\sqrt{y^2-\xi^2}} \tag{3.11}$$

where ξ is a dimensionless variable. Once $g(\xi)$ was found, the refractive index profile was calculated using:

$$r = \xi e^{-g(\xi)} \tag{3.12}$$

$$n(r) = n(\rho)e^{g(\xi)} \tag{3.13}$$

where r is the radial distance from the lens centre, and ρ is the lens diameter. In the case of this experiment, the refractive index was not matched between the edge of the lens and the surrounding medium, and therefore this difference in index must be accounted for. In order to remove the effects of this mismatch and still be able to use (3.11) for analysis, the ray entrance height and angle measured experimentally were transformed into equivalent index matched data. This was done by using the transforms:

$$\bar{y} = y/\bar{n} \tag{3.14}$$

$$\bar{\psi}(\bar{y}) = \psi(y) - 2[\sin^{-1}(y/\rho) - \sin^{-1}(y/\bar{n}\rho)] \tag{3.15}$$

Where $\bar{n}$ is the ratio of the refractive index at the edge of the lens and the surrounding medium. The data set $[\bar{\psi}(\bar{y}), \bar{y}]$ represented the entrance ray heights and associated exit ray angles relative to the optical axis of a set of fictitious rays passing through a lens with an index matched surrounding. Equation (3.11) was calculated by first interpolating between the points of $[\bar{\psi}(\bar{y})]$ using a cubic spline interpolation. Once the coefficients of the spline were calculated, then the integral was evaluated to produce a data set $g(\xi)$. This data set was used in (3.12) and (3.13) to find the points $n(r)$ and r. Once these points were determined, a least squares fit was performed to determine the parabolic shape of the refractive index profile and the corresponding coefficients C_0, C_1, and C_2, for use in equation (3.5). A typical illustrative result of this measurement for one pig lens is shown in Figure 3.6.

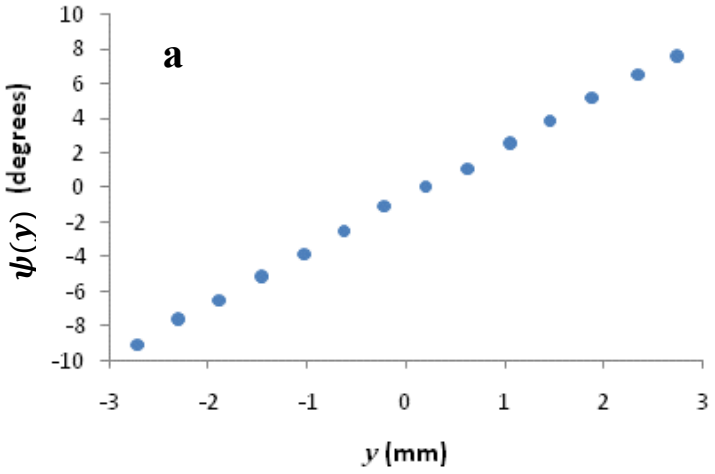

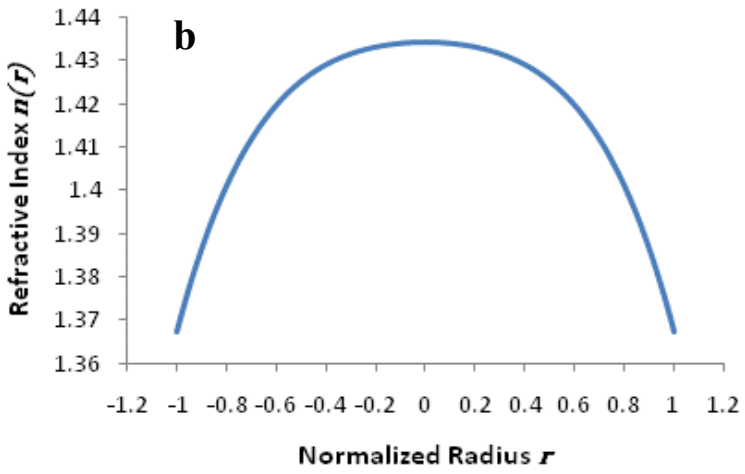

Figure 3.6: (a) Angle formed by the emerging ray $\psi(y)$ vs. displacement of the incident ray from the optic axis y in mm measured in the equatorial plane of one pig lens. (b) Refractive index distribution $n(r)$ vs. normalized lens radius r in the equatorial plane calculated from the points measured in (a).

3.2.3 Profile Measurement System

To measure the thickness, diameter, radius of curvature, and asphericity of the crystalline lenses, a profile measurement system was constructed, shown in Figure 3.7. This system consisted of a diffuse white light source place several centimetres behind the lens, to backlight the lens under test and a CCD camera equipped with an imaging lens to capture the profile image of the test lens. One image was required for the thickness and diameter measurements; two more images were required for the radius of curvature and asphericity measurements. The backlight was covered slightly to increase the contrast between the surface of the lens and the image background to improve the imaging software's edge detection for the surface profile measurement. As the top surface of the lens was seen clearly using this configuration, the lens was measured once with one surface on top and then again after the lens was turned over to bring the second surface to the top. The lenses were very lightly touching the bottom of the lens holder and deformation due to gravity was not a factor since they were mostly floating in solution.

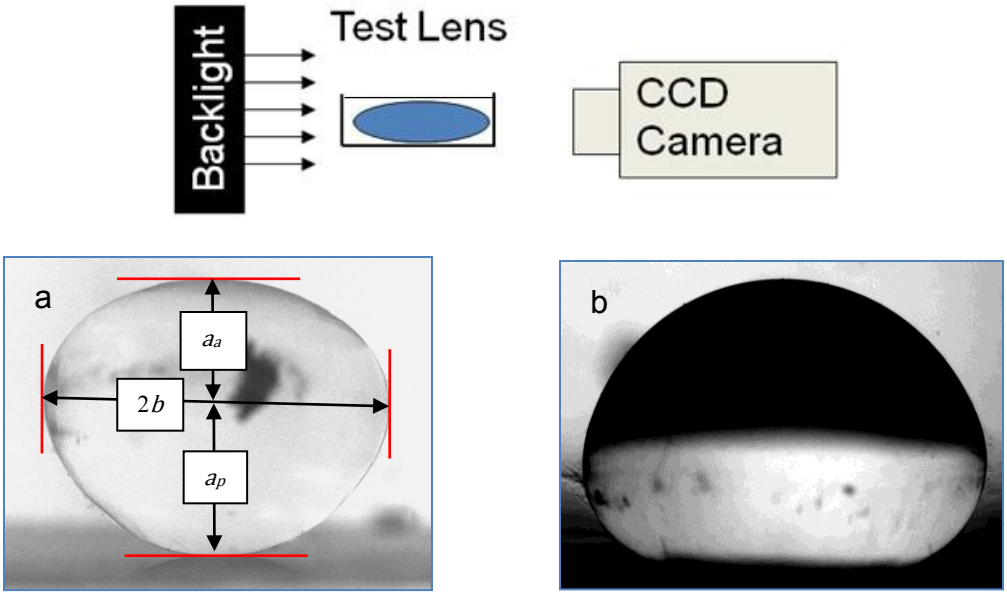

Figure 3.7: Profile Measurement system. This measurement system consisted simply of a diffuse backlight and CCD camera with an imaging lens to capture the profile of the lens under test. Image (a) was taken to measure the lens thickness and diameter, and (b) was taken to measure the radius of curvature and asphericity; images for the lens anterior and posterior were required.

3.2.3.1 Biometry Calculations

A custom program was written in MathCad© to extract the lens diameter and thickness as well as the surface curvature and asphericity. First a calibration factor was determined by measuring a target of known dimensions to quantify the magnification of the imaging system. To measure the lens diameter and thickness, the lens was divided in two section separated by the equatorial plane, as seen in Figure 3.7 (a). The front and back thickness were measured as the distance from this plane to the apex of the anterior and posterior lens surfaces, respectively. The diameter was simply measured as the length of the widest chord in the equatorial plane. These measurements were simply determined directly from images as shown in Figure 3.7 (a) by measuring the length in pixels and applying a calibration factor.

An edge finding routine was used (included in Mathcad's image processing software) to find a binarized image of the edges of the lenses. The conic section parameters, R and q, were found by performing a least squares fit of the binarized data of the lens surface. As a quality assurance test, a spherical surface shape was also fitted to

each profile and an F test[5] was performed on each fit to determine if the asphericity coefficient resulted in a statistically significant ($P > 0.05$) improvement to the fit; if it did not the asphericity coefficient was set to 0.

3.2.4 Measurement System and Calculation Validation

The wavefront measurement system and calculation program was verified by performing focal length and aberration measurements using the measurement system and program on a known glass catalogue lens and then calculating the same using Zemax© optical modeling software. An 18mm focal length, 9mm diameter double convex glass lens was chosen as the test lens (Edmund Optics Inc., Lens #DCX32969). This lens was chosen in particular since it was a double convex lens with spherical surfaces having approximately the same diameter and focal length as a human crystalline lens, with measurable spherical aberration. This test lens was loaded into the system and images were recorded as described above, and shown in Figure 3.8. Images were also taken with no lens in the system and the wavefront calculations were performed on these images to ensure the beam was collimated, untilted, and there were no aberrations introduced by the system itself.

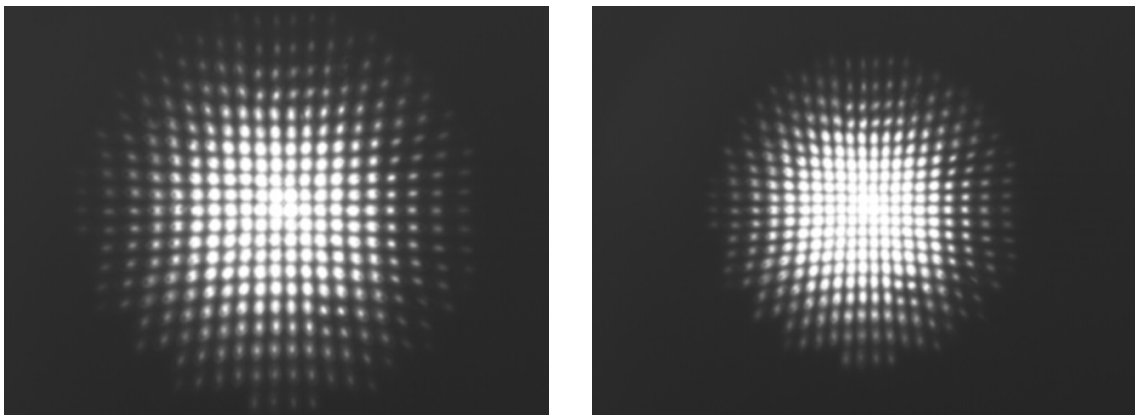

Figure 3.8: Wavefront system calibration. Shown are sample raw images of the beam pattern after passing through a catalogue glass lens, images of four different ray generator locations have been overlapped to show the beam density. Two images were taken at different locations on the optical axis for measurement of the lens focal length and optical aberrations.

In order to determine the repeatability, accuracy, and precision of the wavefront system, measurements were repeated on the same lens 10 times by performing 10

repeated measurements after removing the lens from the system and re-measuring each time. The calculated focal length and spherical aberration were compared with the Zemax output for the same lens. Other aberrations calculated were very small, on the order of 10^{-4}μm as would be expected for a well aligned glass lens with rotational symmetry. Lens alignment was difficult so there were some unavoidable tilts in the wavefront measurements. The focal length and spherical aberration of the lens calculated using Zemax was within one standard deviation of the 10 measurements of focal length and spherical aberration using the measurement system.

The asphericity, curvature, and thickness measurement system was verified by using the same test lens using the profiling measurement system. The asphericities of both lens surfaces were measured to be spherical, with F test comparisons ($P < 0.05$) to aspheres performed for both surfaces on all measurements. Again, very good agreement was achieved as the actual published curvature and thickness measurements were within one standard deviation of 10 measurements.

Verification for the equatorial measurement system was not possible since a known GRIN lens having a similar shape and index distribution to a biological crystalline lens was not available for testing. Therefore the repeatability in this measurement was taken as the repeatability measure for the same crystalline lens measured 10 times, with the lens removed from the system and re-measured each time. This measurement is explained in the next section. A summary of the repeatability measurements is shown in Table 3.1. The measured average with one standard deviation is within the actual Zemax calculated or catalogue provided value for each variable, therefore both measurement systems are valid.

Table 3.1: Summary of repeatability measurements for a catalogue glass lens using the ray tracing measurement system.

Parameter	***Measured Average (± 1σ)***	***Zemax or Catalog (± tol.)***
Spherical Aberration	0.32 ± 0.02μm	0.297 ± 0.002μm
Focal Length	17.9 ± 0.1mm	18.0 ± 0.2mm
Curvature	18.13 ± 0.01mm	18.15mm
Thickness	2.55 ± 0.01mm	2.6 ± 0.1mm
Diameter	8.99 ± 0.01mm	9.0 ± 0.1mm

3.3 Biological Lens Extraction and Measurements

Pig and cow eyes were obtained from a local abattoir. Enucleation was performed within 12 hours of slaughter and whole eyes were received within the next 6 hours. The eyes were transported in a saline solution from the abattoir to the laboratory where the measurements were performed. The age of all pigs and cows measured ranged from approximately 3 months to 1 year. Rabbit eyes were obtained from the University of Ottawa animal care services from animals euthanized for other studies. Enucleations of the rabbit eyes were performed within 6 hours of euthanization, and whole rabbit eyes were transported in a saline solution from animal care services to the laboratory. The age of each rabbit was exactly 6 months. The lens extraction procedure is shown in Figure 3.9. Lenses were extracted from the eyes by first cutting a flap in the cornea large enough to access the lens. The iris was then removed from the lens with a scalpel to expose the ciliary body. The zonules were then carefully cut away from the lens using a scalpel. The lens was then removed from the eye by removing the vitreous attached to the posterior surface using a blunt object. The lenses were then immediately placed in a petri dish already containing a PH balanced saline solution, similar to the environment inside the eye. This solution was isosmotic with the crystalline lenses to prevent swelling or shrinking of the lens during the measurements, as well as to preserve the epithelial cell integrity of the lens capsule. It was apparent during the lens measurements if some vitreous remained on the posterior of the lens, resulting in a distorted ray image, and this problem was remedied by removing the lens from the measurement system and removing the vitreous. Care was taken not to let any sharp instruments come in contact with the lenses during extraction as this would possibly rupture the lens capsule or produce scratches, affecting the clarity of the outer surface of the lens and the optical properties of the lens. The lenses were measured immediately after extraction. Since the lenses were removed from the eye they were studied in the fully accommodated state.

Lenses were placed in the petri dishes with the anterior surface facing down such that the collimated beam entered this surface first. The bottoms of the petri dishes were equipped with very thin glass cover slips (0.13mm) to minimize the effect of the dish on the measurements. Measurements were performed in the system with these petri dishes filled with saline with no lens in place to ensure aberrations were not produced from

either the dishes or the saline forming a meniscus inside the dishes. The depth of the saline in the petri dish was constant for all lenses and was accounted for during modeling. Sample raw wavefront measurement images are shown in Figure 3.10.

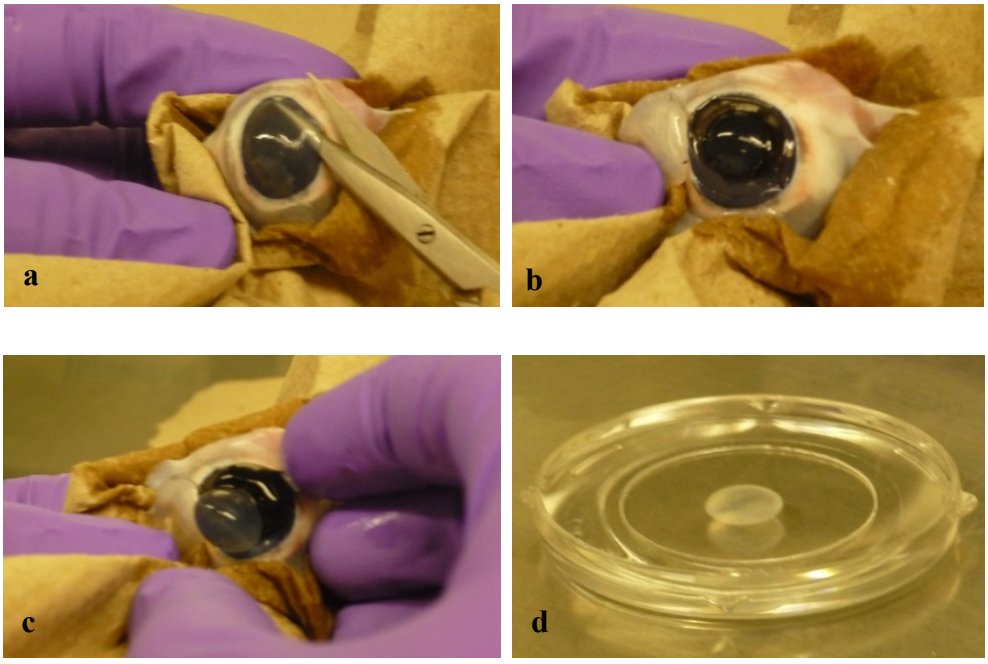

Figure 3.9: Removal of the crystalline lens from pig eyes. The cornea is first cut and pulled back (a) to expose the iris and lens (b). The iris is removed and the zonules are cut from the lens (c). Immediately after the lens is removed it is placed in a saline solution in a petri dish equipped with a very thin glass bottom (d).

Initial alignment of the porcine crystalline lenses proved to be a challenge due to their physiological structure. Light passing through the exact centre of the lens where the sutures meet was highly distorted (seen in Figure 3.10) making it difficult to determine whether the centre spot of the beam pattern was passing through the centre of the lens. Tilt was also difficult to control since the lenses were in a saline solution and would not always lay flat on the bottom of the petri dish such that the optic axis of the lens was in line with the optic axis of the measurement system. These small tilts and decentrations would theoretically produce non-rotationally symmetric aberrations.

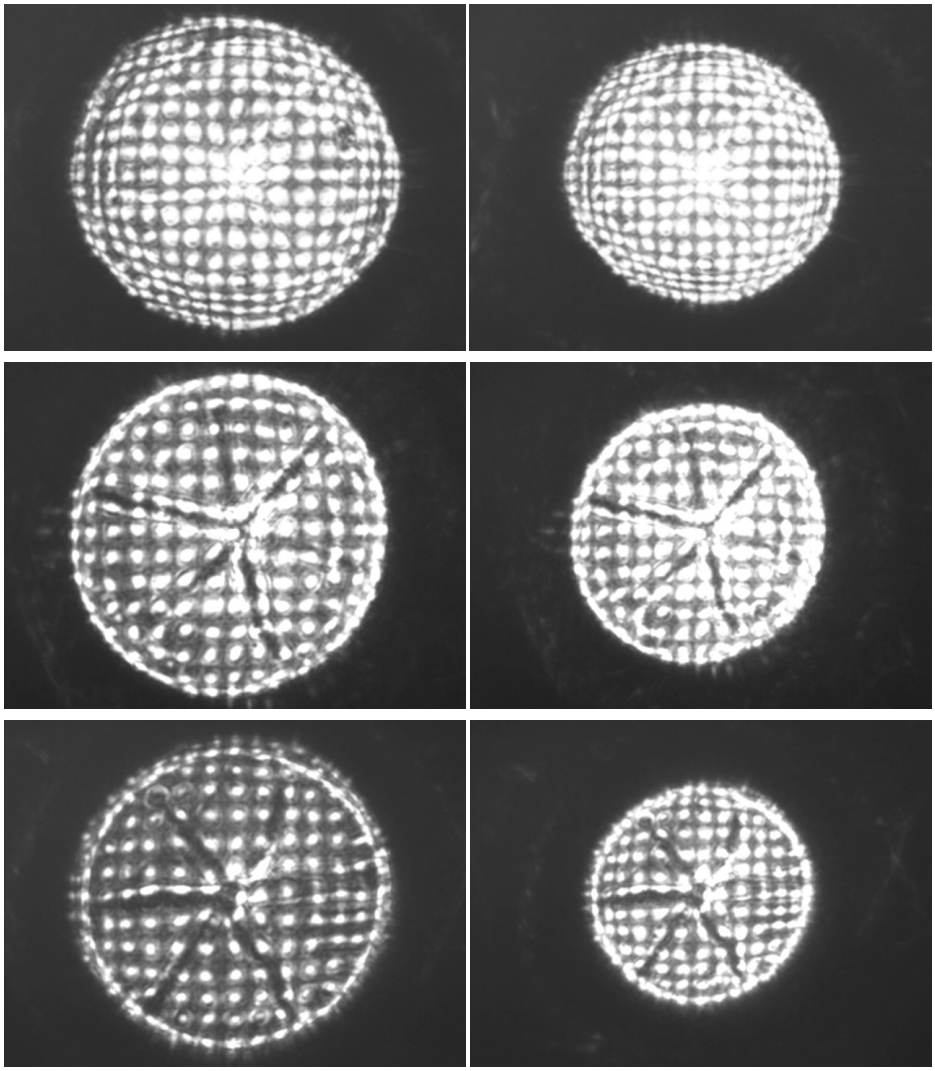

Figure 3.10: Sample images of the spot pattern after passing through three different excised pig lenses farther from (left column) and closer to (right column) the lens' focal plane along the lens' optic axis. Some lenses' images showed strong suture lines (bottom) while others did not (top).

3.3.1 Measurement Errors and Repeatability Analysis of Biological Lenses

Repeatability analysis of the measurement variance for biological samples was performed on the pig lenses by performing repeated measurements of the biometric and optical properties of 10 pig lenses, by removing the lens from the system each time and repeating the measurement. This was done to determine the repeatability of biological samples, even though repeatability measurements were already performed on the catalogue glass lens. Measurements of the lens radii of curvature, asphericity, thickness, and diameter were performed 10 times for each lens. The focal length, spherical

aberration, and equatorial refractive index coefficients were measured only 5 times for each lens because of the rapid degradation of the lens capsule and loss of signal due to scatter. If the lenses were in a better solution more closely matching the aqueous this would not have occurred; this type of solution was not used in these measurements. 5 repeated measurements, however, sufficed for this measurement variance experiment. A summary of this analysis is shown in Table 3.2.

Most of these measurement errors are in good agreement to those achieved by other authors' reported repeatability measurement variations. Those reporting variance in measurement of the spherical aberration of crystalline lenses in their experimental wavefront measurement systems include Liang (1997)[6], Porter (2001)[7], Cheng (2004)[8], Sheehan (2007)[9], and Acosta (2009)[10]. These authors reported measurement variance in spherical aberration ranging from 0.04 to 0.11μm; the measurement variance reported here is the lower end of that range, 0.05. Variations in focal length measurements for similar ray tracing techniques as used here were reported by many authors, including Sivak (1983, 1992)[11,12], Stuart (1991)[13], Moffat (2002)[14], Kuszak (2002)[15], and Borja (2008)[16]. The error range reported by these authors was 0.18 to 1.2mm; the measurement variation in the focal length measured using the system in this thesis, 0.5mm; within range of other's reported errors. Sivak (1983)[11] reported a 0.29mm measurement variation on the surface radius of curvature using a similar profiling technique to that used here. The repeatability of the radii of curvature measured here is well below that: 0.06 and 0.05mm for the anterior and posterior surfaces, respectively. No authors using similar techniques to measure the asphericity reported repeatability variations. The remaining biometrical repeatability variations are also within other authors' ranges; however it is easier to compare these measurements to the resolution of the system itself since they are computed in terms of direct CCD image measurement. The calibration of the profiling system gives 0.0075mm/pixel. Therefore the measurement variations of 0.01 to 0.02mm for the total thickness and diameter measurements correspond to approximately 2-3 pixels of measurement variation. This method was also applied to determine the validity of the repeatability measurement of the radii of curvature and asphericity. An increase in the height and width of the image profiles by 3 pixels caused

an increase in the radii of curvature by approximately 0.06mm, and an increase in the anterior asphericity of 0.02.

Table 3.2: Repeatability for all measured parameters of ten pig lenses, 10 measurements repeated for all biometric measurements, 5 measurements repeated for optical measurements (f and SA).

Variable	*±1σ*	*% of measurement*
$\mathbf{R_a}$	0.06mm	0.81
$\mathbf{q_a}$	0.03	1.86
$\mathbf{R_p}$	0.05mm	0.99
$\mathbf{q_p}$	0.01mm	1.00
t	0.02mm	0.28
$\mathbf{a_a}$	0.01mm	0.32
$\mathbf{a_p}$	0.01mm	0.25
b	0.01mm	0.22
f	0.5mm	1.92
SA	0.05μm	8.77

3.4 Summary

This chapter outlined the steps taken in this thesis in the construction of a fully customizable anatomically correct crystalline lens model. This new customizable model has aspheric front and back surfaces, and an interior described by a variable GRIN. Many parameters were available for the model to be completely customizable, however too many free parameters would render the crystalline lens impossible to model as there is an infinite number of possibilities that would produce identical optical characteristics. Also, since part of the goal of this lens model is to eventually be part of a larger model of the entire human eye to be used for in-vivo human crystalline lens characterization, many of these parameters are not measurable when the lens is inside the eye. It was therefore necessary to fix as many parameters as possible to enable the lens model to be both usable, yet remain customizable to still retain the uniqueness of each modeled lens.

Three measurement systems were constructed to measure the lenses' aberrations, focal length, thickness, diameter, surface curvature, and asphericity and calculate the GRIN distribution in the equatorial plane. These measurement systems were based on the best performing measurement systems reported by other authors for similar

measurements. The performance of the three measurement systems were verified by testing a known glass lens, and repeatability measurements of real crystalline lenses.

The next chapter will show all biometric and optical results. These were then applied to the model to reduce the number of parameters to form a usable customizable model, and to verify the model itself and show its effectiveness in terms of representing the crystalline lens.

References

[1] M. C. W. Campbell, "Measurement of refractive index in an intact crystalline lens," Vis. Res. **24**, 409-415 (1984).

[2] D. Y. C. Chan, J. P. Ennis, B. K. Pierscionek, G. Smith, "Determination and modeling of the 3-D gradient refractive indices in crystalline lenses," Appl. Opt. **27**, 5, 926-931 (1988).

[3] R. Cubalcini, "Modal wave-front estimation from phase derivative measurements," J. Opt. Soc. Am. **69**, 7, 972-977 (1979).

[4] P. L. Chu "Nondestructive measurement of index profile of an optical-fibre perform," Electron. Lett. **13,** 736-738 (1977).

[5] P. R. Bevington, D. K. Robinson, *Data Reduction and Error Analysis for the Physical Sciences,* 2nd ed. New York, McGraw-Hill (1992).

[6] J. Liang, D. R. Williams, "Aberrations and retinal image quality of the normal human eye," J. Opt. Soc. Am. A **14**, 11, 2873-2883 (1997).

[7] J. Porter, A. Guirao, I. G. Cox, D. R. Williams, "Monochromatic aberrations of the human eye in a large population," Opt. Soc. Am. A **18**, 8, 1793-1803 (2001).

[8] H. Cheng, J. K. Barnett, A. S. Vilupuru, J. D. Marsack, S. Kasthurirangan, R. A. Applegate, "A population study on changes in wave aberrations with accommodation," Journal of Vis. **4**, 272-280 (2004).

[9] M. T. Sheehan, A. V. Goncharov, V. M. O'Dwyer, V. Toal, C. Dainty, "Population study of the variation in monochromatic aberrations of the normal human eye over the central visual field," Opt. Express **15**, 12, 7367-7380 (2007).

[10] E. Acosta, D. Vazquez, L. R. Castillo, "Analysis of the optical properties of crystalline lenses by point-diffraction interferometry," Ophthal. Physiol. Opt. **29**, 235–246 (2009).

[11] J. G. Sivak, R. O. Kreuzer, "Spherical aberration of the crystalline lens," Vis. Res. **23**, 59-70 (1983).

[12] J. G. Sivak, D. D. Stuart, K. L. Herbert, J. A. Van Oostrom, L. Segal, "Optical Properties of the Cultured Bovine Ocular Lens as an In Vitro Alternative to the Draize Eye Toxicity Test: Preliminary Validation for Alcohols," Toxicol. Meth. **2**, 4, 280-294 (1992).

[13] D. D. Stuart, J. G. Sivak, A. P. Cullen, J. A. Weerheim, C. A. Monteith, "UV-B radiation and the optical properties of cultured bovine lenses," Curr. Eye Res. **10**, 2, 177-184 (1991).

[14] B. A. Moffat, D. A. Atchison, J. M. Pope, "Age-related changes in refractive index distribution and power of the human lens as measured by magnetic resonance micro-imaging in vitro," Vis. Res. **42**, 1683–1693 (2002).

[15] J. R. Kuszak, J. G. Sivak, S. A. Moran, S. A., Sheib, W. H. Garner, T. L. Ke, M. R. Hellberg, G. Graff, "Suppression of post-vitrectomy lens changes in the rabbit by novel benzopyranyl esters and amides," Exp. Eye Res. **75**, 459-473 (2002).

[16] D. Borja, F. Manns, A. Ho, N. Ziebarth, A. Rosen, R. Jain, A. Amelinckx, E. Arrieta, R. Augusteyn, J. M. Parel, "Optical Power of the Isolated Human Crystalline Lens," Invest. Ophthal. Vis. Sci. **49**, 6, 2541-2548 (2008).

4. Results and Analysis

This chapter shows the application of the customized crystalline lens model to the measurements of real crystalline lenses. This was done both in order to explore means of simplifying the model and for its justification as a valid model in representing individual crystalline lenses. First, the results of the crystalline lens measurements performed on the measurement systems and calculations using the methods described in the previous chapter are compared with other authors' measurements to validate this data set as a source for testing the model. Following this, the equatorial GRIN distribution was calculated for each species and compared to understand the variation across species. Findings from the equatorial index calculations, as well as all of the other collected measurements were applied to the customizable model to find the GRIN index parameter, W, for each biological crystalline lens measured. The effect of the lens measurement errors and uncertainties were investigated to validate the stability of the model. Finally, relationships between biometric and optical measurements are explored to identify means of further simplifying the model. A simplified model is then proposed and differences between the real lens and predicted performance of the simplified model compared to validate the simple model.

4.1 Crystalline Lens Measurements and Calculations

4.1.1 Biometric and Optical Measurements – Comparison with others

Biometry, focal length, and spherical aberration measurements were performed on 22 porcine, 7 rabbit, and 6 cow crystalline lenses using the systems presented in the previous chapter. These measurements were compared to published results and are presented in Tables 4.1, 4.2, and 4.3 for pig, rabbit, and cow lenses, respectively.

In general the data presented here is in agreement with published results. A few exceptions were present, most likely due to different ages of the animals used. Only two studies measured the aberration of the crystalline lens: Roorda et. al. (2004)[1], and Acosta et. al. (2010)[2], both for pig lenses. Both of these studies used a 7mm pupil size; larger than that used here which was 6mm so a direct comparison is difficult because of the shape of the SA wavefront and its interaction with defocus changes with pupil size. This

could explain why the negative spherical aberration measured by Roorda et. al. (2004)[1] was 0.2μm greater, and the largest SA measured by Acosta et. al. (2010)[2] was almost 1.4μm greater than the largest SA measured here since their pupil size was larger. This was tested briefly using the model and it was found that as the pupil size increases the SA increases. Roorda et. al. (2004)[1] used a ray tracing method, comparable to the method used in this study. Acosta et. al. (2010)[2] used a point diffraction interferometry method and comparisons between these two methods have not been published. Furthermore, the exact position of the plane of measurement for the aberrations (principal plane as opposed to lens center for example) can have a significant impact on the SA value reported so direct comparisons are difficult. Other studies measuring spherical aberration did so by measuring the longitudinal spherical aberration (variation in focus along the optical axis). These could not be compared directly to the wavefront Zernike spherical aberration in this thesis since the Seidel term is a combination of the Zernike piston, defocus and spherical terms[3,4] and the amount of each term is unknown in these other studies. Only one author, Vazquez et. al. (2006)[9], measured the asphericities of the anterior and posterior surfaces; all others assumed spherical profiles. It should be kept in mind, however, that SA is individual and unique to each lens specifically and therefore smaller or larger SA values measured by different authors could have resulted in animals of slightly different breed and/or age.

Table 4.1: Summary of optical and biometric measurements of pig lenses in this thesis and measured by other authors.
KEY: R_a: anterior radius of curvature, R_p: posterior radius of curvature, q_a: anterior asphericity, q_p: posterior asphericity, t: thickness, a_a: anterior thickness, a_p: posterior thickness, b: radius, F: focal length, S. A.: spherical aberration.

Author (year)	Variable	Measured Range	Measurement Methods
This Thesis - Wilson (2010) 22 lenses	**R_a**	5.59 – 7.94mm	Biometry • profilometry • profile fit to asphere Optical • 647nm • laser ray tracing
	R_p	-5.11 – -3.93mm	
	q_a	0.00 – 1.70	
	q_p	0.00 – 0.49	
	t	5.90 – 7.61mm	
	a_a	2.54 – 3.37mm	
	a_p	3.31 – 4.24mm	
	b	7.65 – 9.57mm	
	F	20.00 – 27.30	
	SA	-0.64 – 0.38μm	

Sivak (1983)[5] 6 lenses	$\mathbf{R_a}$	7.28 – 7.86mm	Biometry • profilometry • assumed spherical profiles Optical • 632.8nm • laser ray tracing
	$\mathbf{R_p}$	-5.51 – -5.33mm	
	t	7.91 – 8.13mm	
	F	22.14 – 23.20mm	
Vilupuru (2001)[6] 20 lenses	$\mathbf{R_a}$	5.4 – 7.2mm	Biometry • profilometry • assumed spherical profiles Optical • 632.8nm • laser ray tracing
	$\mathbf{R_p}$	-5.2 – -6.9mm	
	t	8.6 – 11.5mm	
	b	9.7 – 13.8mm	
	F	23.5 – 31.8mm	
Jones (2004)[7] 6 lenses	$\mathbf{R_a}$	5.5 – 6.2mm	Biometry • profilometry • assumed spherical profiles • MRI Optical • 543.1nm • laser ray tracing
	$\mathbf{R_p}$	-4.7 – -5.1mm	
	t	7.7 – 7.9mm	
	b	9.3 – 10.1mm	
	F	18.6 – 20.4mm	
Roorda (2004)[1] 1 lens	**SA**	-0.8μm	Optical • 632.8nm • laser ray tracing • 7mm E.P. Ø*
Koopmans (2004)[8] 9 lenses	**t**	6.22 – 6.87mm	Biometry • ultrasound
Vazquez (2006)[9] 1 lens	$\mathbf{q_a}$	0.654	Biometry • profilometry • fit to ellipse
	$\mathbf{q_p}$	0.389	
	t	7.48mm	
	b	9.55mm	
Rielly (2009)[10] 7 lenses	$\mathbf{R_a}$	6.63mm	Biometry • profilometry • assumed spherical profiles
	$\mathbf{R_p}$	5.08mm	
	t	7.86mm	
Acosta (2010)[2] 12 lenses	**t**	6.8 – 7.4mm	Biometry • profilometry Optical • 671nm • Point diffraction interferometry • 5mm E.P. Ø
	b	8.7 – 9.3mm	
	SA	-2.1 – -0.9um	

*E. P. Ø: entrance pupil diameter used in spherical aberration calculation.

Table 4.2: Summary of optical and biometric measurements of rabbit lenses in this thesis and measured by other authors.

Author (year)	Variable	Measured Range	Measurement Methods
This Thesis - Wilson (2010) 7 lenses	$\mathbf{R_a}$	7.21 – 7.57mm	Biometry • profilometry • profile fit to asphere Optical • 647nm • laser ray tracing
	$\mathbf{R_p}$	-5.91 – -5.49mm	
	$\mathbf{q_a}$	0.98 – 1.09	
	$\mathbf{q_p}$	0 – 0.55	
	t	7.60 – 7.89mm	
	$\mathbf{a_a}$	3.54 – 3.68mm	
	$\mathbf{a_p}$	4.06 – 4.28mm	
	b	10.41 – 10.94mm	
	F	20.06 – 21.8mm	
	SA	-1.08 – 0.08μm	
Hughes (1972)[11] 12 lenses	$\mathbf{R_a}$	6.9mm	Biometry • profilometry • assumed spherical profile
	b	7.0 – 8.6mm	
Sivak (1983)[3] 6 lenses	$\mathbf{R_a}$	6.45 – 6.97mm	Biometry • profilometry • assumed spherical profiles Optical • 632.8nm • laser ray tracing
	$\mathbf{R_p}$	5.48 – 5.90mm	
	t	7.62 – 7.82mm	
	F	16.89mm	
Kuszak (2002)[12] 16 rabbits	**F**	20.11 – 21.24mm	Optical • 632.8nm • laser ray tracing • 8.4mm E.P. Ø
Kong (2009)[13] 8 lenses	**t**	6.96 – 7.78mm	Biometry • profilometry
	b	9.55 – 10.16mm	
Kuszak (2000)[14] 16 rabbits	**b**	6.1 – 11.8mm	Biometry • profilometry

Table 4.3: Summary of optical and biometric measurements of cow lenses in this thesis and measured by other authors.

Author (year)	Variable	Measured ± Range	Measurement Methods
This Thesis - Wilson (2010)	$\mathbf{R_a}$	10.66 – 13.38mm	Biometry • profilometry • profile fit to asphere Optical • 647nm • laser ray tracing
	$\mathbf{R_p}$	-11.06 – -9.04mm	
6 lenses	$\mathbf{q_a}$	0.79 – 1.34	
	$\mathbf{q_p}$	0 – 0	
	t	10.95 – 14.72 mm	
	$\mathbf{a_a}$	4.74 – 6.02mm	
	$\mathbf{a_p}$	6.61 – 7.62mm	
	b	14.94 – 17.37mm	
	F	31.00 – 37.70mm	
	SA	-0.55 – 0.05µm	
Sivak (1983)[3]	$\mathbf{R_a}$	12.26 – 13.70mm	Biometry • profilometry • assumed spherical profiles Optical • 632.8nm • laser ray tracing
6 lenses	$\mathbf{R_p}$	8.58 – 9.86mm	
	t	11.96 – 12.20mm	
	F	35.05 – 38.29mm	
Sivak (1990, 92, 97)[15,16,17]	**b**	17.40 – 19.18mm	Biometry • profilometry Optical • 632.8nm • laser ray tracing
3,13,4 lenses	**t**	15.15 – 17.85mm	
(same system)	**F**	40 – 46.5mm	
Stuart (1991)[18] 12 lenses	**F**	35 – 40mm	Optical • 632.8nm • laser ray tracing
Pierscionek (1992)[19]	$\mathbf{R_a}$	8 – 12.5mm	Biometry • profilometry • assumed spherical profile Optical • 632.8nm • laser ray tracing
23 lenses	$\mathbf{R_p}$	10 – 16mm	
	b	7 – 19.2mm	
	F	32 – 50mm	
Kong (2009)[13]	**b**	16.9 – 18.9mm	Biometry • profilometry
5 lenses	**t**	11.7 – 13.4mm	

The pig, rabbit and cow data reported in this thesis are all within range of other authors' measurements and there are no outliers. It was not the purpose of this section to compare these data statistically in any way as there are significant variances across crystalline lenses of the same species depending on several factors such as age, size, and breed. Therefore identical results cannot be expected; all that can be expected and what

was meant to show in this section is that all measurements are within range of other's published measurements.

4.1.2 Equatorial Index GRIN Distribution Measurements and Calculations

In order for the crystalline lens model developed in this thesis to be useful, it was extremely important to reduce as many variables as possible. The first step in this process was to examine the properties of the equatorial index coefficients both within and across species to verify the stability of the equatorial GRIN. The working hypothesis here was that a single set of parameters could be used within a species without affecting the ability to reproduce the optical properties of crystalline lens across individuals. Early work on pig lenses to test this hypothesis was compared to unpublished work by Munger and Campbell (1990)[20] and the profiles appeared to be similar. Based on this work the hypothesis was then extended to include a constant set of parameters across all species.

The equatorial index coefficients, C_0, C_1, and C_2, were calculated from the ray tracing data for 14 pigs, 7 rabbits, and 6 cow crystalline lenses, using the method outlined in section 3.2.2. Each fit to equation 3.2 was tested for quality of fit by χ^2 statistic[21]. All exceeded the requirement for a 95% confidence to the fit (P-values ranged from 0.107 to 0.672 for all data). It was then possible to continue testing of the working hypothesis for the equatorial GRIN.

The first test was to determine if each coefficient was significantly different between lenses of the same species. Since 5 independent repeated equatorial ray tracing measurements were done on 6 pig lenses, it was possible to establish an experimental variance for each of the coefficients calculated from these measurements which could then be compared across the set of 6 lenses to determine if they were significantly different between pig lenses. A repeated measures analysis of variance (RMANOVA) was performed on these repeated measurements of 6 lenses with a P value of > 0.05 chosen to represent a statistically significant difference between lenses[21]. The results of this analysis showed that the coefficients were not significantly different between individual lenses (P = 0.542 for C_0, P = 0.256 for C_1, and P = 0.397 for C_2). This suggested that the group mean of each coefficient can be used as the value for this species and the repeated measure variance as the parameter variance. The 5 measurements of

each coefficient for the 6 pigs as well as 9 single measurements from the rest of the lenses (39 sets of data from 9 lenses) were averaged together. These are shown in Table 4.4. It was decided not to repeat the within species test for cow or rabbit lenses based on the findings discussed below.

Table 4.4: Equatorial refractive index distribution coefficients determined from the repeatability measurements of 6 pig lenses.

Coefficient	Measured Average (± 1σ)
C_0	0.008 ± 0.007
C_1	0.41 ± 0.02
C_2	0.59 ± 0.04

The next step was to compare the coefficients of the three species to determine if they were statistically significantly different across species; these values are shown in Figure 4.1. A one-way ANOVA test was performed for each coefficient across the three species using group means and standard deviations. No statistically significant differences were found between lenses across the three different species (P = 0.519 for C_0, P = 0.687 for C_1, and P = 0.169 for C_2). These findings suggest that a single equatorial profile based on the mean of measurements is sufficient to represent each lens regardless of species which greatly reduces the complexity of the model.

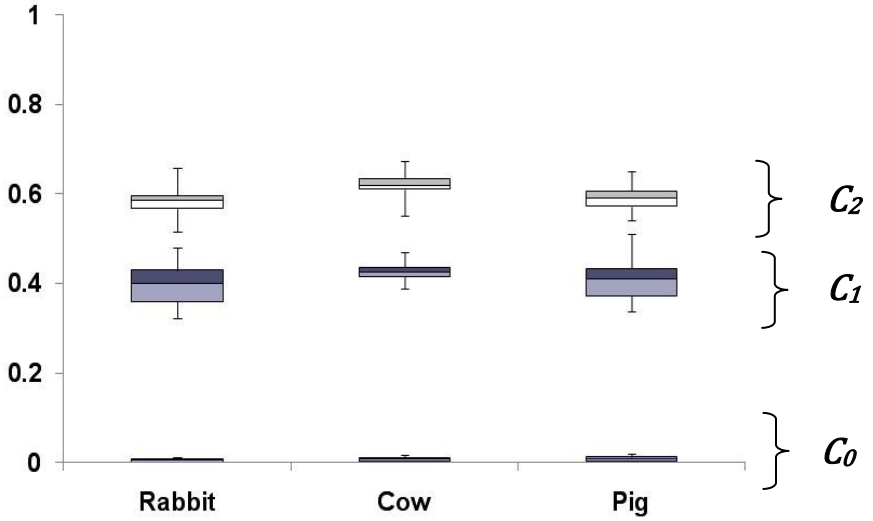

Figure 4.1: Measured equatorial refractive index distribution coefficients C_0, C_1, and C_2, for rabbit, cow, and pig lenses. The bottom error bar indicates the 5th percentile, the bottom of the box indicates the 25th percentile, the middle of the box indicates the mean, the top of the box indicates the 75th percentile, and the top error bar indicates the 95th percentile of all measurements.

It was also desirable to determine if C_0 was significantly different from zero, to determine if this variable could be eliminated from the model altogether for further

simplification. Upon examination of the plots of C_0 in Figure 4.1, and the actual calculated values, there were no occurrences of C_0 below zero; therefore it was clear that C_0 is significantly different from zero and cannot be eliminated based on observation. The results of these calculations of the equatorial index coefficients show that the same equatorial refractive index distribution coefficients can be used across species. Therefore all calculations using the model developed in this thesis used the average values for all measurements for each coefficient, shown in Table 4.5.

Table 4.5: Equatorial refractive index distribution coefficients determined from the measurements across all lenses.

Coefficient	Measured Average (± 1σ)
C_0	0.010 ± 0.006
C_1	0.41 ± 0.03
C_2	0.60 ± 0.06

4.1.3 Determination of the Uniqueness of Lens Biometry and Optical Properties

The remaining variables in the model are the anterior and posterior radius of curvature and asphericity, anterior and posterior thickness, equatorial diameter, focal length, and spherical aberration. From the 5 repeated measured on 6 pig lens it was established that the differences in the parameters across the 6 lenses were statistically significant larger than the resolution of their measurements by performing a repeated measures ANOVA (P-values ranged from 0.001 to 0.007 for all data). An example of the variability is shown in Figure 4.2 for 5 measurements of 6 pig lenses for the anterior radius of curvature, diameter, and focal length. It can be concluded from the RMANOVA that these variables must be uniquely determined for each individual lens in the model.

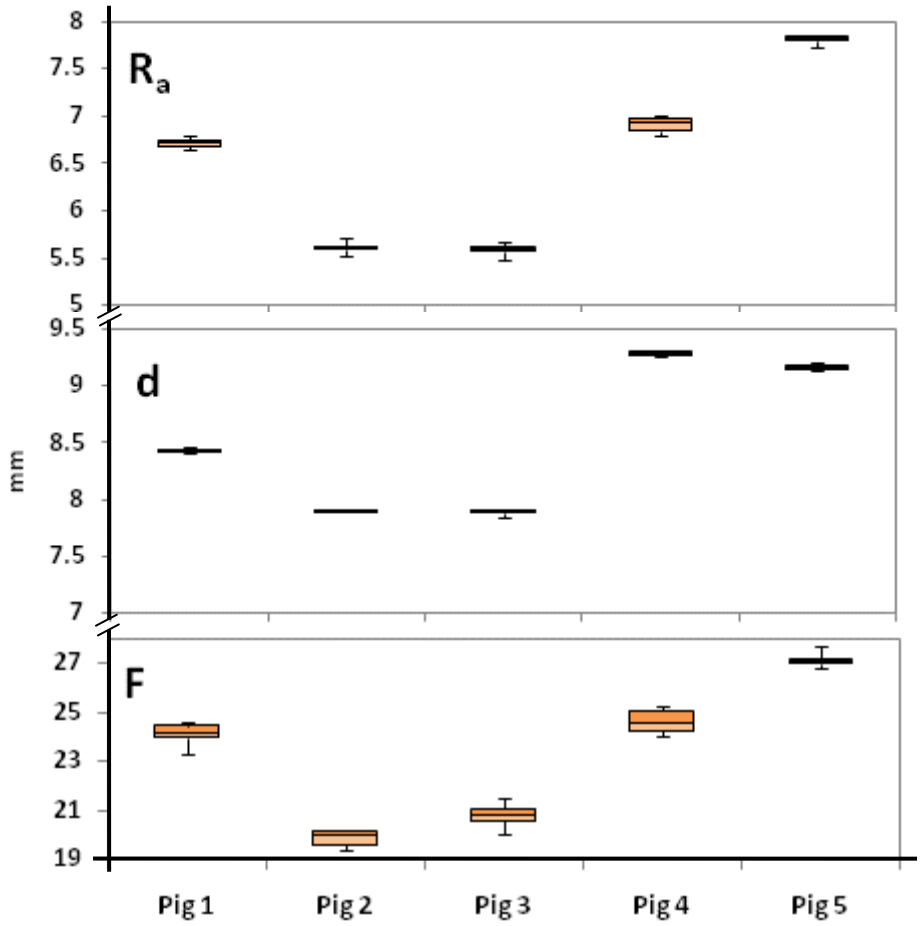

Figure 4.2: Demonstration of the variability and individuality of the lens variables for the anterior radius (top), diameter (middle), and focal length (bottom) measured 5 times for 6 different pig lenses.

4.2 Application of Biometric Measurements to the Lens Model

4.2.1 Choice of Surface and Core Refractive Index Values

Three parameters are present in the model for which no direct measurements were performed; the surface and core refractive index values, n_s and n_c, and the fit parameter W. The first two are considered here and the last in the next section.

It was not planned for this thesis to measure these refractive indices since these have been well studied and reported by several different authors. Reported measurements are summarized in Tables 4.6, 4.7, and 4.8 for rabbit, cow and pig lenses respectively. The refractive indices were converted to the ray tracing wavelength of 647nm used in this thesis using the formula[21]:

$$n(\lambda) = \frac{2[n_0 + (\lambda_0^2 - \lambda^2)m_b - (\lambda_0 - \lambda)b_b]}{[\lambda + (\lambda_0^2 - \lambda^2)m_m - (\lambda_0 - \lambda)b_m]} - n_0 \quad (4.1)$$

where n_0 = refractive index measured at wavelength λ_0, n = refractive index calculated at the desired wavelength, λ, $m_m = 0.605 \cdot 10^{-6} \text{nm}^{-2}$, $m_b = 0.754 \cdot 10^{-6} \text{nm}^{-2}$, $b_m = 0.834 \cdot 10^{-3} \text{nm}^{-1}$, and $b_b = 1.037 \cdot 10^{-3} \text{nm}^{-1}$. These coefficients were derived from fitting data of refractive index measurements vs. wavelength of various ocular media[22]. The measurements by Sivak are much higher than those of other authors; this could be due to the fact that the index was measured using a Pulfrich refractometer; measurements using this instrument are dependent on measurement of a viewing angle which may have been operator dependant.

A few authors tested their index measurement against their crystalline lens models' prediction of focal length and measured focal lengths to test their model. Specifically, the study by Jones (2004)[23] for pig lenses, Nakao (1968)[26] for rabbit lenses, and Chan (1988)[28] for cow lenses. The surface and core refractive index values (or the average in the case of a published range) from each of these studies were entered into the proposed lens model and focal length for each lens calculated. For the pig and rabbit lenses the calculated focal lengths were within the measured data reported for this thesis. For cow lenses, the index values provided by Chan (1988)[28] produced significant differences in predicted focal lengths, while the indices reported by Pierscionek (1989)[22] predicted the measured focal lengths correctly. When the surface and core refractive index values were entered into the proposed lens model, the focal length was not correctly predicted. The core and surface index values for pig, rabbit, and cow lenses used in the lens model are shown in Table 4.9 with their source.

Table 4.6: Comparison of pig crystalline lens core and surface refractive index measurements by various authors. n_c: core refractive index, n_s: surface refractive index.

Author (year)	Index	Measured Value	Wavelength Measured	Converted Value 647nm	Measurement Method
Sivak(1982)[5]	n_c	1.4346	440nm	1.4204	Pulfrich Refractometer
	n_c	1.4307	486nm	1.4213	
	n_c	1.4246	590nm	1.4226	
	n_c	1.4218	650nm	1.4219	
	n_s	1.4240	440nm	1.4105	
	n_s	1.4179	486nm	1.4091	
	n_s	1.4121	590nm	1.4102	
	n_s	1.4105	650nm	1.4106	
Jones (2004)[7]	n_c	1.4374 +/- 0.0007	543.5nm	1.432	MRI
	n_s	1.365 – 1.368	543.5nm	1.362 – 1.365	
Pierscionek (2005)[23]	n_c	1.396	633nm	1.396	Laser ray tracing
	n_c	1.404	532nm	1.399	
	n_s	1.354	633nm	1.354	
	n_s	1.358	532nm	1.354	
Vazquez (2006)[24]	n_c	1.440	633nm	1.440	Optical tomography
	n_s	1.370	633nm	1.370	

Table 4.7: Rabbit crystalline lens core and surface refractive index measurements.

Author (year)	Index	Measured Value	Wavelength Measured	Converted Value (647nm)	Measurement Method
Nakao (1968)[25]	n_c	1.431 – 1.464	589nm	1.429 – 1.462	Abbe Refractometer
	n_s	1.384 – 1.393	589nm	1.382 – 1.391	

Table 4.8: Comparison of cow crystalline lens core and surface refractive index measurements by various authors

Author (year)	Index	Measured Value	Wavelength Measured	Converted Value 647nm	Measurement Method
Bettleheim (1974)[26]	n_c	1.3806 – 1.3945	632.8nm	1.3803 – 1.3942	Light Scattering
Sivak (1982)[22]	n_c	1.4759	440nm	1.4588	Pulfrich refractometer
	n_c	1.4700	486nm	1.4588	
	n_c	1.4629	590nm	1.4605	
	n_c	1.4593	650nm	1.4594	
	n_s	1.4162	440nm	1.4033	
	n_s	1.4117	486nm	1.4032	
	n_s	1.4057	590nm	1.4039	
	n_s	1.4033	650nm	1.4034	
Chan (1988)[27]	n_c	1.453	632.8nm	1.453	Laser ray tracing
	n_s	1.350	632.8nm	1.35	
Pierscionek (1989) [28]	n_c	1.450 – 1.452	632.8nm	1.450 – 1.452	Laser ray tracing
	n_s	1.340	632.8nm	1.340	

Pierscionek (1992)[29]	$\mathbf{n_c}$	1.460-1.474	632.8nm	1.460	Laser ray tracing
	$\mathbf{n_s}$	1.380	632.8nm	1.380	
Pierscionek (1994) [30]	$\mathbf{n_s}$	1.395 – 1.408	670nm	1.395 – 1.408	Fiber optic probe
	$\mathbf{n_s}$	1.381 – 1.388	589nm	1.379 – 1.386	Abbe refractometer

Table 4.9: Refractive index core and surface values used in the customizable crystalline lens model for pig, rabbit, and cow lenses.

Species	Index	Value used in model	Source of index value
Pig	$\mathbf{n_c}$	1.432	Jones (2004)[7]
	$\mathbf{n_s}$	1.364	
Rabbit	$\mathbf{n_c}$	1.446	Nakao (1968)[31]
	$\mathbf{n_s}$	1.387	
Cow	$\mathbf{n_c}$	1.460	Pierscionek (1989)[22]
	$\mathbf{n_s}$	1.380	

4.2.2 Investigation of the GRIN index parameter *W*

The crystalline lens model was used with all of the variables found above to determine the GRIN index parameter, W for each lens. This was done by entering the measured anterior and posterior radius of curvature, asphericity, anterior and posterior thickness and diameter for each individual lens, along with the average C_0, C_1, and C_2 values for each lens. The equations describing the lens model are presented again here for reference. The outer lens surfaces were described by:

$$z = \frac{(x^2 + y^2)c}{1 + \sqrt{(x^2 + y^2)c^2(1 + q)}} \tag{4.2}$$

and the GRIN distribution inside the lens was described by:

$$n(r,z) = n_c \sqrt{1 - \left(\frac{n_c^2 - n_s^2}{n_c^2}\right) p(r,z)} \tag{4.3}$$

$$p(r,z) = C_0 + C_1 K(r,z)^2 + C_2 K(r,z)^4 \tag{4.4}$$

$$K(r,z) = \sqrt{\left(\frac{r}{b}\right)^2 + \left(\frac{z}{\left[1 - \sqrt{k(r,z)}\right]^W (b-a) + a}\right)^2} \tag{4.5}$$

$$k(r,z) = \left(\frac{r}{b}\right)^2 + \left(\frac{z}{a}\right)^2 \tag{4.6}$$

The variables in the surface equation (4.2) are the surface curvature, ($c = 1/R$, where R is the radius of curvature), and the asphericity, q. The front and back surface are each uniquely described and therefore there are four variables, R_a, R_p, q_a, and q_p. The variables in equations (4.2) to (4.5) in the description of the GRIN are n_c and n_s, the central and surface index respectively, C_0, C_1 and C_2, the GRIN equatorial shape coefficients, W, the GRIN fit parameter, and a and b, the lens half thickness along the z axis and radius in the equatorial plane, respectively. Equation (4.4) will have 2 independent forms, one each for the anterior and posterior lens halves.

Each lens' (22 pig, 7 rabbit, and 6 cow) biometry data were entered into the customized crystalline lens model using Zemax® (Zemax Development Corporation) optical modeling software and each lens' predicted focal length and spherical aberration recorded as a function of the GRIN fit parameter W. A value of W for the model was then selected for each lens by plotting the calculated SA vs W and determining the W that calculated the measured SA, as shown in Figure 4.3a.

The first clear result of this modeling was that W was critical to the amount of SA calculated for any single lens while W had only a very small effect on the focal length of the lens as seen in Figure 4.3 showing two randomly selected rabbit lenses as an example. Each rabbit, cow and pig lens follows a slightly different dependence in predicted SA as a function of W and has an individual value of W which best predicts the measured SA. This process of determining W by finding the W that calculated the measured SA was followed for each lens. During these calculations, the calculated focal length was always equal to the measured focal length within measurement errors for the W that fit the SA. The measurement of the focal length was not accurate enough to warrant a specific W that would calculate the focal length equal to the measured focal length.

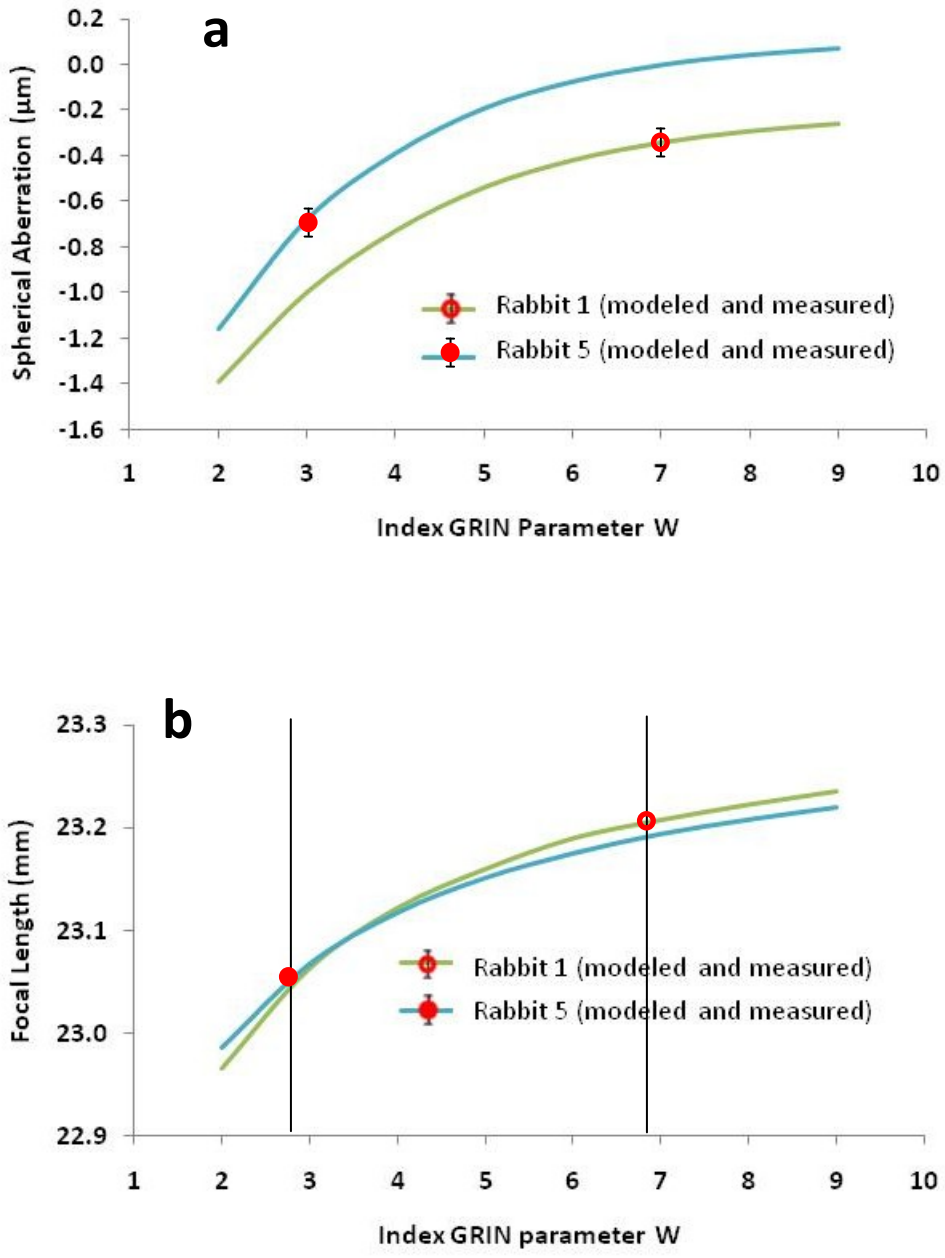

Figure 4.3: Spherical aberration (a) and focal length (b) vs. index GRIN parameter *W* for two different rabbit lenses. The spherical aberration and focal length were calculated using the lens model in Zemax while varying *W*. The measured spherical aberration and focal length are indicated on the plots by red dots. The error bars above and below the red dots indicate one standard deviation for each measurement. One standard deviation of measurement variability in focal length measurement is larger than the plot range (1σ = ±0.5mm).

4.2.3 Effect of Measurement Variation on Lens Model Calculations

The effect of the measurement variation of the lens parameters on the lens model was assessed using the 5 repeated measures performed on 6 pig lenses. Using the crystalline lens model in Zemax, the spherical aberration and focal length were calculated for biometric and equatorial GRIN parameter values which covered a range of two standard deviations of measurement variation for each of the model parameter (Table 4.10). The measurement variation range of two standard deviations was chosen to show a confidence interval in the model of 95%. Each parameter was evaluated one at a time, while holding all other variables constant at their average values for each lens. This allowed for an evaluation of the impact of the measurement variation of each parameter on SA and focal length to better understand the reliability of the model and which parameters were critical. Shown in Table 4.11 are results for the worst case performing pig lens.

Table 4.10: Measured spherical aberration and focal length with ± 2 standard deviations of measurement variation from 5 repeated measures of 6 pig lenses.

Variable	Measured	Measurement Range (±2σ)
Spherical Aberration	-0.57μm	-0.66 – -0.48μm
Focal Length	26.2mm	25.0 – 27.3mm

Table 4.11: Summary of the effect of the measurement variation of each variable on the calculated spherical aberration and focal length using the lens model. The calculated confidence interval of the predicted SA and FL is ± 2 standard deviations of measurement variation. Those variables with calculated spherical aberration falling outside of the measurement variation range are highlighted.

Variable	Value (±2σ)	Predicted SA Range (±2σ)	Predicted FL range (±2σ)
C_0	0.010 ± 0.012*	-0.57 – -0.57μm	26.2 – 26.5mm
C_1	0.41 ± 0.06	-0.68 – -0.46μm	25.8 – 27.0mm
C_2	0.60 ± 0.12	-0.67 – -0.47μm	26.1 – 26.6mm
R_a	6.07 ± 0.12	-0.62 – -0.53μm	26.3 – 26.4mm
R_p	-4.35 ± 0.10	-0.91 – -0.19μm	26.3 – 26.4mm
q_a	1.32 ± 0.06	-0.65 – -0.50μm	26.4 – 26.4mm
q_p	-0.10 ± 0.02	-0.53 – -0.42μm	26.4 – 26.4mm
a_a	2.85 ± 0.02	-0.63 – -0.50μm	26.3 – 26.4mm
a_p	3.72 ± 0.02	-0.85 – -0.30μm	26.3 – 26.4mm
a	6.57 ± 0.04	-0.73 – -0.41μm	26.3 – 26.4mm
b	4.26 ± 0.02	-0.77 – -0.36μm	26.3 – 26.4mm

*limited to >0; within calculated limits

None of the equatorial coefficient measurement variation resulted in a predicted focal length outside of the 95% confidence limits of the measured values. The

coefficients C_1, C_2, and the lens equatorial radius b have just enough impact on the predicted SA that their range falls outside the 95% confidence limits of the measured values. The predicted values fell within 94.2% of C_1, 92.8% of C_2, and 84.8% of b measurements fell within the measurement variation range of the spherical aberration.

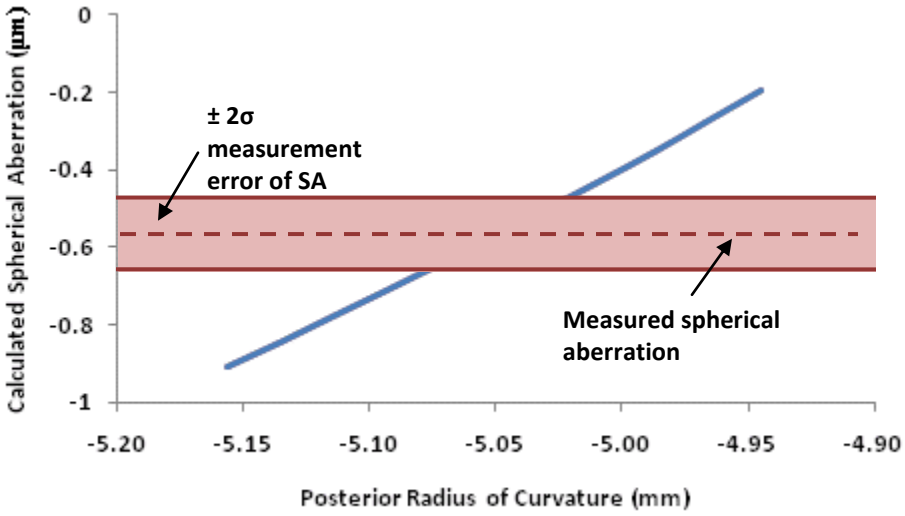

Figure 4.4: Spherical aberration calculated using the lens model vs. varying values of the measured posterior radius of curvature for one pig lens. R_P was varied over two standard deviations; the mean value of -5.05 is in the centre of this plot. The dotted line represents the mean value of spherical aberration measured for this particular pig lens. The shaded area represents two standard deviations of measurement error. This plot shows that two standard deviations of the measurement error of R_P is slightly outside the measurement variation of the spherical aberration.

The variable with the largest impact on the range of predicted SA was the radius of curvature of the posterior lens surface since it has the greatest impact on the calculated range of the spherical aberration, not because it has a large measurement error. This is illustrated in Figure 4.4 showing the calculated spherical aberration vs. the posterior radius of curvature, R_p, for one pig lens, varying R_p over two standard deviations of measurement error. The calculated error function indicated only 72.9% of the measurements for the posterior radius of curvature fall within the measured 95% variance range of the spherical aberration. This is still better than one standard deviation (68.3%) and therefore the model is still considered to be valid, however the measurement of the posterior radius of curvature should be considered critical for the accuracy of the model.

4.3 Measured Biometric and Optical Relationships

As discussed in section 2.3, it is clear that there are strong linear relationships between the lens' optical and biometric properties and between certain biometric properties. As a starting point to investigate these relationships, a Pearson correlation coefficient (r) table was calculated considering all optical and biometric properties measured. For those relationships with significant correlation ($P < 0.05$) a linear regression was performed to obtain the specific relationship between each set of variables. As suggested by Vilupuru (2001)[4], orthogonal regressions were computed instead of linear regressions to obtain a more realistic estimate of the variance since there is no clear independent variable as all variables are measured from real lenses. These results are summarized in Tables 4.12 to 4.14. The intercept m_1, slope m_2, and correlation coefficient r are shown for the best fit for each pair of variables. Full fit results including the errors on each slope and all P values for the correlation coefficients are given in Appendix C. Figure 4.5 shows an example of data for pig lenses along with the orthogonal regression line and the correlation coefficient for some of these relationships. Although there were many significant correlations relating lens size, curvatures and optical properties, no significant correlations were found between the posterior asphericity and any other measured property, most likely since more than half of all of the lenses measured for each species had a posterior asphericity equal to 0. There were no linear relationships found between the measured spherical aberration or the GRIN distribution parameter, W, and any of the other measured lens properties, shown in Figure 4.6 for pig lenses as an example.

The correlations found for the rabbit lenses were much lower than those seen for the pig and cow lenses. One likely reason for this is the age of the rabbit lenses – these lenses where obtained from a university laboratory where they were raised in exactly the same manner and all are precisely the same age, sex, weight, etc. to control experimental parameters and therefore they were most likely not a representative of a normal population of rabbits. It would be preferable to obtain a broader sample of a normal rabbit population to confirm some of these results.

Table 4.12: Optical and biometric relationships calculated for pig lens measurements. Significant relationships were calculated for r > 0.423 (p < 0.050) given N = 22 samples. m_1 refers to the x-axis intercept and m_2 refers to the slope of the line of best fit.
KEY: R_a: anterior radius of curvature, R_p: posterior radius of curvature, q_a: anterior asphericity, q_p: posterior asphericity, t: thickness, a_a: anterior thickness, a_p: posterior thickness, b: radius, F: focal length, S. A.: spherical aberration.

y→ / x↓		R_a	q_a	R_p	t	a_a	a_p	b	F	SA	W
	m_1	X	0.221	-0.511	0.701	0.336	0.404	0.828	3.156		
R_a	m_2	X	-0.089	-1.099	2.030	0.673	1.086	3.233	2.502		
	r	X	0.956	-0.96	0.959	0.942	0.944	0.874	0.980	-0.085	-0.052
	m_1	4.320	X	-2.320	1.314	1.605	1.673	6.092	13.826		
q_a	m_2	0.647	X	-1.338	0.803	0.693	1.468	0.401	4.558		
	r	0.956	X	-0.894	0.958	0.892	0.865	0.819	0.922	-0.138	-0.101
	m_1	-1.803	-0.382	X	-1.375	-0.558	-0.803	-1.491	-5.791		
R_p	m_2	1.495	0.344	X	-0.556	-0.408	-0.234	-1.986	2.559		
	r	-0.960	-0.894	X	-0.961	-0.934	-0.954	-0.938	-0.955	0.053	0.075
	m_1	1.402	0.242	-0.672	X	0.426	0.579	1.141	4.584		
t	m_2	-2.718	-0.272	0.064	X	0.053	-0.088	1.023	-7.320		
	r	0.959	0.958	-0.961	X	0.979	0.988	0.937	0.928	-0.013	-0.031
	m_1	2.982	0.633	-1.558	2.290	X	1.288	3.062	9.324		
a_a	m_2	-2.026	-0.461	0.072	0.037	X	0.042	-0.228	-3.635		
	r	0.942	0.892	-0.934	0.979	X	0.936	0.912	0.914	-0.024	-0.029
	m_1	2.19	0.464	-1.169	1.687	0.687	X	1.853	8.477		
a_p	m_2	-1.673	-0.383	-0.016	0.303	0.303	X	1.638	-8.340		
	r	0.944	0.865	-0.954	0.988	0.936	X	0.929	0.913	-0.005	0.030
	m_1	1.078	0.157	-0.589	0.791	0.338	0.479	X	4.621		
b	m_2	-2.79	0.004	0.646	-0.149	-0.03	-0.342	X	-16.529		
	r	0.874	0.819	-0.938	0.937	0.912	0.929	X	0.859	0.030	-0.111
	m_1	0.305	0.066	-0.157	0.208	0.097	0.109	0.230	X		
F	m_2	-0.504	-0.165	-0.790	1.823	0.646	1.22	3.279	X		
	r	0.980	0.922	-0.955	0.928	0.914	0.913	0.859	X	-0.118	0.009
	m_1									X	
SA	m_2									X	
	r	-0.085	-0.138	0.053	-0.013	-0.024	-0.005	0.030	-0.118	X	0.076
	m_1										X
W	m_2										X
	r	-0.052	-0.101	0.075	-0.031	-0.029	0.030	-0.111	0.009	0.076	X

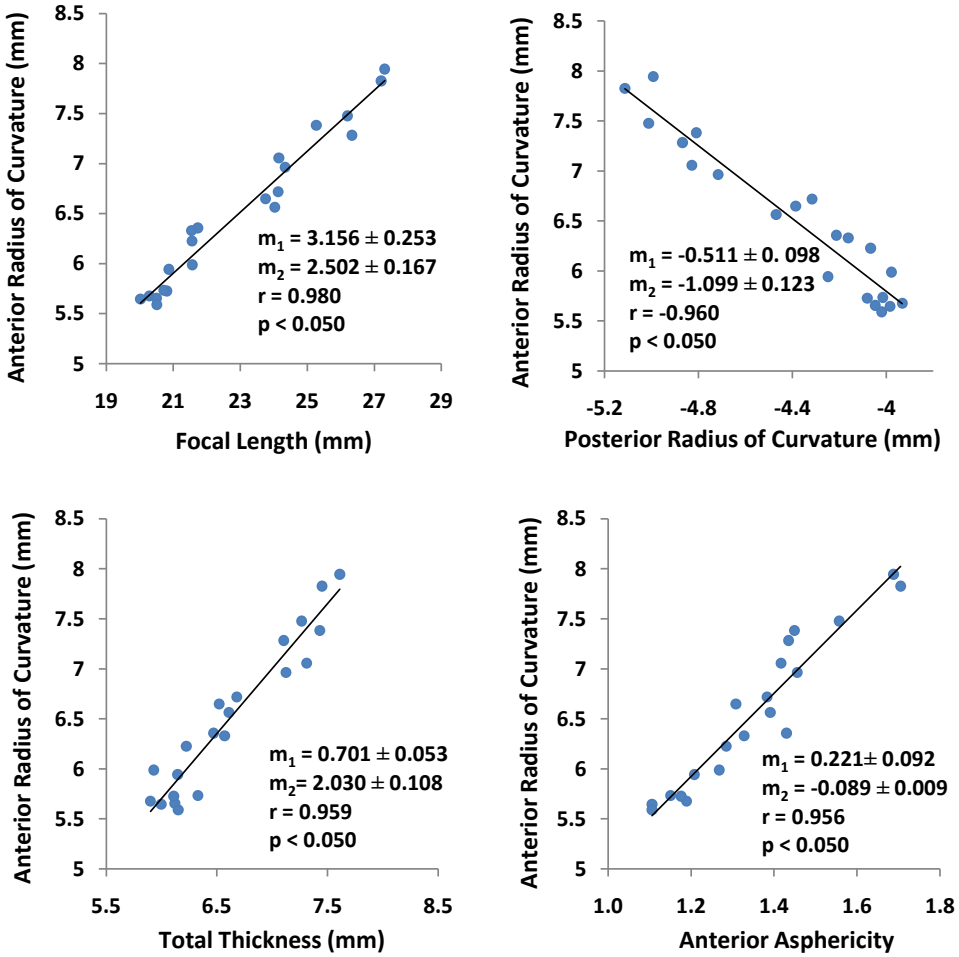

Figure 4.5: Linear biometric and optical relationships calculated from orthogonal regressions for pig crystalline lenses. Shown here are the linear relationships between the anterior radius of curvature of the lens and (a) focal length, (b) posterior radius of curvature, (c) lens thickness, and (d) anterior surface asphericity. The intercept and slope (and associated errors) for the orthogonal lines of best fit are indicated by m_1 and m_2, respectively.

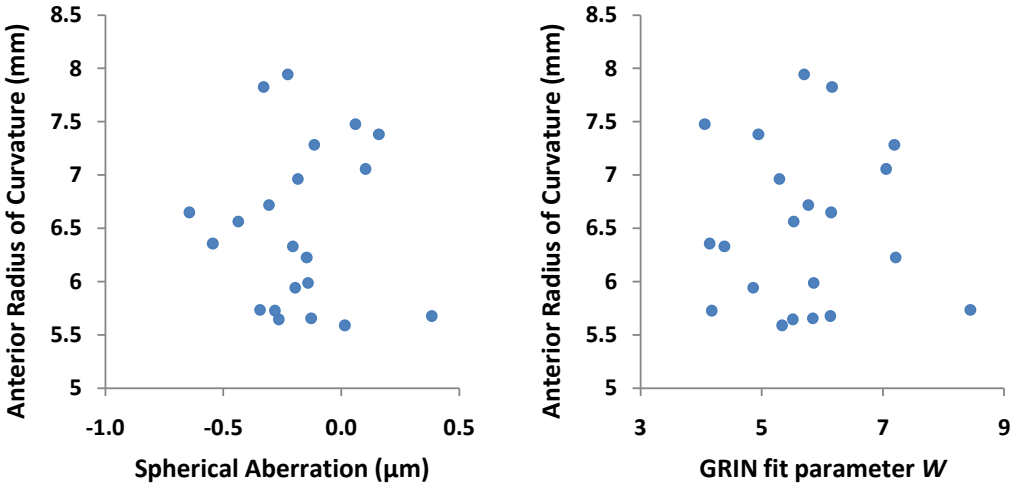

Figure 4.6: Demonstration of the lack of correlation between the anterior radius of curvature vs. spherical aberration (left) and *W* (right) for pig lenses. No significant correlation of any kind was found between the spherical aberration or *W* and any other parameter measured.

Table 4.13: Optical and biometric relationships calculated for rabbit lens measurements. Significant relationships were calculated for r > 0.754 (p < 0.050) given N = 7 samples.

y→ / x↓		R_a	q_a	R_p	t	a_a	a_p	b	F	SA	W
	m_1	X	0.136		0.714	0.178		1.046	3.126		
R_a	m_2	X	0.005		2.435	2.260		2.820	-0.163		
	r	X	0.786	-0.727	0.869	0.788	0.681	0.753	0.859	-0.125	-0.526
	m_1	2.802	X			1.225		5.108			
q_a	m_2	4.570	X			2.337		5.360			
	r	0.786	X	-0.253	0.550	0.952	0.172	0.900	0.688	-0.697	-0.342
	m_1	-0.574		X	-0.512		-0.437		-1.708		
R_p	m_2	-4.123		X	-4.805		-1.645		-13.231		
	r	-0.727	-0.253	X	-0.788	-0.265	-0.873	-0.119	-0.593	-0.387	-0.342
	m_1	1.060		-1.210	X		0.700		3.720		
t	m_2	-0.757		3.627	X		-1.263		-5.640		
	r	0.869	0.550	-0.788	X	0.685	0.909	0.427	0.837	0.045	-0.687
	m_1	2.187	0.740			X		3.183			
a_a	m_2	-0.397	-1.628			X		-0.869			
	r	0.788	0.952	-0.265	0.685	X	0.319	0.830	0.735	-0.659	-0.551
	m_1			-1.745	1.181		X				
a_p	m_2			1.491	2.837		X				
	r	0.681	0.172	-0.873	0.909	0.319	X	0.082	0.668	0.435	-0.579
	m_1	0.546	0.182			0.216		X			
b	m_2	1.695	-0.900			1.309		X			
	r	0.753	0.900	-0.119	0.427	0.830	0.082	X	0.657	-0.538	-0.320
	m_1	0.204			0.188				X		
F	m_2	2.724			3.383				X		
	r	0.859	0.688	-0.593	0.837	0.735	0.668	0.657	X	-0.166	-0.624
	m_1									X	
SA	m_2									X	
	r	-0.125	-0.697	-0.387	0.045	-0.659	0.435	-0.538	-0.166	X	0.122
	m_1										X
W	m_2										X
	r	-0.526	-0.342	0.342	-0.687	-0.551	-0.579	-0.320	-0.624	0.122	X

Table 4.14: Optical and biometric relationships calculated for cow lens measurements. Significant relationships were calculated for r > 0.811 (p < 0.050) given N = 6 samples.

y→ / x↓		R_a	q_a	R_p	t	a_a	a_p	b	F	SA	W
	m_1	X	0.230	-0.767	1.271	0.413	0.335	0.921	2.341		
R_a	m_2	X	-1.742	-0.790	-2.862	0.325	3.145	5.520	6.755		
	r	X	0.950	-0.984	0.971	0.952	0.939	0.958	0.948	-0.442	0.012
	m_1	0.230	X	-3.611	5.004	1.897	1.838	3.770	11.418		
q_a	m_2	-1.742	X	-6.231	7.346	3.374	5.516	12.314	22.398		
	r	0.950	X	-0.938	0.897	0.838	0.829	0.887	0.849	-0.376	-0.077
	m_1	-1.265	-0.293	X	-1.590	-0.516	-0.401	-1.157	-2.837		
R_p	m_2	0.605	1.896	X	3.351	-0.097	-3.183	-5.057	-6.539		
	r	-0.984	-0.938	X	-0.939	-0.921	-0.874	-0.934	-0.890	0.554	-0.163
	m_1	0.742	0.164	-0.554	X	0.327	0.247	0.648	1.749		
t	m_2	2.820	-1.032	-3.067	X	1.203	3.980	8.625	13.125		
	r	0.971	0.897	-0.939	X	0.991	0.938	0.883	0.945	-0.286	-0.105
	m_1	2.224	0.465	-1.714	3.010	X	0.785	1.952	5.530		
a_a	m_2	0.242	-1.453	-1.003	-3.399	X	3.058	6.385	5.636		
	r	0.952	0.838	-0.921	0.991	X	0.943	0.874	0.945	-0.307	-0.055
	m_1	2.643	0.573	-1.922	3.512	1.138	X	2.532	6.699		
a_p	m_2	-6.810	-3.022	-3.666	-12.267	-2.908	X	-1.599	-13.245		
	r	0.939	0.829	-0.874	0.938	0.943	X	0.945	0.996	-0.262	-0.165
	m_1	1.000	0.231	-0.619	1.210	0.322	0.354	X	2.384		
b	m_2	-4.514	-2.679	0.239	-7.567	-0.106	1.341	X	-4.953		
	r	0.958	0.887	-0.934	0.883	0.874	0.945	X	0.948	-0.505	0.061
	m_1	0.393	0.087	-0.287	0.512	0.156	0.148	0.363	X		
F	m_2	-1.664	-1.947	-0.005	-5.457	-0.148	2.019	3.948	X		
	r	0.948	0.849	-0.890	0.945	0.945	0.996	0.948	X	-0.253	-0.169
	m_1									X	
SA	m_2									X	
	r	-0.442	-0.376	-0.554	-0.286	-0.307	-0.262	-0.505	-0.253	X	-0.080
	m_1										X
W	m_2										X
	r	0.012	-0.077	-0.163	-0.105	-0.055	-1.650	0.061	-0.169	-0.080	X

The only study on the biometrical relationships for the species studied in this thesis were those done by Vilupuru (2001)[4], for pig lenses, which was already discussed in Chapter 2. Similar relationships were found, for example, the relationship between the anterior and posterior radii of curvature is $m_1 = -0.806$, $m_2 = -0.667$, and in this work the same relationship is $m_1 = -1.099$, $m_2 = -0.511$. Although the values are similar, they are outside of the error range and this was found for all of the other relationships.

Possibilities for discrepancies are most likely due to the fact that the Vilupuru study did not measure aspheric anterior radii of curvatures, which could lead to different measured values of the anterior radii of curvature. Furthermore, the two studies could have used pigs of varying ages or different species of pigs with different biometric relationships.

These correlations may be used to further simplify the model for any of the mammals measured by reducing the number of parameters required to uniquely describe each lens and reducing the number of measurements needed in a real clinical situation to set the lens model for an individual. There are enough relationships that exist such that if only the lens thickness is known, all of the other required parameters can be uniquely defined in the model by calculating them using these relationships. The only parameter that remains to be defined is the SA, which must be found for each lens by customizing W. Therefore W is the only parameter that must be determined by a fitting process, all other parameters are determined from clinically obtainable measurements.

4.4 Model Validation

The last step in the development of the customizable crystalline lens model is the validation of its simplified form. The lens thickness measurements for each pig lens were used to calculate the remaining parameters required in the model from the linear relationships shown in Table 4.12. These parameters were entered into the model and the measured spherical aberration was then used to find W. Once W was found, this was used to determine the model lens' focal length. In other words, C_0, C_1 and C_2 were constants, the measured thickness (t) was the independent variable, the remaining biometric parameters: anterior radius of curvature (R_a), posterior radius of curvature (R_p), anterior asphericity (q_a), posterior asphericity (q_p), anterior thickness (a_a) posterior thickness (a_p), and the radius (b) were the dependent variables, and W was a constrained variable in the lens model.

The focal length, spherical aberration, and lens thickness were the only original measured parameters used in the model validation since, as discussed previously, the lens model is to be further developed for use as part of a customizable model of the whole human eye, and these are the only parameters that are measurable with any accuracy in-vivo.

Plots of calculated spherical aberration vs. W are shown in Figure 4.7 for two randomly selected and representative pig lenses. Both curves were calculated using all of the original measurements (labeled original data) and for the simplified model (labeled modeled data) are presented for comparison. Note the spherical aberration calculated using the modeled data agree very well with the spherical aberration calculated using the original data. Because of the methodology – the modeled fit parameter W was selected so the model's predicted SA was within measurement error of the measured SA and thus is always not significantly different.

The measured and modeled focal lengths of the 22 pig lenses are shown in Figures 4.8 and 4.9 for comparison. Figure 4.8 shows the measured focal lengths with their associated measurement error and the calculated focal lengths for each pig lens. The average percentage error between the measured focal length and the modeled focal length for all pigs was 3.6% with a standard deviation of 2.1%, and the largest single error was 9.1%. Figure 4.9 compares the measured focal length vs. the calculated focal length using the model with an orthogonal regression. If the slope of the orthogonal regression line is 1 and the intercept is 0, then the measured and modeled parameters can be considered to be not significantly different. In order test if the slope was statistically different from 1, the slope and the intercept were compared to a data set having a slope of 1 and an intercept of zero; the data set of measured focal length vs. measured focal length. Then analysis of covariance (ANCOVA[20]) was applied, to compare the two different linear regression lines. Using this method, p-values of 0.511 and 0.824 were obtained for comparison of the slopes and the intercepts, respectively. This means that the modeled and measured focal lengths were not statistically significantly different from each other and the model can be considered to be successful in describing the focal length of the pig lenses.

The same procedure was applied for all cow lenses to test the model using a different species, and the measured and predicted focal length for these lenses are shown in Figure 4.10. The average percentage error between the measured focal length and the modeled focal length for the measurement group of cows was 2.7% with a standard deviation of 1.9%, and the largest single error was 6.3%. This shows that the model can predict the optical performance of individual lenses of different species.

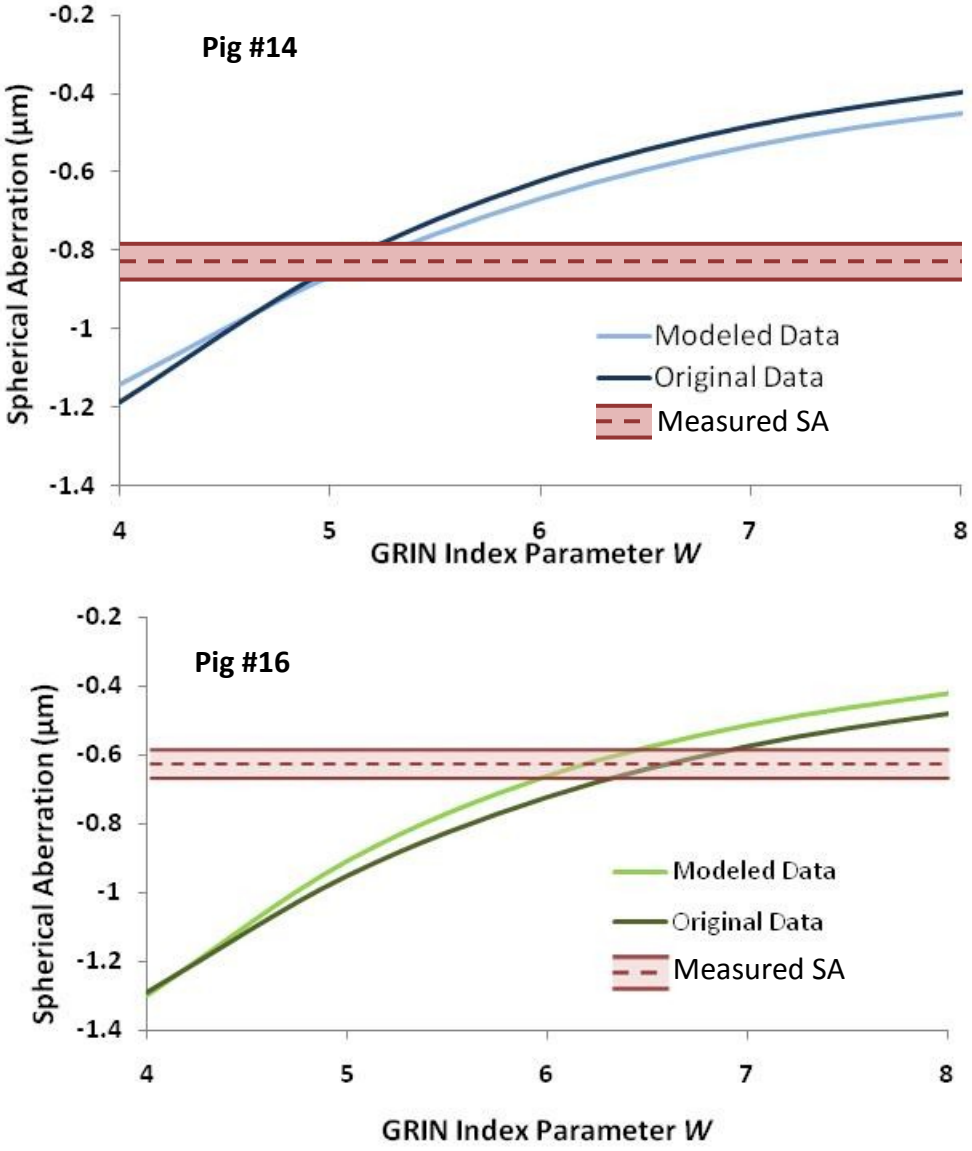

Figure 4.7: Calculated and measured spherical aberration vs. GRIN index parameter *W* for two different pig lenses. The dark blue curve was calculated using the original measured biometrical data. The light blue curve for pig #14 and the light green curve for pig #16 was calculated using only the measured lens focal length and thickness, and the rest of the required variables were calculated using the biometric linear relationships. The measured spherical aberration is indicated on the plot by red dots on each curve. The corresponding *W* for each curve was slightly different. *W* corresponding to the modeled data was used to find the lens focal length calculated from the model.

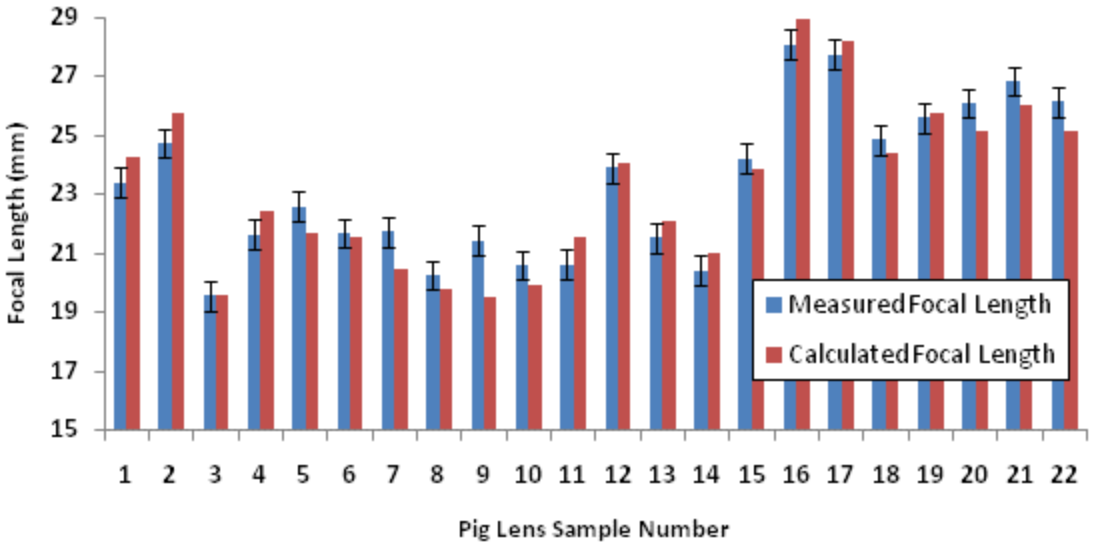

Figure 4.8: Measured focal length of all pig lenses and calculated focal length using the lens model. The largest percentage error between the measured and calculated focal length is 9.1% for pig 9. The average percentage error for the entire group is 3.6%.

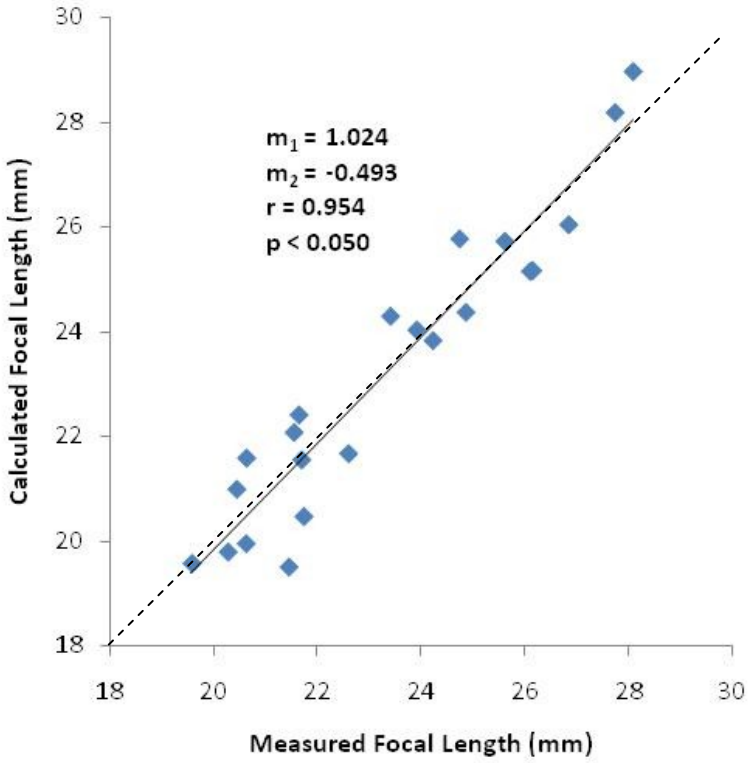

Figure 4.9: Orthogonal regression between Focal length calculated from the customizable crystalline lens model and the measured focal length for 22 pig lenses.

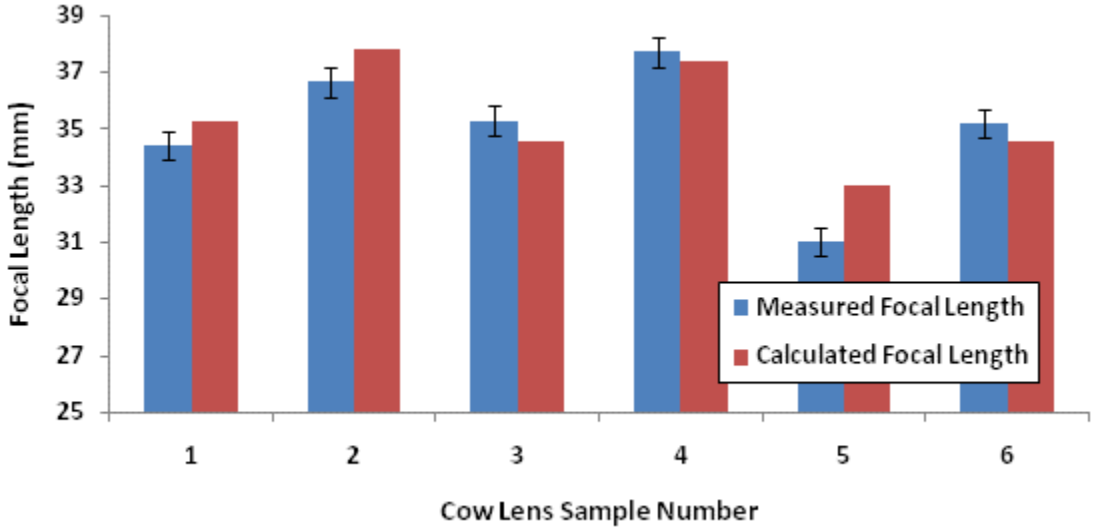

Figure 4.10: Measured focal length of all cow lenses and calculated focal length using the lens model. The largest percentage error between the measured and calculated focal length is 6.3% for cow 5. The average percentage error for the entire group is 2.7%.

4.5 Applicability to a Human Lens Model

The customizable model, as it is presented here has not been validated in human lenses. For the model to be valid for humans the GRIN index parameters must be measured and the biometric and optical relationships must be first established. Linear biometric and optic relationships have been investigated by Manns (2004)[33] and Glasser (1999)[34] for human lenses as discussed in Chapter 1, therefore it has been shown that they are present, however more relationships are needed in terms of the lens thickness and diameter as these are required lens model parameters. The measure of the crystalline lens thickness is critical in this model as it is used to predict all of the remaining lens biometric parameters, required to determine the value of the fit parameter W which customizes the lens gradient for each individual.

References

[1] A. Roorda, A. Glasser, “Wave aberrations of the isolated crystalline lens,” J. Vis. 4, 250-261 (2004).

[2] E. Acosta, J. Bueno, C. Schwarz, P. Artal, “Relationship between wave aberrations and histological features in ex vivo porcine crystalline lenses,” J. Biomed. Opt. **15**, 5, 1-4 (2010).

[3] R. K. Tyson, “Conversion of Zernike aberration coefficients to Seidel and higher-order power-series aberration coefficients," Opt. Lett. **7**, 262- 264 (1982).

[4] G. Conforti, “Zernike aberration coefficients from Seidel and higher-order power series coefficients," Opt. Lett. 8, 390-391 (1983).

[5] J. G. Sivak, R. O. Kreuzer, “Spherical aberration of the crystalline lens,” Vis. Res. **23**, 59-70 (1983).

[6] A. S. Vilupuru, A. Glasser, A. “Optical and biometric relationships of the isolated pig crystalline lens.,” Ophthal. Physiol. Opt. **21**, 4, 296-311 (2001).

[7] C. E. Jones, J. M. Pope “Measuring optical properties of an eye lens using magnetic resonance imaging,” Magn. Reson. Imaging **22**, 211–220 (2004).

[8] S. A. Koopmans, T. Terwee, H. J. Haitjema, H. Deuring, H., S. van Aarle, A. C. Kooijman, “Relation between injected volume and optical parameters in refilled isolated porcine lenses,” Ophthal. Physiol. Opt. 572–579 (2004).

[9] D. Vazquez, E. Acosta, G. Smith, L. Garner, “Tomographic method for measurement of thegradient refractive index of the crystalline lens. II. The rotationally symmetrical lens,” J. Opt. Soc. Am. A **23**, 10, 2551-2565 (2006).

[10] M. A. Reilly, P. D. Hamilton, G. Perry, N. Ravi, “Comparison of the behavior of natural and refilled porcine lenses in a robotic lens stretcher,” Exp. Eye Res. **88**, 483–494 (2009).

[11] A. Huges, “A Schematic Eye for the Rabbit,” Vis. Res. **12**, 123-138 (1972).

[12] J. R. Kuszak, J. G. Sivak, S. A. Moran, S. Sheib, W. H. Garner, T. L. Ke, M. R. Hellberg, G. Graff, “Suppression of post-vitrectomy lens changes in the rabbit by novel benzopyranyl esters and amides,” Exp. Eye. Res. **75,** 459-473 (2002).

[13] C. W. Kong, R. Gerometta, L. J. Alvarez, O. A. Candia, “Changes in rabbit and cow lens shape and volume upon imposition of anisotonic conditions,” Exp. Eye Res. **89**, 469–478 (2009).

[14] J. R. Kuszak, J. G. Sivak, K. L. Herbert, S. Scheib, W. Garner, G. Graff, “The Relationship Between Rabbit Lens Optical Quality and Sutural Anatomy after Vitrectomy,” Exp. Eye Res. **71**, 267- 281 (2000).

[15] J. G. Sivak, M. Yoshimura, J. A. Weerheim, “Effect of Gentamicin and Chloramphenicol on Bovine Lens Optical Function During Culture,” J. Toxico1.-Cut. Oc. Toxicol. **9**, 4, 265-275 (1990).

[16] J. G. Sivak, D. D. Stuart, K. L. Herbert, J. A. Van Oostrom, L. Segal, “Optical Properties of the Cultured Bovine Ocular Lens as an In Vitro Alternative to the Draize Eye Toxicity Test: Preliminary Validation for Alcohols,” Toxicol. Methods **2**, 4, 280-294 (1992).

[17] J. G. Sivak, K. L. Herbert, “Optical damage and recovery of the in vitro bovine ocular lens for alcohols, surfactants, acetates, ketones, aromatics, and some consumer products: a review,” J. Toxico1.-Cut. Oc. Toxicol. **16**, 3, 173-187 (1997).

[18] D. D. Stuart, J. G. Sivak, A. P. Cullen, J. A. Weerheim, C. A. Monteith, "UV-B radiation and the optical properties of cultured bovine lenses," Curr. Eye Res. **10**, 2, 177-184 (1991).

[19] B. K.Pierscionek, R. C. Augusteyn, "Growth related changes to functional parameters in the bovine lens," Biochimica et. Biophysica Acta. 283-290 (1992).

[20] R. Munger, M. C. W. Campbell, I. Belanic, "Refractive index distribution in mammalian lenses: test for elliptical symmetry," OSA Technical Digest Series, VSIA, **2**, 76 - 79 (1990).

[21] L. D. Fisher, G. Van Belle, *Biostatistics, A Methodology for the Health Sciences*, 1993, New York, USA: Wiley-Interscience.

[22] R. H. H. Kroger, "Methods to estimate dispersion in vertebrate ocular media," J Opt Soc Am A **9**, 1486–1490 (1992).

[23] B. K. Pierscionek, "Growth and ageing effects on the refractive index in the equatorial plane of the bovine lens," Vis. Res. **29**, 12, 1759-1766 (1989).

[24] B. K. Pierscionek, A. Belaidi, H. H. Bruun, "Refractive index distribution in the porcine eye lens for 532nm and 633nm light," Eye, **19**, 375–381 (2005).

[25] D. Vazquez, E. Acosta, G. Smith, L. Garner, "Tomographic method for measurement of thegradient refractive index of the crystalline lens. II. The rotationally symmetrical lens," J. Opt. Soc. Am. A **23**, 10, 2551-2565 (2006).

[26] S. Nakao, S. Fujimoto, "Model of Refractive-Index Distribution in the Rabbit Crystalline Lens," Journ. Opt. Soc. Am. **58**, 8, 1125-1130 (1968).

[27] F. A. Bettelheim, T. J. Y. Wang, T. J. Y. Topographic Distribution of Refractive Indices in Bovine Lenses," Exp. Eye Res. **18,** 351-356 (1974).

[28] D. Y. C. Chan, J. P. Ennis, B. K. Pierscionek, G. Smith, "Determination and modeling of the 3-D gradient refractive indices in crystalline lenses," App. Opt. **27**, 5, 926-931 (1988).

[29] B. K. Pierscionek, "Growth and ageing effects on the refractive index in the equatorial plane of the bovine lens," Vis. Res. **29**, 12, 1759-1766 (1989).

[30] B. K. Pierscionek, R. C. Augusteyn, "Growth related changes to functional parameters in the bovine lens," Biochimica et. Biophysica Acta., 283-290 (1992).

[31] B. K. Pierscionek, "Refractive Index of Decapsulated Bovine Lens Surfaces Measured with a Reflectometric Sensor," Vis. Res. **34**, 15, 927-1933 (1990).

[32] S. Nakao, S. Fujimoto, "Model of Refractive-Index Distribution in the Rabbit Crystalline Lens," Journ. Opt. Soc. Am. **58**, 8, 1125-1130 (1968).

[33] B. K. Pierscionek, "Growth and ageing effects on the refractive index in the equatorial plane of the bovine lens," Vis. Res. **29**, 12, 1759-1766 (1989).

[34] F. Manns, V. Fernandeza, S. Zippera, S. Sandadia, M. Hamaouia, A. Hoc, J. M. Parela, "Radius of curvature and asphericity of the anterior and posterior surface of human cadaver crystalline lenses," Exp. Eye Res. **78**, 39–51 (2004).

[35] A. Glasser, M. C. W. Campbell, "Biometric, optical and physical changes in the isolated human crystalline lens with age in relation to presbyopia," Vision Res. **39**, 1991–2015 (1999).

5. Discussion, Conclusions and Future Work

5.1 Discussion

The human eye is an amazing visual system with extraordinary capabilities. The crystalline lens has unique optical properties that allow it to provide remarkable functions within the healty human eye: clear image formation on the retina of both near and distant objects. The human eye is most definitely not without optical errors, including defocus, astigmatism and higher order aberrations. The optical and biometric properties of the eye vary widely across the population, and this fact should come as no surprise as we are all as individual as our fingerprints. It was pointed out in a very early study by Steiger (1913)[1] that average population data cannot be used as constants in models of the human eye. He stated that by using any number of different parameters in an eye model he could produce endless different variations in visual performance. Therefore investigations and clinical solutions based on population mean data are rarely the optimal solution for an individual. Recent advancement in treatments for correcting optical errors of human eyes has attempted to address these issues with wavefront data, however these techniques are still lacking in their ability to model the optical performance of an individual's eye before treatment to obtain the best possible outcome. The need for a system which considers the optical properties of an individual's eye for either research or clinical considerations is clear. Current crystalline lens models (most of which are part of an eye model) also aim to reproduce the optical qualities of the average crystalline lens and suffer the same shortcomings of average eye models. None of these studies on crystalline lens models have attempted to compare an individual human lens model with an individual human experimental result.

This thesis developed and validated a new customizable lens model which is anatomically based and incorporates the more universally accepted anatomical properties of the crystalline lens while allowing for some customizability to model a wide range of individual animal crystalline lenses. In addition to being anatomically based, the lens model must be determined uniquely for each eye using only parameters which can be obtained easily in-vivo (i.e. in a clinical environment) in order to be useful in research and clinical applications. The final novel model proposed in this thesis was developed

from a customized GRIN model first introduced in this thesis, optical and biometric lens data obtained from 3 mammalian species, and published refractive index data.

One of the major differences between this model and others lies in the customizable GRIN parameter, *W* and its use to deviate from the elliptical isoindicial contour model assumed by many others. The shapes of the contours from a representative model of a pig lens in this thesis are compared to the model by Pierscionek(1989)[2] discussed in Chapter 2 with a GRIN having elliptically symmetric isoindicial contours with different eccentricities for the anterior and posterior halves. The shapes of the contours are compared in Figure 5.1; the purpose of the comparison is only to illustrate the contour shape as the locations of the contours are not drawn to scale.

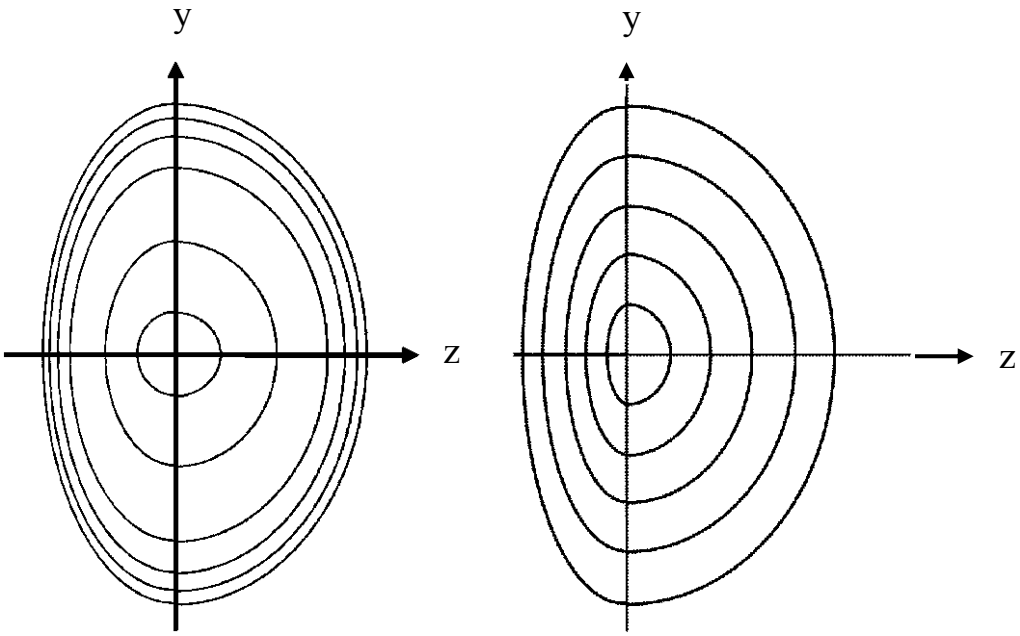

Figure 5.1: Comparison of the isoindicial contours in the sagittal plane developed in this thesis (a) and in the GRIN model developed by Pierscionek et al. (b). Pierscionek's model assumed elliptical contours where this thesis made no assumption other than a spherical core. Notice the tighter isoindical surfaces close to the lens surface and the slower change in gradient at the lens center.

As discussed in Chapter 2, human, cow, rabbit, pig, and other mammalian lenses do not have elliptically symmetric contours so these types of models do not accurately reproduce the lens optical performance. The model GRIN distribution of a pig lens developed in this thesis is shown in Figure 5.2 in the z, x, and y axes. While the GRIN along the x and y axes are the same, the GRIN along the z axis is not. In comparison, when the GRIN derived along the z axis and calculated in the x axis for a human lens from Pierscionek's paper were both plotted together on the same axis (shown in Figure 5.3), it can be seen

that they are actually identical and can be described by the same function since the equatorial index was simply scaled to calculate the GRIN distribution in the sagittal plane. Since the lens modeled in this thesis actually correctly predicted the optical properties of a real crystalline lens while the elliptical model did not, this proves further that one cannot assume elliptical symmetry of the isoindicial contours, and the GRIN along the z and x (or y) axes are not the same function.

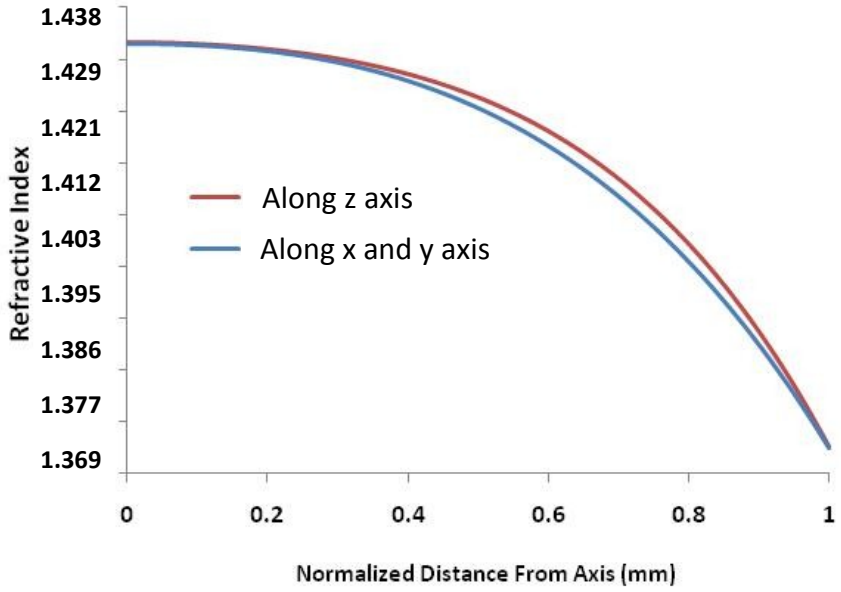

Figure 5.2: GRIN distribution for a pig lens model developed in this thesis along the x, y, and z axes, showing a different function for the z axis.

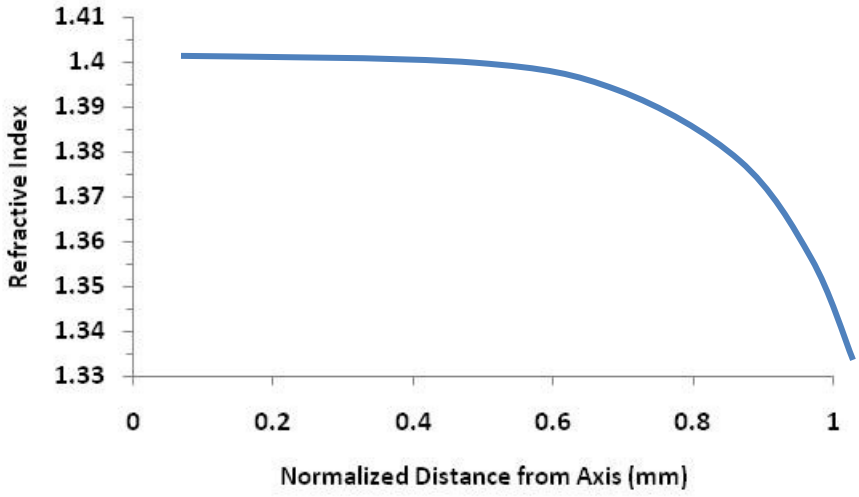

Figure 5.3: Three GRIN distributions for a human lens model developed by Pierscionek (1989)[2] along the x, y, and z axes, indicating the same function describes the GRIN along all axes. The curves all lay directly one on top of the other and therefore are identical.

Upon further investigation of the GRIN in the equatorial plane, it can be seen that Pierscionek's GRIN is much flatter across the central lens region for human lenses when compared to the equatorial GRIN calculated for pig lenses, shown as the plot along the x and y axis in Figure 5.2. This can be further investigated by comparing the equatorial plane GRIN calculated by Pierscionek (2005)[3] for pig lenses and in this thesis for pig lenses, and the equatorial GRIN calculated by Chan (1988)[4] for cow lenses and in this thesis for cow lenses.

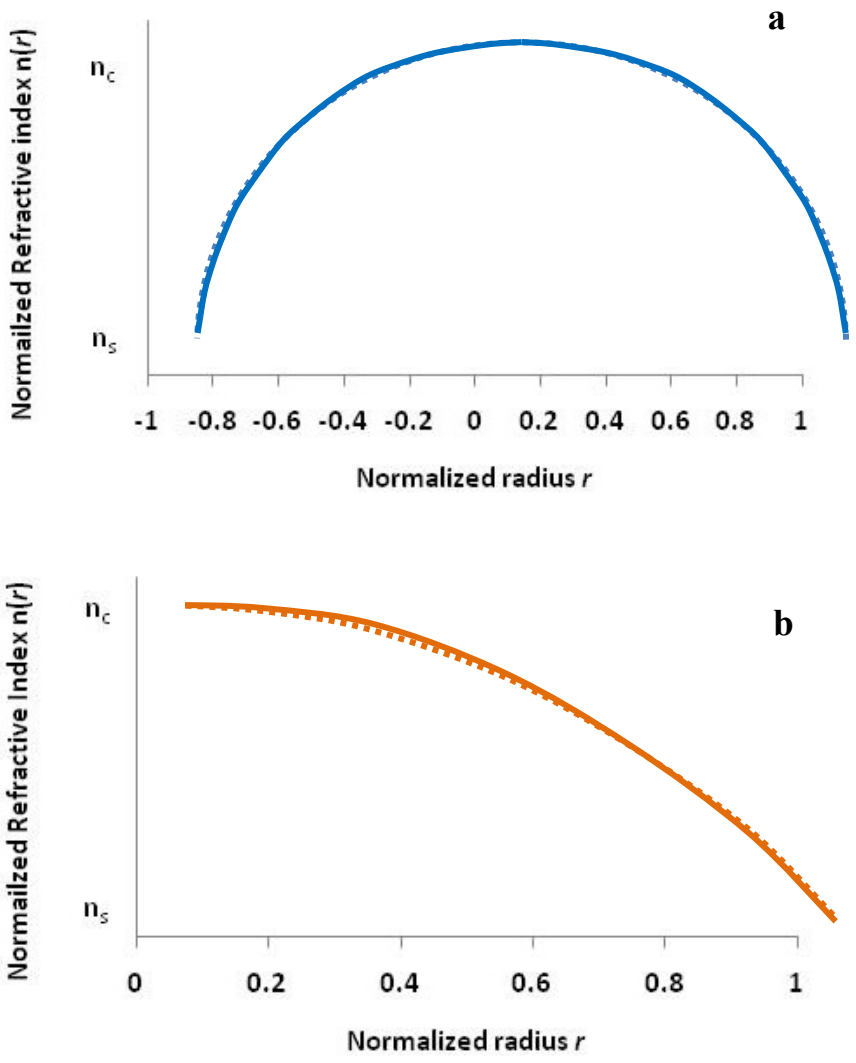

Figure 5.4: Comparison of GRIN measurement distribution in the equatorial plane from Pierscionek(2005)[3] (dotted line) and this thesis (solid line) for pig lenses (a), and from Chan(1989)[4] (dotted line) and this thesis (solid line) for cow lenses (b). The equatorial plane GRIN calculations were all measured using the same technique.

Both studies used the same technique to measure the equatorial GRIN as was used in this thesis. This comparison is shown in Figure 5.4; the plots shown for other's measurements were derived from images in their publications. The equatorial refractive index distributions calculated in this thesis are in good agreement with that calculated by others using the same method. Upon investigation of the shapes of the equatorial GRIN in these species vs. that of the human lens shown above, the profile of the human lens is much flatter across the central region of the lens, which could be due to the age of the human lens shown. This suggests that the GRIN coefficients that were used across species measured in this thesis may not be useable in human lenses. The GRIN coefficients of human lenses must therefore be investigated as a first step in advancing the model developed here for use in the human eye.

In summary, it has been shown in this thesis that an anatomically based customizable GRIN lens model can be constructed that successfully reproduces the optical properties of an individual lens. Importantly, it has been discovered that the shape of the GRIN in the equatorial plane seems to be consistent both within and across species used in this work. This important conclusion lead to the use of the same GRIN distribution coefficients, C_0, C_1, and C_2 for all of the animal lenses modeled in this thesis. If this relation were not true within the same species then the custom model would not work obviously since it is impossible to measure the equatorial index in vivo. This also suggests the possibility that the same human GRIN coefficients may be used once determined for human lenses; however further testing is required to validate this hypothesis.

Additionally, a high level of correlation between the biometric and optical lens parameters was found among the animal lenses studied in this thesis and these linear relationships can be used to reduce the number of parameters in an animal eye model. These optical and biometric relationships were crucial to making this model usable in its proposed role in a full eye model. In order for the model to be developed into a workable in vivo human crystalline lens model, it must be fully specifiable from clinically available measures. The required values to specify the model are the lens focal length, spherical aberration, and thickness. Lens thickness can be measured by using techniques including ultrasound[4] or optical coherence tomography[5]. The focal length and SA of the lens can

be extracted from a wavefront measurement of the whole eye[6]. If enough biometric and optical relationships are found, the focal length and thickness can be used to find all of the other necessary biometric parameters, while the spherical aberration is used to derive the GRIN index parameter, W for each individual lens. Since the other lens parameters rely so heavily on these relationships, it is of paramount importance for the initial measurements to be done properly such that these relationships can be used effectively. For example, if the lens thickness is not accurate, then all of the other parameters determined from this measurement will not be accurate and therefore the lens model will not accurately predict the properties of that lens.

5.2 Conclusions

The following conclusions can be drawn resulting from work in this thesis:

1) The linear relationships present in pig, rabbit and cow crystalline lenses occurring between the lens biometric and optical parameters may be used in the simplification of the custom crystalline lens model.
2) The coefficients describing the equatorial refractive index distribution, C_0, C_1, and C_2 are not significantly different across three different species: pig, rabbits and cows. These relationships may also be used in the simplification of the custom crystalline lens model.
3) A modified version of Chan's method can be used to calculate the GRIN in all planes of the lens by incorporating a variable GRIN parameter that assumes no pre-determined GRIN function that is able to predict the optical aberrations of a lens.
4) A fully customizable crystalline lens model based on anatomical parameters for an individual lens is able to predict the optical performance of real mammalian crystalline lenses.

Finally the working hypothesis was, as stated in Chapter 1: A customizable crystalline lens model can be constructed based on anatomically measured biometric and optical parameters; these parameters have inter-dependent relationships that can be used

to reduce the model's complexity. The three-dimensional distribution of the GRIN of this crystalline lens model can be approximated from the experimentally measured GRIN in one plane (the equatorial plane).

Given that an anatomically based individualizable crystalline lens model was constructed and simplified using measured biometric and optical relationships which successfully predicted the optical properties of an actual crystalline lens, this work demonstrates clearly that the working hypothesis was correct.

5.3 Future Research

As stated previously, the crystalline lens developed in this thesis will eventually be incorporated into a new customizable anatomically correct model of the human eye. This new human eye model will be used both as a clinical tool in the diagnosis and treatment planning of optically based visual problems and as a research tool to study the optical properties of individual human eyes. In order to produce a human eye model from what has been developed here, first what is needed is a continuation of this work to form a model of the human lens.

Most of the work for this has been done already, however a few customizations need to be made. Most importantly, the GRIN in the equatorial plane needs to be determined and if the variation between human lenses is statistically significant or not such that it could be used for all human lenses. This is a critical step as the GRIN of individual lenses cannot be measured and was the main working hypothesis of this model. The surface and core refractive indices have been presented in the literature (as shown in Chapter 1), however, like these indices presented pig, rabbit and cow lenses, there exists some variation in the reported data. An in depth study of these indices would be beneficial to a human crystalline lens model and improve its accuracy greatly. Also, a thorough investigation on the optical and biometric relations of the human lens is required since not all of these relations have been established for human lenses.

The customizable model, as it is presented here, was developed for pig, rabbit and cow crystalline lenses. For each species the model is used for, the biometric and optical relationships for that species must be first established. When modifying this model to represent human lenses, the biometric and optical relationships for human lenses must be

established through rigorous testing. During this testing, extreme care must be taken in the determination of the posterior radius of curvature and total lens thickness since these parameters had the greatest effect on the calculated spherical aberration using the lens model. This is another critical step since the spherical aberration calculated using the model is required in the determination of the GRIN index parameter, *W*.

The integration of the lens model into a model of the eye is not a simple matter and a great deal more research is required in terms of its placement within the eye. As indicated briefly in Chapter 1, the components of the eye are not aligned along a single axis; the lens is tilted and displaced slightly with respect to the axis of the cornea and the fovea. This is paramount in the understanding of the optics of the eye and therefore further investigation of the optical effects of tilt and decentration of the lens within the eye must be undertaken.

Another important factor to take into consideration is the effects of ageing and accommodation on the optical properties of the lens; this was only slightly touched on in this thesis. Several studies have shown that there is a change in refractive index of the surface and core of the lens with ageing; therefore these factors must be taken into account when modeling a lens and the appropriate refractive index values must be applied when modeling an individual's lens and eye. Modeling changes in the eye's optical properties during accommodation requires incorporating a flexible crystalline lens model. A young human lens will assume it's maximally accommodated state upon removal from the eye, whereas an older human lens having undergone presbyopia will not experience the same change in shape. The change in shape of the GRIN under these accommodative changes must be addressed.

Also stated in Chapter 1, the eye is capable of detecting wavelengths from 380 to 770nm with a dynamic range from 25cm in front of the eye to infinity, capable of adapting to light levels ranging from near darkness to very bright sunlight. The attempt of reproducing these dynamic capabilities in an eye model is a great undertaking. Future work addressing these capabilities should also include the study of the chromatic aberrations of the customizable crystalline lens. The parameters of the lens, including the variable GRIN will have an impact on the lens' optical response to colour. The study of

the effects of a variable iris is also required, which also changes the aberration properties of the crystalline lens and eye as mentioned briefly in Chapter 1.

The customizable anatomically correct lens model developed in this thesis is a small but very significant step towards a fully customizable anatomically correct model of the eye and will also provide the scientific community with a tool to better understand the optical properties of the crystalline lens.

References

[1] Steiger, A., *Die Entstehung der spharischen Refraktionen des menschlichen Auges*. Berlin, Karger, 1913.

[2] B. K. Pierscionek, D. Y. Chan, "Refractive index gradient of human lenses," Optom. Vis. Sci. **66**, 12, 822-829 (1989).

[3] Chan, D. Y. C., Ennis, J. P., Pierscionek, B. K., Smith, G., "Determination and modeling of the 3-D gradient refractive indices in crystalline lenses." App. Opt., (1988); 27, 5: 926-931.

[4] B. K. Pierscionek, A. Belaidi, H. H. Bruun, "Refractive index distribution in the porcine eye lens for 532nm and 633nm light," Eye, **19**, 375–381 (2005).

[5] G. Smith, "The optical modeling of the human lens," Ophthal. Physiol. Opt. **11**, 359-369 (1991).

[6] C. Allouch, O. Touzeau, R. Kopito, V. Borderie, L. Laroche, "Crystalline lens biometry using A-scan ultrasound and the Orbscan device," J. Fr. Ophtalmol. **28**, 9, 925-932 (2005).

[7] B. M. Lehman, D. A. Berntsen, M. D. Bailey, K. Zadnik, "Validation of OCT-based Crystalline Lens Thickness Measurements in Children," Optom. Vis. Sci. **86**,3, 181-187 (2009).

[8] P. Artal, J. M. Bueno, A. Guirao, P. M. Prieto, "Aberration Structure of the Human Eye," in *Adaptive Optics for Vision Science*, Porter, Queener, Lin, Thorn, Awwal, ed. John Wiley & Sons, Inc, (2006).

Appendix A

Equatorial GRIN Index Distribution Calculation

The GRIN in the equatorial plane of the lens was calculated using the methods developed by Campbell(1984)[1] and Chan(1988)[2] who both used a modified method of Chu(1977)[3], who produced a method to non-destructively determine the GRIN of optical fibre preforms. The angle made by the laser beam's exit ray as a function of the distance of the original ray with the horizontal axis was used to calculate the refractive index profile in the equatorial plane. The basic geometry is shown in Figure A.1.

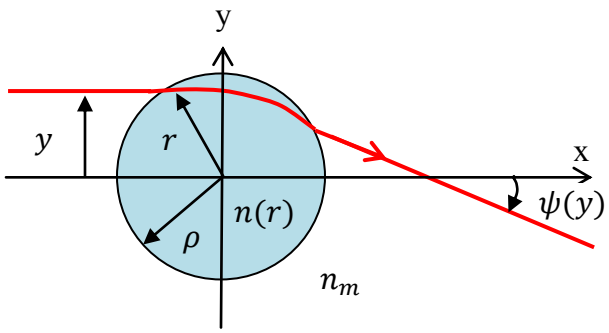

Figure A.1: Schematic diagram of the rays in the equatorial plane and the measured variables used in the GRIN profile calculation. The actual measurements are performed in the equatorial profile.

The beam displacement upon entering the lens is y, and $\psi(y)$ is the exit angle of the beam upon leaving the lens as a function of the beam displacement. The common assumption is made that the lens has rotational symmetry about the z or optic axis. This is generally agreed upon in the literature, as discussed in the previous chapter. The lens refractive index is of the form $n(r,z)$ and the lens can described radially as $r = \sqrt{x^2+y^2}$. Since the plane of interest is the equatorial plane, then $z = 0$ and the refractive index takes the form $n(r)$. Experimentally, the height of the ray above the optic axis y, and its corresponding exit angle, $\psi(y)$ was measured. Using basic geometric optics[4], the exit angle as a function of the entrance beam ray height was written as:

$$\psi(y) = 2\cos^{-1}\frac{y}{\rho} - 2yn_m\int_{r_s}^{\rho}\frac{dr}{r\sqrt{[n^2(r)r^2 - n_m^2y^2]}} \tag{A.1}$$

where n_m is the refractive index of the surrounding medium. The lower limit of the integral, r_s, is solved by the equation:

$$r_s n_m(r_s) = yn_m \tag{A.2}$$

A dimensionless variable ξ and a new function $g(\xi)$ are then introduced:

$$n_m\xi = rn(r) \tag{A.3}$$

$$n(r) = n(\rho)e^{g(\xi)} \tag{A.4}$$

Using these variables, equation (A.1) becomes:

$$\psi(y) = 2\left[\sin^{-1}(y/\rho) - \sin^{-1}(y/\bar{n}\rho) - 2y\int_{y}^{\bar{n}\rho} \frac{d\xi\ g'(\xi)}{\sqrt{\xi^2 + y^2}}\right] \tag{A.5}$$

where

$$\bar{n} = n(\rho)/n_s \tag{A.6}$$

which is the ratio of the refractive index at the edge of the lens and the surrounding medium. When the ratio $\bar{n} = 1$, or in the index matched case, the term in equation (A.5) inside the square brackets vanishes. The resulting equation can then be inverted using an Abel transform. The Abel transform is an integral transform that can be used in the analysis of spherically symmetric functions. Using this transform, (A.5) becomes:

$$g(\xi) = \frac{1}{\pi}\int_{\xi}^{\rho} \frac{dy\ \psi(y)}{\sqrt{y^2 - \xi^2}} \tag{A.7}$$

Now (A.7)(A.7) was calculated since a set of experimentally determined values for $\psi(y)$ and y were obtained. Once $g(\xi)$ was found, the refractive index profile was calculated using:

$$r = \xi e^{-g(\xi)} \tag{A.8}$$

$$n(r) = n(\rho)e^{g(\xi)} \tag{A.9}$$

where $n(\rho) = n_m$ in the index matched case. In the case of this experiment, the refractive index was not matched between the edge of the lens and the surrounding medium, and therefore must be accounted for. In order to remove the effects of this mismatch and still be able to use (A.7) for analysis, the ray height and angle measured experimentally were transformed into equivalent index matched data. This was done by using the transforms:

$$\bar{y} = y/\bar{n} \tag{A.10}$$

$$\bar{\psi}(\bar{y}) = \psi(y) - 2[\sin^{-1}(y/\rho) - \sin^{-1}(y/\bar{n}\rho)] \tag{A.11}$$

The data set $[\bar{\psi}(\bar{y})]$ represented the position and associated ray angles of a set of fictitious rays passing through a lens with an index matched surrounding. Therefore this data set only contained information about the deflection of the ray due to the lens GRIN and not due to the refractive index difference between the lens surface and its surrounding medium as was the case during the actual equatorial measurement. Equation

(A.7) was calculated by first interpolating between the points of $[\bar{\psi}(\bar{y})]$ using a cubic spline interpolation. Once the coefficients of the spline were calculated, then the integral was evaluated to produce a data set $g(\xi)$. This data set was used in (A.3) and (A.4) to find the points $n(r)$ and r. Once these points were determined, a least squares fit was performed to determine the parabolic shape of the refractive index profile and the corresponding coefficients C_0, C_1, and C_2.

Chan tested the validity and accuracy of this extrapolation scheme of using 2D measurements in the equatorial plane to produce a 3D refractive index profile for the entire lens. A synthetic data set of 20 data points, $[\bar{\psi}(\bar{y})]$, was generated for a parabolic profile using 1.333 as the surrounding medium and 1.350 as the edge index value, with 1.420 for the core value, which were his accepted values for a bovine lens. The calculated index at the lens edge using (A.3), (A.4) and (A.7) was 1.35065; less than 0.05% error. Therefore this method is acceptable for determining the refractive index distribution in the equatorial plane.

[1] Campbell, M. C. W., *Measurement of refractive index in an intact crystalline lens,* Vis. Res. 1984; 24: 409-415.

[2] Chan, D. Y. C., Ennis, J. P., Pierscionek, B. K., Smith, G., *Determination and modeling of the 3-D gradient refractive indices in crystalline lenses*. Appl. Opt., 1988; 27, 5: 926-931.

[3] Chu P. L. *Nondestructive measurement of index profile of an optical-fibre preform*. Electron. Lett., 1977; 13: 736-738.

[4] Born, M., Wolf, E., *Principles of Optics, 7th ed.*, 1999, Cambridge, U.K.: Cambridge Press.

Appendix B

Modal Estimation of the Wavefront Phase from Phase Derivative Measurements

In this appendix, the modal estimation of the wavefront phase from measurements of the derivatives of the phase is described, as developed by Cubalcini(1978)[1]. In this method, the assumption is made that the phase of the wavefront can be estimated by an infinite sum of orthogonal functions, represented by:

$$\phi(X,Y) = \sum_{K} a_K \, Z_K(X,Y) \tag{B.1}$$

where the orthogonal functions used in this thesis are the Zernike polynomials, $Z_k(X,Y)$ and (X,Y) are the coordinates of the wavefront sensor. The assumption is also made that the sensor is split into sub-apertures, measuring the X and Y directional derivatives of the phase, given by:

$$P(X,Y)_i = \frac{\partial \phi(X,Y)_i}{\partial X} + \nu_i \tag{B.2}$$

and

$$Q(X,Y)_i = \frac{\partial \phi(X,Y)_i}{\partial Y} + \mu_i \tag{B.3}$$

respectively. $(X,Y)_i$ refers to the coordinates of the ith measurement, ν_i and μ_i refer to the measurement noise associated with the ith sample. The magnitude of the noise within the samples is a function of the spatial frequency content of the wavefront phase and the number of sub-apertures, therefore one would try to minimize this noise as much as possible by maximizing the number of sub-apertures as much as possible. For the rest of this argument, the noise across the sub-apertures is assumed to be zero. These directional derivatives are then used in the least squares fit to the Zernike polynomial to estimate the wavefront phase error.

First a measurement vector P is constructed to form an estimator:

$$P = \left\{P(X,Y)_1, P(X,Y)_2, \ldots, P(X,Y)_K, Q(X,Y)_1, Q(X,Y)_2, \ldots, Q(X,Y)_L\right\}^T \tag{B.4}$$

This measurement vector corresponds to the X and Y directional derivatives of the estimate. These will ultimately result in a set of constants based upon the measurement vector above, represented by the vector:

$$\hat{A} = \{\hat{a}_2, \hat{a}_3, \dots, \hat{a}_i\} \tag{B.5}$$

The estimate of the phase of the wavefront can be determined from:

$$\widehat{\Phi}(X,Y) = \sum_{i=2}^{I} \hat{a}_i \, Z_i(X,Y) \tag{B.6}$$

where the first term in the series, $\hat{a}_1 Z_1(X,Y)$ is a constant since it is the piston term and can therefore be omitted. Now $\hat{A}$ must be chosen such that the error squared between the estimates and the measurements is minimized. Since the measurement gives the directional derivatives, the minimization function must also contain the derivatives of the estimate:

$$\frac{\partial \widehat{\Phi}(X,Y)}{\partial X} = \sum_{i=2}^{I} \hat{a}_i \frac{\partial Z_i(X,Y)}{\partial X} \tag{B.7}$$

$$\frac{\partial \widehat{\Phi}(X,Y)}{\partial Y} = \sum_{i=2}^{I} \hat{a}_i \frac{\partial Z_i(X,Y)}{\partial Y} \tag{B.8}$$

and the least squares minimization function is given by:

$$F = \sum_{k=1}^{K} \left(P(X,Y)_k - \sum_{i=2}^{I} \hat{a}_i \frac{\partial Z_i(X,Y)_k}{\partial X} \right)^2 + \sum_{l=1}^{L} \left(Q(X,Y)_l - \sum_{i=2}^{I} \hat{a}_i \frac{\partial Z_i(X,Y)_l}{\partial Y} \right)^2 \tag{B.9}$$

In order to find the best fit, F is minimized with respect to $\hat{A}$, resulting in the following equations:

$$\sum_{k=1}^{K}\left(P(X,Y)_k\frac{\partial Z_j(X,Y)_k}{\partial X}\right)+\sum_{l=1}^{L}\left(Q(X,Y)_l\frac{\partial Z_j(X,Y)_l}{\partial Y}\right)$$
$$=\sum_{i=2}^{I}\left[\hat{a}_i\left(\sum_{k=1}^{K}\frac{\partial Z_j(X,Y)_k}{\partial X}\frac{\partial Z_i(X,Y)_k}{\partial X}\right.\right.$$
$$\left.\left.+\sum_{l=1}^{L}\frac{\partial Z_j(X,Y)_l}{\partial Y}\frac{\partial Z_i(X,Y)_l}{\partial Y}\right)\right] \tag{B.10}$$

where $j = 2,3,\ldots I$. This can also be written in matrix form as:

$$DP = E\hat{A}, \tag{B.11}$$

$$D=\begin{pmatrix}\frac{\partial Z_2(X,Y)_1}{\partial X} & \frac{\partial Z_2(X,Y)_2}{\partial X} & \cdots & \frac{\partial Z_2(X,Y)_K}{\partial X} & \frac{\partial Z_2(X,Y)_l}{\partial Y} & \cdots & \frac{\partial Z_2(X,Y)_L}{\partial Y}\\ \frac{\partial Z_3(X,Y)_1}{\partial X} & \frac{\partial Z_3(X,Y)_2}{\partial X} & \cdots & \frac{\partial Z_3(X,Y)_K}{\partial X} & \frac{\partial Z_3(X,Y)_l}{\partial Y} & \cdots & \frac{\partial Z_3(X,Y)_L}{\partial Y}\\ \vdots & \vdots & & \vdots & \vdots & & \vdots\\ \frac{\partial Z_l(X,Y)_1}{\partial X} & \frac{\partial Z_l(X,Y)_2}{\partial X} & \cdots & \frac{\partial Z_l(X,Y)_K}{\partial X} & \frac{\partial Z_I(X,Y)_l}{\partial Y} & \cdots & \frac{\partial Z_I(X,Y)_L}{\partial Y}\end{pmatrix} \tag{B.12}$$

and

$$E = DD^T \tag{B.13}$$

so the estimator can be found directly as:

$$\hat{A} = E^{-1}DP = (DD^T)^{-1}DP \tag{B.14}$$

giving $\hat{a}_i$ as the ith coefficient of the Zernike polynomial. As the coordinate system is Cartesian, the Zernike coefficients must be converted to this form before this method can be used.

In the analysis of the propagation of variances, it was shown that in order to minimize the error, the number of measurements should be minimized to estimate a fixed number of modes, and the measurements in estimating higher order modes should be taken far from the centre of the aperture. Also as the number of modes to be estimated increases, so does the variance of the individual modes.

[1] R. Cubalcini, "Modal wave-front estimation from phase derivative measurements," J. Opt. Soc. Am. **69**, 7, 972-977 (1979).

Appendix C

Biometric and Optical Measured Data for Pig, Rabbit, and Cow Lenses

Table C.1 Measured Biometric and Optical Properties of Pig Lenses

Pig	R_a	q_a	R_p	q_p	t	a_a	a_p	$2b$	b	F	SA	W
1	6.74	1.31	-4.32	0.00	6.52	2.83	3.69	8.46	4.23	23.75	-0.64	6.14
2	6.86	1.34	-4.42	0.00	6.68	2.90	3.78	8.64	4.32	24.13	-0.31	5.77
3	5.60	1.18	-3.97	-0.09	6.00	2.61	3.38	7.86	3.93	20.02	-0.27	5.51
4	6.07	1.23	-4.12	0.00	6.22	2.70	3.52	8.12	4.06	21.56	-0.15	7.21
5	5.68	1.16	-3.90	0.00	5.90	2.57	3.33	7.75	3.88	20.29	0.38	6.13
6	6.07	1.16	-3.92	0.00	5.93	2.58	3.35	7.79	3.89	21.57	-0.14	5.86
7	5.75	1.21	-4.05	0.00	6.12	2.66	3.46	8.01	4.00	20.50	-0.13	5.84
8	5.84	1.21	-4.04	0.00	6.11	2.66	3.45	7.99	4.00	20.81	-0.28	4.17
9	6.12	1.29	-4.28	0.00	6.47	2.81	3.66	8.41	4.20	21.73	-0.54	4.14
10	5.86	1.22	-4.07	0.00	6.15	2.67	3.47	8.03	4.02	20.87	-0.20	4.86
11	5.82	1.26	-4.19	0.00	6.33	2.75	3.58	8.24	4.12	20.72	-0.34	8.44
12	6.83	1.33	-4.38	0.00	6.61	2.87	3.74	8.56	4.28	24.03	-0.44	5.53
13	6.07	1.32	-4.35	-0.10	6.57	2.85	3.72	8.52	4.26	21.54	-0.21	4.38
14	5.75	1.22	-4.07	0.00	6.15	2.67	3.47	8.04	4.02	20.51	0.01	5.34
15	6.92	1.45	-4.72	-0.04	7.12	3.09	4.04	9.15	4.58	24.34	-0.18	5.29
16	7.79	1.53	-4.94	0.00	7.45	3.23	4.23	9.52	4.76	27.20	-0.33	6.16
17	7.83	1.57	-5.05	0.00	7.61	3.29	4.32	9.71	4.85	27.31	-0.23	5.70
18	6.86	1.50	-4.85	0.00	7.31	3.17	4.14	9.36	4.68	24.15	0.10	7.05
19	7.20	1.53	-4.93	0.00	7.43	3.22	4.21	9.50	4.75	25.27	0.16	4.95
20	7.49	1.49	-4.82	0.00	7.27	3.15	4.12	9.31	4.66	26.20	0.06	4.06
21	7.53	1.45	-4.71	0.00	7.10	3.08	4.03	9.13	4.56	26.33	-0.11	7.19
22	7.47	1.48	-4.79	0.00	7.22	3.13	4.09	9.26	4.63	26.15	-0.57	5.02

Table C.2: Measured Biometric and Optical Properties of Bunny Lenses

Bunny	R_a	q_a	R_p	q_p	t	a_a	a_p	$2b$	b	F	SA	W
1	7.44	1.03	5.91	0.00	7.74	3.58	4.16	10.51	5.25	22.90	-0.40	6.27
2	7.47	1.04	5.83	0.00	7.82	3.63	4.20	10.59	5.30	23.65	-1.11	3.18
3	7.57	1.09	5.68	0.00	7.79	3.68	4.11	10.94	5.47	23.49	-1.78	4.41
4	7.51	1.02	5.90	0.49	7.89	3.61	4.28	10.56	5.28	23.31	0.08	3.25
5	7.39	1.00	5.70	0.47	7.66	3.56	4.10	10.61	5.30	22.87	-0.26	4.57
6	7.21	0.98	5.50	0.13	7.60	3.55	4.06	10.41	5.21	22.59	-0.57	6.16
7	7.57	1.04	5.91	0.55	7.83	3.60	4.23	10.73	5.37	23.81	0.04	4.93

Table C.4: Measured Biometric and Optical Properties of Cow Lenses

Cow	R_a	q_a	R_p	q_p	t	a_a	a_p	$2b$	b	F	SA	W
1	11.83	0.97	9.78	0.00	12.19	5.21	7.19	16.52	8.26	34.45	-0.23	8.84
2	12.72	1.32	10.43	0.00	13.29	5.45	7.44	17.24	8.62	36.65	0.00	5.15
3	12.07	0.99	10.14	0.00	12.47	5.33	7.24	16.79	8.40	35.30	-0.24	10.17
4	13.38	1.34	11.06	0.00	14.72	6.02	7.62	17.37	8.69	37.71	-0.16	7.73
5	10.67	0.80	9.04	0.00	10.95	4.74	6.61	14.94	7.47	31.03	0.05	7.95
6	12.87	1.33	10.91	0.00	13.18	5.45	7.23	17.25	8.63	35.20	-0.55	11.98

Table C.5: Calculated Equatorial Coefficients

CO			C1			C2		
Rabbit	Cow	Pig	Rabbit	Cow	Pig	Rabbit	Cow	Pig
0.013	0.008	0.014	0.331	0.381	0.326	0.581	0.607	0.572
0.002	0.013	0.011	0.395	0.415	0.500	0.501	0.534	0.701
0.001	0.017	0.025	0.389	0.419	0.396	0.552	0.636	0.619
0	0.003	0.000	0.423	0.423	0.382	0.582	0.685	0.574
0.005	0.002	0.016	0.499	0.441	0.366	0.601	0.621	0.598
0.0073	0	0.009	0.437	0.479	0.436	0.682	0.632	0.526
0.0078		0.003	0.319		0.416	0.592		0.574
		0.000			0.528			0.558
		0.007			0.392			0.574
		0.007			0.370			0.595
		0.012			0.379			0.625
		0.002			0.335			0.563
		0.011			0.491			0.609
		0.003			0.426			0.596

Table C.6: Measured Optical and Biometric Relationships of Pig lenses.

y → / x ↓		R_a	q_a	R_p	t	a_a	a_p	b	F	SA	W
	m_1	X	0.221	-0.511	0.701	0.336	0.404	0.828	3.156		
	s.e.		0.023	0.198	0.246	0.094	0.145	0.256	0.943		
R_a	m_2	X	-0.089	-1.099	2.030	0.673	1.086	3.233	2.502		
	s.e.		0.007	0.035	0.382	0.125	0.356	0.134	0.787		
	r	X	0.956	-0.96	0.959	0.942	0.944	0.874	0.980	-0.085	-0.052
	m_1	4.320	X	-2.320	1.314	1.605	1.673	6.092	13.826		
	s.e.	0.492		0.382	0.094	0.047	0.063	1.278	3.392		
q_a	m_2	0.647	X	-1.338	0.803	0.693	1.468	0.401	4.558		
	s.e.	0.044		0.152	0.052	0.063	0.087	0.052	1.263		
	r	0.956	X	-0.894	0.958	0.892	0.865	0.819	0.922	-0.138	-0.101
	m_1	-1.803	-0.382	X	-1.375	-0.558	-0.803	-1.491	-5.791		
	s.e.	0.045	0.003		0.096	0.053	0.005	0.470	1.584		
R_p	m_2	1.495	0.344	X	-0.556	-0.408	-0.234	-1.986	2.559		
	s.e.	0.373	0.089		0.049	0.035	0.011	0.076	0.963		
	r	-0.960	-0.894	X	-0.961	-0.934	-0.954	-0.938	-0.955	0.053	0.075
	m_1	1.402	0.242	-0.672	X	0.426	0.579	1.141	4.584		
	s.e.	0.093	0.054	0.037		0.025	0.046	0.076	1.983		
t	m_2	-2.718	-0.272	0.064	X	0.053	-0.088	1.023	-7.320		
	s.e.	0.372	0.045	0.022		0.022	0.012	0.054	2.272		
	r	0.959	0.958	-0.961	X	0.979	0.988	0.937	0.928	-0.013	-0.031
	m_1	2.982	0.633	-1.558	2.290	X	1.288	3.062	9.324		
	s.e.	0.569	0.034	0.369	0.893		0.321	0.743	2.275		
a_a	m_2	-2.026	-0.461	0.072	0.037	X	0.042	-0.228	-3.635		
	s.e.	0.072	0.053	0.005	0.001		0.004	0.048	1.372		
	r	0.942	0.892	-0.934	0.979	X	0.936	0.912	0.914	-0.024	-0.029
	m_1	2.190	0.464	-1.169	1.687	0.687	X	1.853	8.477		
	s.e.	0.473	0.068	0.032	0.693	0.157		0.782	2.986		
a_p	m_2	-1.673	-0.383	-0.016	0.303	0.303	X	1.638	-8.340		
	s.e.	0.362	0.073	0.002	0.097	0.042		0.367	1.936		
	r	0.944	0.865	-0.954	0.988	0.936	X	0.929	0.913	-0.005	0.030
	m_1	1.078	0.157	-0.589	0.791	0.338	0.479	X	4.621		
	s.e.	0.269	0.073	0.026	0.024	0.072	0.026		1.854		
b	m_2	-2.790	0.004	0.646	-0.149	-0.030	-0.342	X	-16.529		
	s.e.	0.795	0.001	0.078	0.026	0.003	0.035		4.205		
	r	0.874	0.819	-0.938	0.937	0.912	0.929	X	0.859	0.030	-0.111
	m_1	0.305	0.066	-0.157	0.208	0.097	0.109	0.230	X		
	s.e.	0.013	0.003	0.047	0.035	0.005	0.009	0.012			
F	m_2	-0.504	-0.165	-0.790	1.823	0.646	1.292	3.279	X		
	s.e.	0.032	0.012	0.046	0.672	0.372	0.742	0.987			
	r	0.980	0.922	-0.955	0.928	0.914	0.913	0.859	X	-0.118	0.009
SA	m_1									X	

	m_2									X	
	r	-0.085	-0.138	0.053	-0.013	-0.024	-0.005	0.030	-0.118	X	0.076
	m_1										X
W	m_2										X
	r	-0.052	-0.101	0.075	-0.031	-0.029	0.030	-0.111	0.009	0.076	X

Table C.7: Measured Optical and Biometric Relationships of Bunny lenses.

y → / x ↓		R_a	q_a	R_p	t	a_a	a_p	b	F	SA	W
	m_1	X	0.136		0.714	0.178		1.046	3.126		
	s.e.		0.023		0.246	0.094		0.256	0.943		
R_a	m_2	X	0.005		2.435	2.260		2.820	-0.163		
	s.e.		0.007		0.382	0.125		0.134	0.787		
	r	X	0.786	-0.727	0.869	0.788	0.681	0.753	0.859	-0.125	-0.526
	m_1	2.802	X			1.225		5.108			
	s.e.	0.492				0.047		1.278	3.392		
q_a	m_2	4.570	X			2.337		5.360			
	s.e.	0.044				0.063		0.052	1.263		
	r	0.786	X	-0.253	0.550	0.952	0.172	0.900	0.688	-0.697	-0.342
	m_1	-0.574		X	-0.512		-0.437		-1.708		
	s.e.	0.045			0.096		0.005		1.584		
R_p	m_2	-4.123		X	-4.805		-1.645		-13.231		
	s.e.	0.373			0.049		0.011		0.963		
	r	-0.727	-0.253	X	-0.788	-0.265	-0.873	-0.119	-0.593	-0.387	-0.342
	m_1	1.060		-1.210	X		0.700		3.720		
	s.e.	0.093		0.037			0.046		1.983		
t	m_2	-0.757		3.627	X		-1.263		-5.640		
	s.e.	0.372		0.022			0.012		2.272		
	r	0.869	0.550	-0.788	X	0.685	0.909	0.427	0.837	0.045	-0.687
	m_1	2.187	0.740			X		3.183			
	s.e.	0.569	0.034					0.743			
a_a	m_2	-0.397	-1.628			X		-0.869			
	s.e.	0.072	0.053					0.048			
	r	0.788	0.952	-0.265	0.685	X	0.319	0.830	0.735	-0.659	-0.551
	m_1			-1.745	1.181		X				
	s.e.			0.032	0.693						
a_p	m_2			1.491	2.837		X				
	s.e.			0.002	0.097						
	r	0.681	0.172	-0.873	0.909	0.319	X	0.082	0.668	0.435	-0.579
	m_1	0.546	0.182			0.216		X			
	s.e.	0.269	0.073			0.072					
b	m_2	1.695	-0.900			1.309		X			
	s.e.	0.795	0.001			0.003		X			

	r	0.753	0.900	-0.119	0.427	0.830	0.082	X	0.657	-0.538	-0.320
	m_1	0.204			0.188				X		
	s.e.	0.013		0.047	0.035		0.009				
F	m_2	2.724			3.383				X		
	s.e.	0.032		0.046	0.672		0.742				
	r	0.859	0.688	-0.593	0.837	0.735	0.668	0.657	X	-0.166	-0.624
	m_1									X	
SA	m_2									X	
	r	-0.085	-0.138	0.053	-0.013	-0.024	-0.005	0.030	-0.118	X	0.076
	m_1										X
W	m_2										X
	r	-0.052	-0.101	0.075	-0.031	-0.029	0.030	-0.111	0.009	0.076	X

Table C.8: Measured Optical and Biometric Relationships of Cow lenses.

y → / x ↓		R_a	q_a	R_p	t	a_a	a_p	b	F	SA	W
	m_1	X	0.221	-0.511	0.701	0.336	0.404	0.828	3.156		
	s.e.		0.023	0.198	0.246	0.094	0.145	0.256	0.943		
R_a	m_2	X	-0.089	-1.099	2.030	0.673	1.086	3.233	2.502		
	s.e.		0.007	0.035	0.382	0.125	0.356	0.134	0.787		
	r	X	0.956	-0.96	0.959	0.942	0.944	0.874	0.980	-0.085	-0.052
	m_1	4.320	X	-2.320	1.314	1.605	1.673	6.092	13.826		
	s.e.	0.492		0.382	0.094	0.047	0.063	1.278	3.392		
q_a	m_2	0.647	X	-1.338	0.803	0.693	1.468	0.401	4.558		
	s.e.	0.044		0.152	0.052	0.063	0.087	0.052	1.263		
	r	0.956	X	-0.894	0.958	0.892	0.865	0.819	0.922	-0.138	-0.101
	m_1	-1.803	-0.382	X	-1.375	-0.558	-0.803	-1.491	-5.791		
	s.e.	0.045	0.003		0.096	0.053	0.005	0.470	1.584		
R_p	m_2	1.495	0.344	X	-0.556	-0.408	-0.234	-1.986	2.559		
	s.e.	0.373	0.089		0.049	0.035	0.011	0.076	0.963		
	r	-0.960	-0.894	X	-0.961	-0.934	-0.954	-0.938	-0.955	0.053	0.075
	m_1	1.402	0.242	-0.672	X	0.426	0.579	1.141	4.584		
	s.e.	0.093	0.054	0.037		0.025	0.046	0.076	1.983		
t	m_2	-2.718	-0.272	0.064	X	0.053	-0.088	1.023	-7.320		
	s.e.	0.372	0.045	0.022		0.022	0.012	0.054	2.272		
	r	0.959	0.958	-0.961	X	0.979	0.988	0.937	0.928	-0.013	-0.031
	m_1	2.982	0.633	-1.558	2.290	X	1.288	3.062	9.324		
	s.e.	0.569	0.034	0.369	0.893		0.321	0.743	2.275		
a_a	m_2	-2.026	-0.461	0.072	0.037	X	0.042	-0.228	-3.635		
	s.e.	0.072	0.053	0.005	0.001		0.004	0.048	1.372		
	r	0.942	0.892	-0.934	0.979	X	0.936	0.912	0.914	-0.024	-0.029
	m_1	2.190	0.464	-1.169	1.687	0.687	X	1.853	8.477		
a_p	s.e.	0.473	0.068	0.032	0.693	0.157		0.782	2.986		

	m_2	-1.673	-0.383	-0.016	0.303	0.303	X	1.638	-8.340		
	s.e.	0.362	0.073	0.002	0.097	0.042		0.367	1.936		
	r	0.944	0.865	-0.954	0.988	0.936	X	0.929	0.913	-0.005	0.030
	m_1	1.078	0.157	-0.589	0.791	0.338	0.479	X	4.621		
	s.e.	0.269	0.073	0.026	0.024	0.072	0.026		1.854		
b	m_2	-2.790	0.004	0.646	-0.149	-0.030	-0.342	X	-16.529		
	s.e.	0.795	0.001	0.078	0.026	0.003	0.035		4.205		
	r	0.874	0.819	-0.938	0.937	0.912	0.929	X	0.859	0.030	-0.111
	m_1	0.305	0.066	-0.157	0.208	0.097	0.109	0.230	X		
	s.e.	0.013	0.003	0.047	0.035	0.005	0.009	0.012			
F	m_2	-0.504	-0.165	-0.790	1.823	0.646	1.292	3.279	X		
	s.e.	0.032	0.012	0.046	0.672	0.372	0.742	0.987			
	r	0.980	0.922	-0.955	0.928	0.914	0.913	0.859	X	-0.118	0.009
	m_1									X	
SA	m_2									X	
	r	-0.085	-0.138	0.053	-0.013	-0.024	-0.005	0.030	-0.118	X	0.076
	m_1										X
W	m_2										X
	r	-0.052	-0.101	0.075	-0.031	-0.029	0.030	-0.111	0.009	0.076	X

Table C.9 Measured Focal length and Calculated Focal Length Using the Custom Crystalline Lens Model for Cow Lenses

Measured Focal Length (mm)	Calculated Focal Length (mm)
34.45	35.30
36.65	37.79
35.30	34.58
37.71	37.41
31.03	32.98
35.20	34.56

Table C.10 Measured Focal length and Calculated Focal Length Using the Custom Crystalline Lens Model for Pig Lenses

Measured Focal Length (mm)	Calculated Focal Length (mm)
23.40	24.30
24.74	25.78
19.57	19.58
21.64	22.41
22.60	21.68
21.69	21.56
21.73	20.47
20.27	19.79
21.45	19.51
20.62	19.75
20.63	21.59
23.91	24.04
21.55	22.08
20.44	20.99
24.22	23.73
28.09	28.98
27.74	28.19
24.86	24.38
25.61	25.73
26.10	25.16
26.84	26.05
26.15	25.07

☺